1 of 2
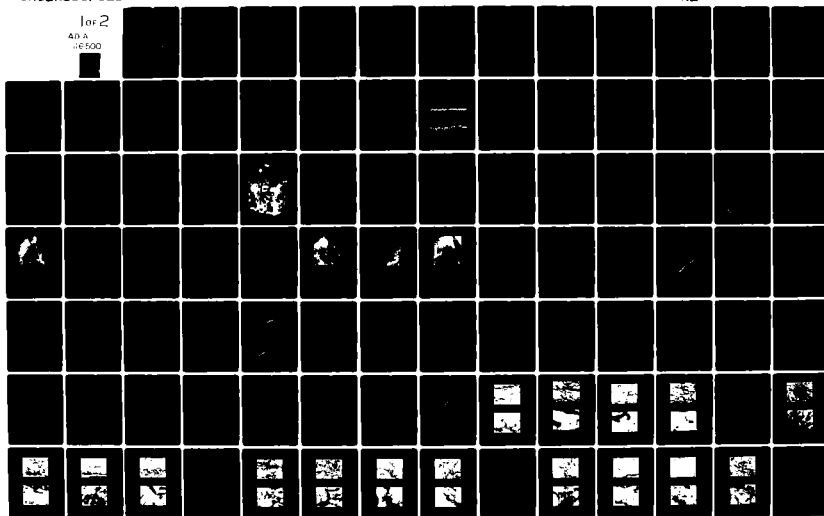
AD A
116500

METHODOLOGY FOR EVALUATION OF FATIGUE CRACK-GROWTH RESISTANCE OF ALUMINUM ALLOYS UNDER SPECTRUM LOADING

G.R. Chanani
I. Telesman
P.E. Bretz
G.V. Scarich

NORTHROP CORPORATION
AIRCRAFT DIVISION
ONE NORTHROP AVENUE
HAWTHORNE, CALIFORNIA 90250

APRIL 1982

TECHNICAL REPORT
FINAL REPORT FOR PERIOD 4 AUGUST 1980 — 4 AUGUST 1981

APPROVED FOR PUBLIC RELEASE; DISTRIBUTION UNLIMITED

DEPARTMENT OF THE NAVY
NAVAL AIR SYSTEMS COMMAND
WASHINGTON, D.C. 20361

REPORT DOCUMENTATION PAGE		READ INSTRUCTIONS BEFORE COMPLETING FORM
1. REPORT NUMBER	2. GOVT ACCESSION NO.	3. RECIPIENT'S CATALOG NUMBER
4. TITLE (and Subtitle) Methodology for Evaluation of Fatigue Crack-Growth Resistance of Aluminum Alloys under Spectrum Loading		5. TYPE OF REPORT & PERIOD COVERED Final 4 Aug. 1980 - 1 Aug. 1981
		6. PERFORMING ORG. REPORT NUMBER NOR 82-54
7. AUTHOR(s) G.R. Chanani, I. Telesman, P.E. Bretz (Alcoa), and G.V. Scarich (See Block 18)		8. CONTRACT OR GRANT NUMBER(s) N00019-80-C-0427
9. PERFORMING ORGANIZATION NAME AND ADDRESS Northrop Corporation, Aircraft Division One Northrop Avenue Hawthorne, California 90250		10. PROGRAM ELEMENT, PROJECT, TASK AREA & WORK UNIT NUMBERS N00019-80-PR-RL105
11. CONTROLLING OFFICE NAME AND ADDRESS Department of the Navy Naval Air Systems Command Washington, D.C. 20361		12. REPORT DATE April 1982
		13. NUMBER OF PAGES 136
14. MONITORING AGENCY NAME & ADDRESS(if different from Controlling Office)		15. SECURITY CLASS. (of this report) Unclassified
		15a. DECLASSIFICATION DOWNGRADING SCHEDULE

16. DISTRIBUTION STATEMENT (of this Report)

Approved for public release; distribution unlimited

17. DISTRIBUTION STATEMENT (of the abstract entered in Block 20, if different from Report)

18. SUPPLEMENTARY NOTES

Other contributors to the report are: J.H. FitzGerald - Northrop, and R.J. Bucci and R.R. Sawtell - Alcoa

19. KEY WORDS (Continue on reverse side if necessary and identify by block number)

Aluminum Alloys		Spectrum Loading
2024	7475	Retardation
2124	Microstructure	Fracture Toughness
7050	Temper	Constant Amplitude Loading
7075	Fatigue Crack-Growth	Variable Amplitude Loading

20. ABSTRACT (Continue on reverse side if necessary and identify by block number)

The purpose of this program is to obtain guidelines and test methodologies for selection and development of spectrum fatigue resistant, higher strength aluminum alloys for application to aircraft structures. The results described in this report present baseline characteristics of a number of high strength aluminum alloys for use in the future phases of this investigation.

Seven commercial 2XXX and 7XXX aluminum alloys were chosen and have been characterized with respect to chemical composition, microstructure, tensile

DD FORM 1 JAN 73 1473 EDITION OF 1 NOV 65 IS OBSOLETE

properties, and fracture toughness. Fatigue crack propagation (FCP) tests were conducted on specimens of each alloy for both constant-amplitude loading (including the near-threshold region) and two F-18 load spectra. One of the spectra was dominated by tension loads and the other contained tension and compression loads of nearly equal magnitude. The spectrum FCP testing was performed at maximum peak stress of 145 MPa (21 ksi) as well as limited testing at 103 and 169 MPa (15 and 24.5 ksi) to obtain additional data at the low and high end of the crack-growth range. Pertinent fracture surface features were documented on the spectrum fatigue specimens.

For fatigue crack growth testing under constant amplitude loading, the significant observations were that: 1) The differences in fatigue crack-growth rates were greatest in the near-threshold regime, where 2024-T351 and 7475-T651 showed the highest resistance to FCP and 2) FCP resistance varied with stress intensity factor range (ΔK). For example, in contrast to its excellent near-threshold crack-growth resistance, alloy 7475-T651 had the lowest resistance to FCP for ΔK greater than 6 MPa $\sqrt{m}$.

For spectrum testing at the maximum peak stress of 145 MPa (21 ksi):

1. The ranking of the alloys by spectrum life is the same for both spectra. The alloys ranked as follows with their percentage of life relative to 2024-T351, averaged for both spectra, shown in parenthesis: 2024-T351 (100%), 7475-T651 (82%), 7050-T73651 (73%), 7475-T7351 (72%), 7075-T7351 (64%), 2124-T851 (56%), and 2024-T851 (45%).

2. For each material the tension-dominated (TD) spectrum consistently resulted in longer lives than the tension-compression (TC) spectrum.

For the spectrum testing at 103 MPa (15 ksi), which was limited to a smaller range of crack-growth at lower stress intensities than that for the 145 MPa (21 ksi) testing: 1) Each alloy had about the same spectrum fatigue life, except for the 2024-T351 alloy which had a significantly longer spectrum fatigue life than the other alloys and 2) for each alloy, the TD spectrum resulted in a nearly equal or somewhat longer spectrum fatigue life than the same alloy tested with the TC spectrum.

Spectrum testing at 169 MPa (24.5 ksi), which represented a smaller range of crack-growth than the testing at 145 MPa (21 ksi) resulted in rankings similar to the 145 MPa (21 ksi) testing — the only significant change was that for the TD spectrum, 2024-T351 had a lower life than three of the four 7XXX alloys.

The T351 temper of 2024 had better constant amplitude and spectrum FCP resistance at all stress intensities than the T851 temper. The T651 temper of 7475 had better constant amplitude FCP resistance at low stress intensities, but lower resistance at high stress intensities than the T7351 temper. However, for spectrum FCP, the results were just the opposite.

Further work in the next phase of this program is in progress to correlate microstructural and fractographic features to spectrum behavior. This information will be used to select microstructures and simplified spectra to critically evaluate the role of specific microstructural features on crack retardation and growth process.

PREFACE

DTIC
COPY
INSPECTED
2

Accession For

NTIS

DTIC

By
Distribution

Dist

A

iii

CONTENTS

CONTENTS (Continued)

FIGURES

FIGURES (Continued)

TABLES

ABBREVIATIONS AND SYMBOLS

a	Crack-length
a_i	Initial crack length
a_c	Current crack length
a_f	Final crack length
B	Specimen thickness
COD	Crack opening displacement
da/dH	Spectrum crack-growth rate
da/dN	Crack-growth rate (constant amplitude)
F	Failure
FCGR	Fatigue-crack growth rate
FCP	Fatigue-crack propagation
H	Simulated flight hours or half height of compact tension specimen
K	Stress-intensity factor
K_{hmax}	Stress intensity factor at largest (highest) peak of a spectrum
K_{hmin}	Stress intensity factor at smallest (lowest) valley of a spectrum
K_{max}	Maximum stress intensity factor
K_{Ic}	Plane strain fracture toughness
K_Q	Conditional fracture toughness, test did not meet all the ASTM E399 validity criteria
L-T	Crack growth on plane normal to the rolling direction (L) of the plate in a direction transverse (T) to the rolling direction (per ASTM E399)
N	Number of cycles
P_{hmax}	Load at largest (highest) peak of a spectrum
P_{hmin}	Load at smallest (lowest) valley in a spectrum
P_{max}	Peak Load
P_{sm}	Mean spectrum load
R	Stress or load ratio $= P_{min}/P_{max}$
SEM	Scanning electron microscope/microscopy
TC	Tension-compression, horizontal hinge tail *moment spectrum*
TD	Tension-dominated, lower wing root spectrum
TEM	Transmission electron microscope/microscopy

ABBREVIATIONS AND SYMBOLS (continued)

T/2	Mid-thickness (center) location in a plate
T/4	Quarter-thickness location in a plate
3T/4	Three-quarter thickness location in a plate
W	Specimen width
YS	Yield strength
ΔK	Stress-intensity range
ΔK_h	Overall stress intensity range of a spectrum
ΔP	Load range
ΔP_h	Overall load range of a spectrum
$\Delta \sigma$	Stress range: Algebraic difference between successive valley and peak (positive or increasing) or between successive peak and valley (negative or decreasing).
$\Delta \sigma_h$	Overall stress range in a spectrum
σ	Applied stress
σ_{hmax}	Stress at largest (highest) peak of a spectrum
σ_{hmin}	Stress at smallest (lowest) valley of a spectrum
σ_{sm}	Spectrum mean stress

I. INTRODUCTION

Fatigue crack growth behavior under variable amplitude loading is increasingly being used in the selection of materials for aircraft structures and their design, particularly for fatigue critical structures. This is supplanting the selection of materials based on their constant amplitude fatigue crack growth resistance because the life of an aircraft structure cannot be predicted reliably using constant amplitude fatigue crack growth data and existing life prediction techniques. Research in the last decade [1-12] has shown that load sequences have a considerable effect on fatigue-crack propagation (FCP) behavior. In particular, the application of overloads or a few cycles at high tensile loads may cause retardation; that is, a temporary decrease in fatigue-crack growth rate during subsequent lower-amplitude cycles. Most of the work in the last decade was focused on understanding the effects of single overloads on fatigue crack growth rates [1-10]. Recently more emphasis is being placed upon the evaluation of fatigue crack growth under complex spectrum loading [11-14] simulating the loading experienced by aircraft structures.

The nature of a spectrum can vary widely depending on a particular component and type of aircraft. Depending on the specific details of load spectra, FCP resistance for a given material can vary widely. Often the reasons why different FCP resistance is observed for the same materials are unknown, since the load spectra are complex and the interactions between alloy microstructure and variable amplitude load histories are not well understood.

Research in the last decade [1-4, 15-19] on high strength aluminum alloys has identified several microstructural factors which influence FCP resistance for constant amplitude loading: alloy purity (Fe, Si content), temper, Cu content, and dispersoid type (e.g., $Al_{12}Mg_2Cr$ in 7075 vs. Al_3Zr in 7050). However, the influence of these microstructural features on crack growth is not the same at intermediate and high growth rates ($>10^{-8}$ m/cycle (2.5×10^{-7} in./cycl.)) as it is at near-threshold rates ($<10^{-8}$ m/cycle). For example, overaging from a T6 temper to a T7 temper reduces FCP rates by a factor of two at intermediate stress intensities (ΔK) but can increase crack growth rates by a

1

factor of ten at low ΔK. These studies demonstrate that different microstructural features control constant amplitude FCP behavior at different ΔK values.

The same level of understanding regarding microstructural effects on FCP under variable amplitude loading does not exist. Whereas constant amplitude loading characterizes the steady state FCP response of an alloy, FCP under variable amplitude loading includes transient material responses not present in constant amplitude FCP. Therefore, the understanding of microstructural effects on constant amplitude FCP behavior is not sufficient to rationalize spectrum fatigue performance. In particular, the ability of an alloy to retard crack growth following a tensile overload is an important transient characteristic for assessing FCP life. However, since the present knowledge regarding the effect of microstructure on retardation behavior of aluminum alloys is limited to studies involving simple overload spectra, the results under spectrum loading at present cannot be understood.

Several mechanisms have been proposed to explain the observed retardation behavior following simple overloads. These include residual compressive stresses at the crack-tip [20, 21], crack closure [22-24], changes in the crack-tip plastic zone size [1, 20, 25], crack-blunting [1, 26], or combinations of these. A number of empirical models, based on either the crack closure [22, 23] or plastic zone size [20, 21] concepts, have been proposed that quantitatively take retardation into account in predicting FCP behavior. These models achieve satisfactory results only under certain specified conditions. However, when the test conditions are changed or broadened to include additional variables such as those existing in real spectra, the models usually fail to predict observed crack-growth lives.

The major weakness of all of these models is that they do not take into account either metallurgical or the environmental factors that influence FCP. For instance, the Willenborg model predicts that materials with the same yield strength will exhibit similar retardation behavior [20]. Chanani [1] found that this was not the case for 2024-T8 and 7075-T73 heat treated to the same yield strength. He concluded that metallurgical variables such as precipitate morphology, dislocation interactions, and cyclic hardening exponent, have to be taken into account to explain the differences between the crack growth rates. Sanders et al [2] had identified microstructural features such as precipitate

morphology, intermetallic constituent particles, and dispersoid size as influencing FCP. Improved analytical life prediction capabilities would result if microstructure/load history interactions for spectrum FCP are understood and incorporated in such models.

The purpose of the multiphase NAVAIR program (N00019-80-C-0427 and N00019-81-C-0550) is to perform a detailed metallurgical investigation and to simplify complex load histories into generic spectra which are representative of certain classes of applications and provide information for development of fatigue resistant alloys. As a major part of this effort, attention will be given to identifying metallurgical factors in high strength aluminum alloys which control FCP behavior under spectrum loading. This knowledge of load history/microstructure interactions is essential to the development of criteria by which complex load histories can be standardized and simplified for materials evaluation.

The development of standardized and/or simplified load spectra offers several advantages in characterizing the fatigue performance of engineering materials and designing fatigue resistant alloys. It is presently not cost-effective to develop alloys for high resistance to FCP under spectrum loading, since a wide variety of load histories must be considered. If a small number of standardized spectra existed, more meaningful tests which consider spectrum loading can be included in alloy development/selection programs. Standardized load spectrum also would provide a common data base for comparisons of fatigue performance among various materials. Selected existing life prediction tools will be evaluated, and the incorporation of metallurgical factors in these models will be examined.

This report describes the work completed in Phase I of this program. Seven commercial 2XXX and 7XXX aluminum alloys (Figure 1) were chosen for analysis so that the influence of both purity and temper on FCP can be evaluated. All seven alloys have been characterized with respect to chemical composition, microstructure, tensile properties, and fracture toughness. FCP tests have also been conducted on specimens of each alloy for both constant amplitude loading (including the low ΔK region) and two F-18 load spectra. One is a tension-dominated spectrum representing the lower wing root load history, and the other is a tension-compression spectrum representing the horizontal tail hinge moment load history. In the spectrum testing, one primary stress level was used for FCGR testing, while two other stress levels were used to obtain data at the low and high ends of the crack-growth range.

INVESTIGATION OF FATIGUE CRACK GROWTH OF ALUMINUM ALLOYS UNDER SPECTRUM LOADING

MATERIALS

PRESENT EFFORT	FUTURE EFFORT
2024-T351	2020-T651
2024-T851	TMT2020-T6X51
2124-T851	2324-T39
7050-T73651	7075-T651
7075-T7351	7150-T6E189
7475-T651	X7091-T7E69
7475-T7351	SPECIAL HEATS WITH SELECTED MICROSTRUCTURES

SPECIFIC COMPARISONS

- ALLOY PURITY (FRACTURE TOUGHNESS)
  7075 vs 7475 and 2024 vs 2124

- PRECIPITATE STRUCTURE (TEMPER)
  2024-T351 vs T851, 7475-T651 vs T7351, and 7075-T651* vs T7351

- GRAIN SIZE*
  P/M (FINE) vs I/M (COARSE) and TMT 2020 (FINE) vs CONVENTIONAL 2020 (COARSE)

- EXISTING ALLOYS vs NEW ALLOYS AND APPROACHES*
  7XXX vs X7091 P/M and 7150, and 2XXX vs 2324 and Al-Li (2020 TYPE)

GENERAL COMPARISONS

TENSILE
FRACTURE TOUGHNESS
MICROSTRUCTURE
CONSTANT AMPLITUDE FATIGUE CRACK PROPAGATION

LOAD HISTORY

TWO F-18 SPECTRA
THREE STRESS LEVELS**
MODIFICATIONS OF THE F-18 SPECTRA*

SPECTRUM TEST SPECIMEN

6mm THICK X 100mm WIDE CENTER CRACKED PANEL
L-T ORIENTATION

*FUTURE EFFORT
**SECOND AND THIRD STRESS LEVEL RESULTS ON
2024-T851 AND 7475-T7351 FROM N00019-81-C-0550

FIGURE 1. PROGRAM OUTLINE

Fractographic examination of the spectrum fatigue specimens was used to document pertinent fracture features for each alloy.

The information obtained in this first phase represents a baseline characterization of the seven alloys on which subsequent program phases will build. In succeeding programs, analyses of fatigue data, microstructural analysis, fractography, and life prediction models will be used to identify metallurgical factors and isolate those portions of each spectrum which dominate FCP behavior. From this information, special alloys (if necessary) with selected microstructures, and simplified spectra will be used to critically examine the role of specific microstructural features on crack retardation and growth processes in high strength aluminum alloys. From these results, guidelines and test methodologies for selection and development of fatigue resistant, high strength aluminum alloys for complex aircraft loading will be obtained.

II. EXPERIMENTAL PROCEDURE

Commercially produced 2X24 and 7XXX aluminum alloy plates in various tempers, as shown in Figure 1, and ranging in thickness from 19 to 38mm (0.75 to 1.5 in.) were utilized in the program. The acceptability of each plate was verified by chemical composition analysis, and by tensile and fracture toughness (K_{Ic}) tests as described in this section. Also described in this section are the fatigue crack growth test procedures and background on the spectra selected for use in the program. The plates were characterized for their tensile properties at the T/4, 3T/4, T/2 and the near-surface locations. However, the spectrum FCP testing was performed on specimens obtained from the T/4 and 3T/4 locations of the plates because of the uniformity of the tensile properties at these locations.

2.1 CHEMICAL ANALYSIS

The chemical composition of each of the seven plates was determined on remelt samples of material (about 65 g each) cut from the plates. A quantometer interfaced with a minicomputer was used to obtain the analyses.

2.2 METALLOGRAPHY AND FRACTOGRAPHY

Specimens for optical metallography were taken from the T/4 location in each alloy plate to insure that the observed microstructures were typical of those in the spectrum specimens. Standard metallographic procedures were used in preparing all the specimens. One of the two etchants listed was used on each alloy, as noted on the micrographs.

Keller's Etch	Graff-Sargent Etch
2 ml HF (48%)	0.5 ml HF (conc.)
3 ml HCl	3 ml CrO_3
5 ml HNO_3	15.3 ml HNO_3
190 ml H_2O	84 ml H_2O

Specimens for fractographic analysis were cleaned ultrasonically in an acetone bath, rinsed in alcohol, and gold-coated to improve resolution. Fractographs of the fracture surface of each specimen were obtained at crack lengths, a, of 6.4 mm (0.25 in.) and 19 mm (0.75 in.).

2.3 TENSILE TESTS

Tensile tests were conducted in accordance with ASTM Standard Method B557. All tests were performed at room temperature in laboratory air on specimens taken in the longitudinal (L) orientation with respect to the rolling direction. Specimen location, nominal diameter, and gage length are listed below. It was necessary to vary specimen size in order to locate the reduced test section of each specimen at the appropriate location through the plate: center (T/2) quarter thickness (T/4), three-quarter thickness (3T/4), and near surface.

Specimen Location	No. of Specimens	Nominal Diameter		Gage Length	
		mm	(in.)	mm	(in.)
T/2	2	12.7	(0.500)	50.8	(2.00)
T/4, 3T/4	1 each	6.4	(0.250)	25.4	(1.00)
near surface	1 each	4.1	(0.160)	16.3	(0.64)

2.4 FRACTURE TOUGHNESS (K_{Ic}) TESTS

Fracture toughness tests were conducted in accordance with ASTM Standard Method E399. All tests were performed at room temperature in laboratory air on compact-tension (CT) specimens taken in the longitudinal (L-T) orientation with respect to the rolling direction. Two specimens were taken from each plate; the nominal thickness and nominal width of the specimens for each plate are listed below.

Nominal Plate Thickness		Nominal Specimen Thickness (B)		Nominal Specimen Width (W)	
mm	(in.)	mm	(in.)	mm	(in.)
19.0	(0.75)	19.0	(0.75)	38.1	(1.50)
25.4	(1.00)	25.4	(1.00)	50.8	(2.00)
31.8	(1.25)	31.8	(1.25)	63.5	(2.50)
38.1	(1.50)	38.1	(1.50)	76.2	(3.00)

2.5 FATIGUE CRACK PROPAGATION (FCP) TESTS UNDER CONSTANT LOAD AMPLITUDE

Constant load amplitude FCP tests were conducted over low, intermediate, and high stress intensity (ΔK) ranges on modified compact-type (WOL) specimens (B = 6.35mm (0.25 in.), W = 64.8mm (2.55 in.), and H/W = 0.486) in the longitudinal (L-T) orientation. Specimens were taken from the T/4 and 3T/4 locations in each plate. All testing was performed on closed loop, servo-hydraulic test machines at a load ratio (R = P_{min}/P_{max}) equal to 0.33 and at a test frequency of 25 Hz. Test environment was room temperature laboratory air with high humidity (relative humidity >90%).

The precracking of each specimen was conducted at R = 0.1 or 0.33 with visual crack length measurement. Upon attaining the desired precrack crack length, a, an automated test system utilizing a computer for data acquisition and machine control was used to obtain the crack growth rate (da/dN) data. Crack length was monitored continuously by an elastic compliance technique, enabling the stress intensity factor, K, to be controlled according to the equation:

$$K = K_o \, exp \, [C \, (a_c - a_i)]$$

where K_o is the initial cyclic stress intensity corresponding to the starting crack length, a_i ; a_c is the current crack length, and C is the constant with the dimension of 1/length [27]. A double cantilever clip-on displacement gage was used for monitoring crack opening displacements (COD). The K-decreasing tests (near-threshold) were conducted using a value for the parameter C of -38.1 mm^{-1} (-1.5 in.$^{-1}$), and the K-increasing tests (intermediate and high ΔK) were conducted using values of C between 44.4 mm^{-1} (1.75 in.$^{-1}$) and 63.5 mm^{-1} (2.5 in.$^{-1}$). Several visual crack length measurements were also made during each test for verification.

The test procedures strictly adhered to the ASTM Standard Test Method E647 for Constant-Load-Amplitude Fatigue Crack Growth Rates above 10^{-8} m/cycle, and to the proposed ASTM Standard test practice for measurement of near-threshold growth rates, da/dN < 10^{-8} m/cycle[28].

2.6 SPECTRUM TESTING

2.6.1 Spectrum Selection and Definition

Two different F-18 spectra were selected for this program. Portions of these spectra are shown in Figure 2, while Figure 3 shows the terminology used to describe spectrum test parameters. One is a tension-dominated spectrum representing the lower wing root load history and the other is a tension-compression spectrum representing the horizontal tail hinge moment load history. Both spectra were computer generated for the two components of the same aircraft assuming an identical sequence of events.
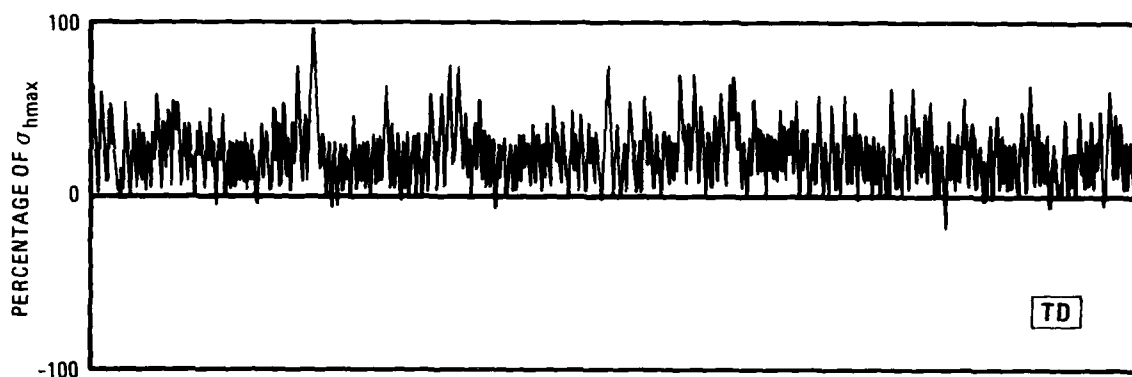
a. TENSION-DOMINATED SPECTRUM (WING ROOT)
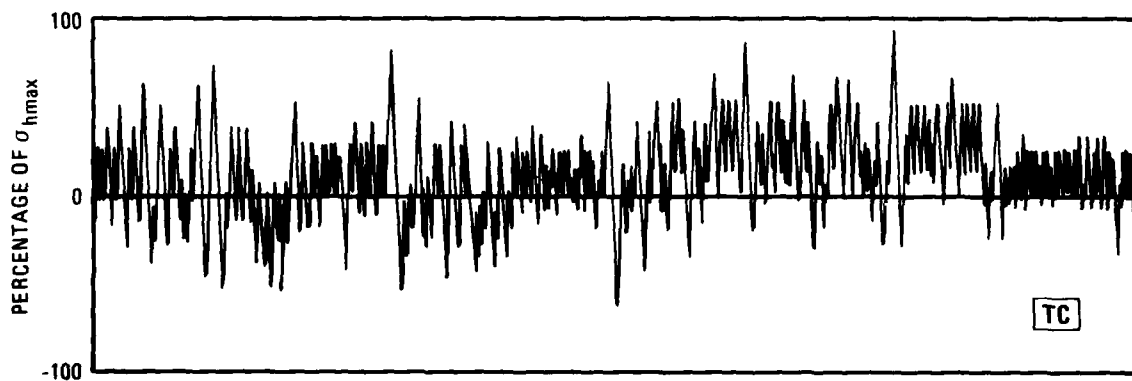
b. TENSION-COMPRESSION SPECTRUM (HORIZONTAL TAIL HINGE)

FIGURE 2. REPRESENTATIVE PORTIONS OF STRESS
HISTORY OF EACH SPECTRUM

9
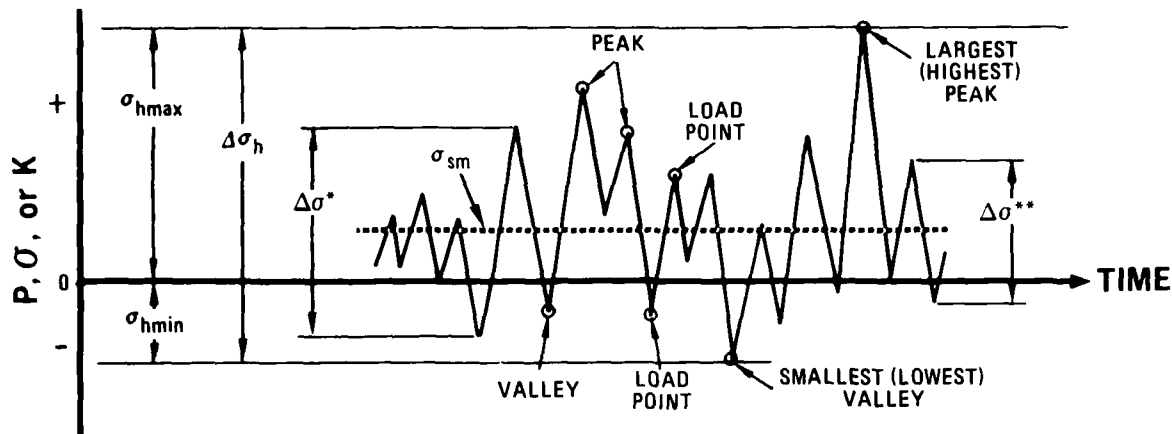
- P_{max}, σ_{max}, OR K_{max} = PEAK LOAD, STRESS, OR STRESS INTENSITY FACTOR

- P_{min}, σ_{min} OR K_{min} = MINIMUM LOAD, STRESS, OR STRESS INTENSITY FACTOR

- ΔP, $\Delta \sigma$, OR ΔK = RANGE OF LOAD, STRESS, OR STRESS INTENSITY FACTOR; ALGEBRAIC DIFFERENCE BETWEEN SUCCESSIVE VALLEY AND PEAK (POSITIVE OR INCREASING) OR BETWEEN SUCCESSIVE PEAK AND VALLEY (NEGATIVE OR DECREASING)

- P_{hmax}, σ_{hmax}, OR K_{hmax} = LOAD, STRESS, OR STRESS INTENSITY FACTOR AT LARGEST (HIGHEST) PEAK OF A SPECTRUM

- P_{hmin}, σ_{hmin}, OR K_{hmin} = LOAD, STRESS, OR STRESS INTENSITY FACTOR AT SMALLEST (LOWEST) VALLEY, I.E., THE LOWEST ALGEBRAIC VALUE IN A SPECTRUM

- ΔP_h, $\Delta \sigma_h$ OR ΔK_h = OVERALL LOAD, STRESS, OR STRESS INTENSITY RANGE, I.E., THE ALGEBRAIC DIFFERENCE BETWEEN THE LARGEST PEAK AND THE SMALLEST VALLEY OF A SPECTRUM

- P_{sm} OR σ_{sm} = SPECTRUM MEAN LOAD OR STRESS, ALGEBRAIC AVERAGE OF ALL THE PEAK AND VALLEY STRESSES OR LOADS OF A SPECTRUM

NOTES: 1. STRESS IS GROSS STRESS
2. STRESS INTENSITY IS A FUNCTION OF CRACK LENGTH
*ALSO CALLED POSITIVE OR INCREASING LOAD RANGE
**ALSO CALLED NEGATIVE OR DECREASING LOAD RANGE

FIGURE 3. DEFINITION OF TERMS

One "pass" of this basic event spectrum consists of a sequence of 250 flights representing 300 flight hours. One pass of the tension-dominated (TD) spectrum (wing root) has 4,705 load peaks and an equal number of valleys while the tension-compression (TC) spectrum (horizontal tail hinge) has 7,852 load peaks and an equal number of valleys. Since the service life of the F-18 aircraft is 6,000 hours, one service life is obtained by completion of a total of 20 passes of the above sequence. The F-18 is designed to last four lifetimes, i.e., 24,000 flight hours.

The F-18 was used as a basis for selection of spectra, stresses, and lives; therefore, a very brief and simplified description of the F-18 design follows.

10

The F-18 (more precisely F/A-18A) aircraft is a Navy carrier-based fighter/ attack aircraft. The life requirements for analysis of components are based on both durability and damage tolerance criteria. These criteria differ from the U.S. Air Force requirements of MIL-A-83444 in which the damage tolerance is based on fatigue crack growth from assumed initial flaws to various inspectability criteria. The F-18 durability and damage tolerance requirements include various combinations of fatigue crack initiation, assumed initial flaws, and growth requirements with a different number of lifetimes for each combination. The initial flaw size (or initiation) requirements are less severe than the Air Force requirements; however, the F-18 must endure more severe spectra and longer inspection intervals.

A discussion of the spectrum generation procedure follows and a schematic chart of the procedure is shown in Figure 4. The first 100 flights out of a total of 250 flights are carrier operations which initiate with a catapult launch and end with an arrested landing. The following 150 flights are field operations ending with a field landing. Field carrier landing practices are also dispersed at intervals during the field operation phase of the spectrum.

Each flight is flown at one of four critical points defined by a weight, speed, and altitude. Symmetrical events (pitch and level flight) within a flight are defined by a peak and valley load factor (n_z) sequence. Asymmetric conditions (rolls) are defined by a given roll rate ($\dot{p}$) which gives a positive and negative load perturbation to the associated symmetrical load. Landings are defined by type (arrested landings, touch-and-go, field, etc.) and sink speed.

The load sequence for a particular location on the aircraft structure is obtained for each defined event from a table linking load magnitude with load factor (n_z) at each critical point condition; roll rate and load factor at each critical point condition; and with sink speed for each type of landing. The table is obtained from the results of a finite element model run of the complete structure loaded by a range of unit conditions. The load values are normalized by dividing them by the load for a reference condition. This normalized load sequence is then "laundered" to eliminate small perturbations and "pass through" event peaks which are smaller than the valley of the previous event. After the laundering operation the final load sequence is stored on a permanent file to be called up for analysis or the creation of a test tape. A listing of the spectrum
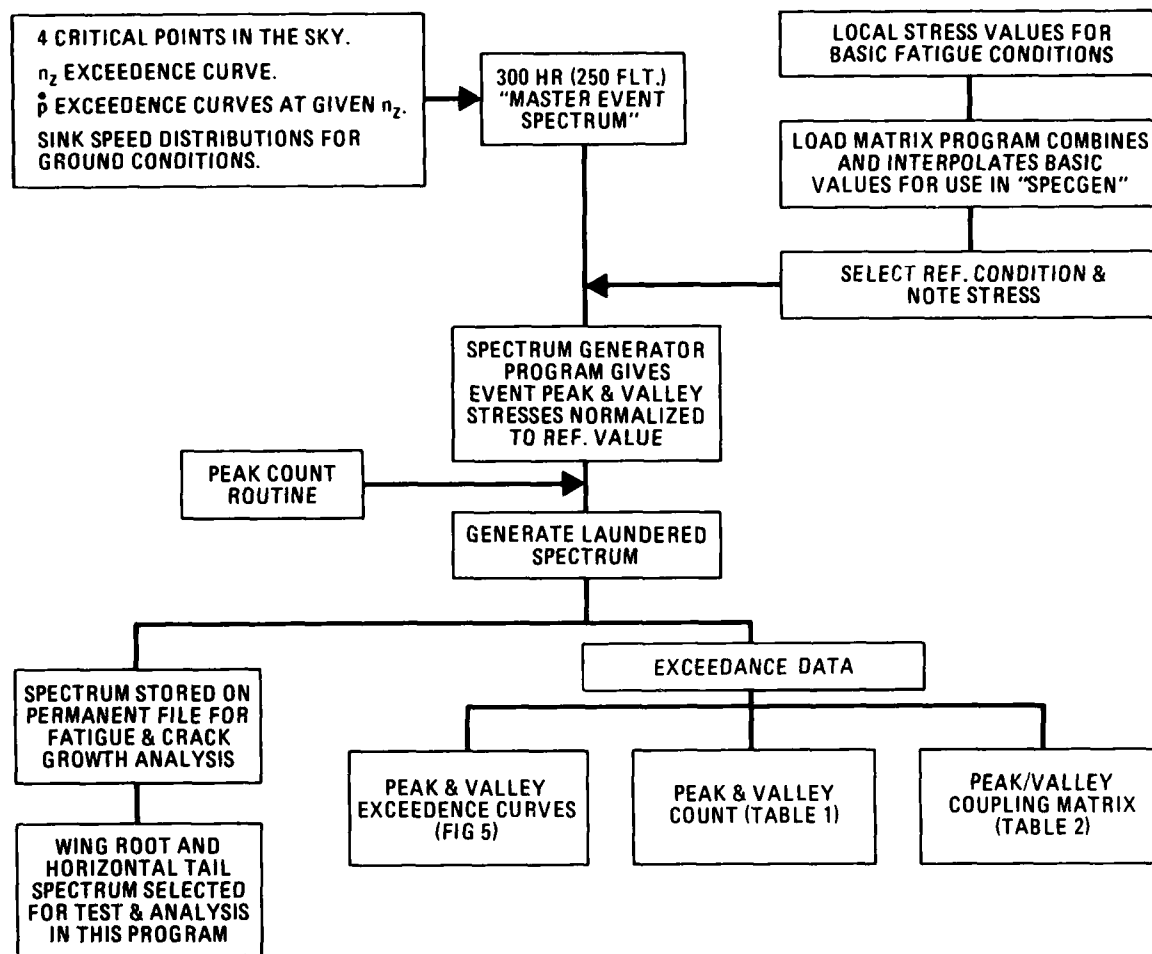
FIGURE 4. SPECTRUM GENERATION PROCEDURE

4 CRITICAL POINTS IN THE SKY.
n_z **EXCEEDENCE CURVE.**
$\dot{p}$ **EXCEEDENCE CURVES AT GIVEN** n_z.
SINK SPEED DISTRIBUTIONS FOR GROUND CONDITIONS.

→ **300 HR (250 FLT.) "MASTER EVENT SPECTRUM"**

LOCAL STRESS VALUES FOR BASIC FATIGUE CONDITIONS

LOAD MATRIX PROGRAM COMBINES AND INTERPOLATES BASIC VALUES FOR USE IN "SPECGEN"

SELECT REF. CONDITION & NOTE STRESS

SPECTRUM GENERATOR PROGRAM GIVES EVENT PEAK & VALLEY STRESSES NORMALIZED TO REF. VALUE

PEAK COUNT ROUTINE →

GENERATE LAUNDERED SPECTRUM

SPECTRUM STORED ON PERMANENT FILE FOR FATIGUE & CRACK GROWTH ANALYSIS

WING ROOT AND HORIZONTAL TAIL SPECTRUM SELECTED FOR TEST & ANALYSIS IN THIS PROGRAM

EXCEEDANCE DATA

PEAK & VALLEY EXCEEDENCE CURVES (FIG 5)

PEAK & VALLEY COUNT (TABLE 1)

PEAK/VALLEY COUPLING MATRIX (TABLE 2)

is also made available in the cycle-by-cycle format. Exceedance data are summarized in the form of a computer graphics plot, a table of peak and valley occurrences (spectral density function), and a tabular matrix of peak-valley couplings both in increments of 5 percent of maximum spectrum load. These summaries for the spectra used are presented in Figure 5 and Tables 1 and 2.

2.6.2 Specimen Preparation

The spectrum fatigue specimens (Figure 6) were machined from T/4 and 3T/4 locations of the aluminum plates in the L-T orientation.
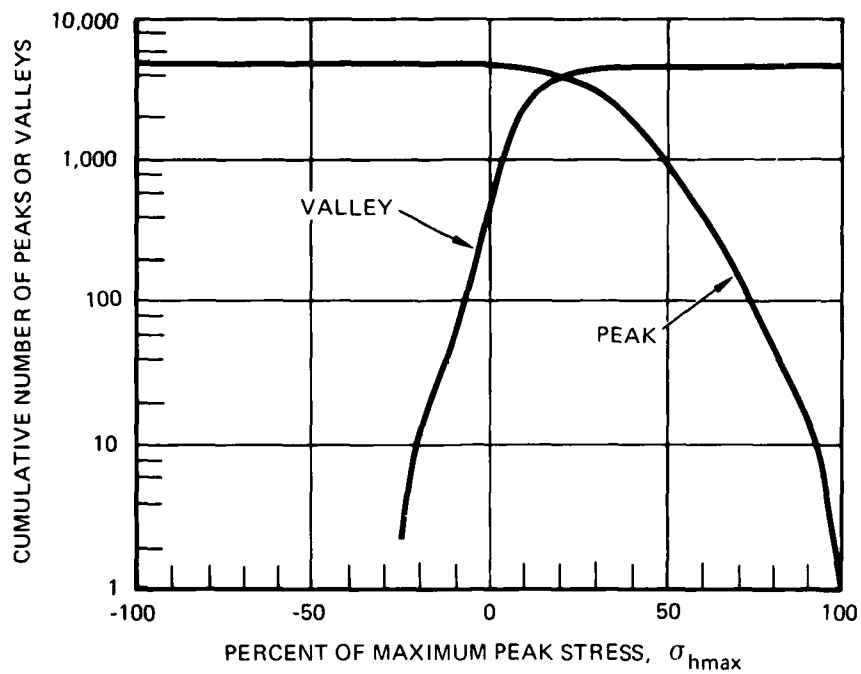
a. TENSION-DOMINATED SPECTRUM (WING ROOT)
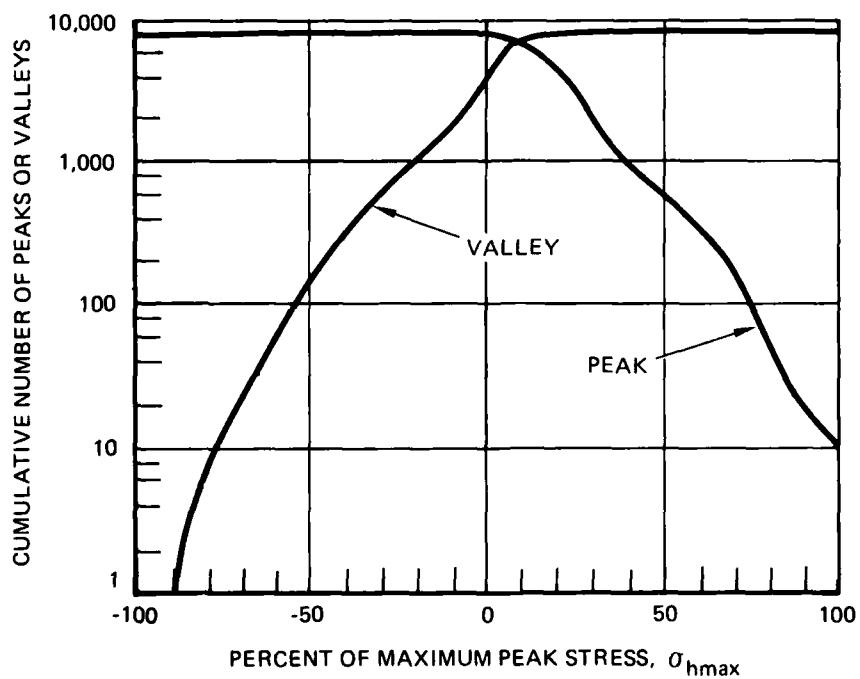
b. TENSION-COMPRESSION SPECTRUM (HORIZONTAL TAIL HINGE)

FIGURE 5. EXCEEDANCE CURVES

13

TABLE 1. SPECTRAL DENSITY FUNCTION

A. TENSION-DOMINATED WING ROOT SPECTRUM[a]

PERCENT OF MAXIMUM PEAK LOAD	NUMBER OF EVENTS			
	PEAKS	VALLEYS	AMPLITUDES[b]	MEAN LEVELS[c]
P = 100	1	—	0	—
95 ≤ P < 100	7	0	0	0
90 ≤ P < 95	8	0	0	0
85 ≤ P < 90	14	0	0	0
80 ≤ P < 85	20	0	0	0
75 ≤ P < 80	42	0	0	0
70 ≤ P < 75	63	0	0	0
65 ≤ P < 70	112	0	0	5
60 ≤ P < 65	189	1	0	15
55 ≤ P < 60	123	1	0	17
50 ≤ P < 55	367	2	2	60
45 ≤ P < 50	379	3	12	144
40 ≤ P < 45	560	11	24	351
35 ≤ P < 40	770	42	89	620
30 ≤ P < 35	978	69	258	943
25 ≤ P < 30	99	169	565	1706
20 ≤ P < 25	168	305	1085	2198
15 ≤ P < 20	98	437	2274	1355
10 ≤ P < 15	335	589	2290	453
5 ≤ P < 10	372	1192	1210	1348
0 ≤ P < 5	0	1345	1601	187
-5 ≤ P < 0	0	404	—	6
-10 ≤ P < -5	0	91	—	2
-15 ≤ P < -10	0	21	—	0
-20 ≤ P < -15	0	11	—	0
-25 ≤ P < -20	0	10	—	0
-30 ≤ P < -25	0	2	—	0
-35 ≤ P < -30	0	0	—	0
-40 ≤ P < -35	0	0	—	0
-45 ≤ P < -40	0	0	—	0
-50 ≤ P < -45	0	0	—	0
-55 ≤ P < -50	0	0	—	0
-60 ≤ P < -55	0	0	—	0
-65 ≤ P < -60	0	0	—	0
-70 ≤ P < -65	0	0	—	0
-75 ≤ P < -70	0	0	—	0
-80 ≤ P < -75	0	0	—	0
-85 ≤ P < -80	0	0	—	0
-90 ≤ P < -85	0	0	—	0
-95 ≤ P < -90	0	0	—	0
-100 < P < -95	0	0	—	0
P = -100	—	0	—	—
TOTALS	4705	4705	9410	9410

[a] SEE FIGURE 3 FOR DEFINITION OF TERMS
[b] ONE HALF OF LOAD RANGE
[c] AVERAGE OF PEAK AND VALLEY LOADS

14

TABLE 1. SPECTRAL DENSITY FUNCTION (CONTINUED)

B. TENSION-COMPRESSION HORIZONTAL TAIL HINGE MOMENT SPECTRUM[a]

PERCENT OF MAXIMUM PEAK LOAD	NUMBER OF EVENTS			
	PEAKS	VALLEYS	AMPLITUDES[b]	MEAN LEVELS[c]
P = 100	10	--	0	--
95 ≤ P < 100	7	0	0	0
90 ≤ P < 95	2	0	0	0
85 ≤ P < 90	22	0	1	0
80 ≤ P < 85	20	0	3	0
75 ≤ P < 80	19	0	0	0
70 ≤ P < 75	84	0	6	0
65 ≤ P < 70	47	0	19	0
60 ≤ P < 65	121	0	79	0
55 ≤ P < 60	3	0	24	5
50 ≤ P < 55	319	0	67	5
45 ≤ P < 50	84	0	154	16
40 ≤ P < 45	398	0	125	50
35 ≤ P < 40	126	0	450	99
30 ≤ P < 35	881	0	423	529
25 ≤ P < 30	2037	0	998	214
20 ≤ P < 25	296	0	1896	563
15 ≤ P < 20	556	0	2077	1383
10 ≤ P < 15	1208	237	4974	4794
5 ≤ P < 10	1273	377	2835	2504
0 ≤ P < 5	201	1621	2373	3127
−5 ≤ P < 0	61	2349	—	1111
−10 ≤ P < −5	37	1288	—	577
−15 ≤ P < −10	16	325	—	261
−20 ≤ P < −15	15	633	—	182
−25 ≤ P < −20	0	210	—	127
−30 ≤ P < −25	1	228	—	66
−35 ≤ P < −30	0	123	—	40
−40 ≤ P < −35	0	140	—	33
−45 ≤ P < −40	0	70	—	9
−50 ≤ P < −45	0	113	—	7
−55 ≤ P < −50	0	49	—	2
−60 ≤ P < −55	0	28	—	0
−65 ≤ P < −60	0	17	—	0
−70 ≤ P < −65	0	17	—	0
−75 ≤ P < −70	0	10	—	0
−80 ≤ P < −75	0	4	—	0
−85 ≤ P < −80	0	1	—	0
−90 ≤ P < −85	0	3	—	0
−95 ≤ P < −90	0	1	—	0
−100 < P < −95	0	0	—	0
P = −100	—	0	—	—
TOTALS	7852	7852	15704	15704

[a]SEE FIGURE 3 FOR DEFINITION OF TERMS
[b]ONE HALF OF LOAD RANGE
[c]AVERAGE OF PEAK AND VALLEY LOADS

15

TABLE 2. PEAK/VALLEY COUPLING MATRIX

A. TENSION-DOMINATED WING ROOT SPECTRUM

a. A VALLEY ASSOCIATED WITH THE PRECEDING PEAK

16

TABLE 2. PEAK/VALLEY COUPLING MATRIX (Continued)

B. TENSION COMPRESSON HORIZONTAL TAIL HINGE MOMENT SPECTRUM

a. A VALLEY ASSOCIATED WITH THE PRECEDING PEAK

36
(1.4) TYP

13 (0.3) TYP

76
(3.0) TYP

38 (1.50) TYP

1.57 (0.062) DIA
HOLE AND
FATIGUE PRECRACK

GRIP
AREA
148
(5.8)
TYP

26 (1.03) DIA

2.00

99 ± 3 (3.9 ± 0.1)

6.3 ± 0.1
(0.247 ± .004)

401
(15.8)

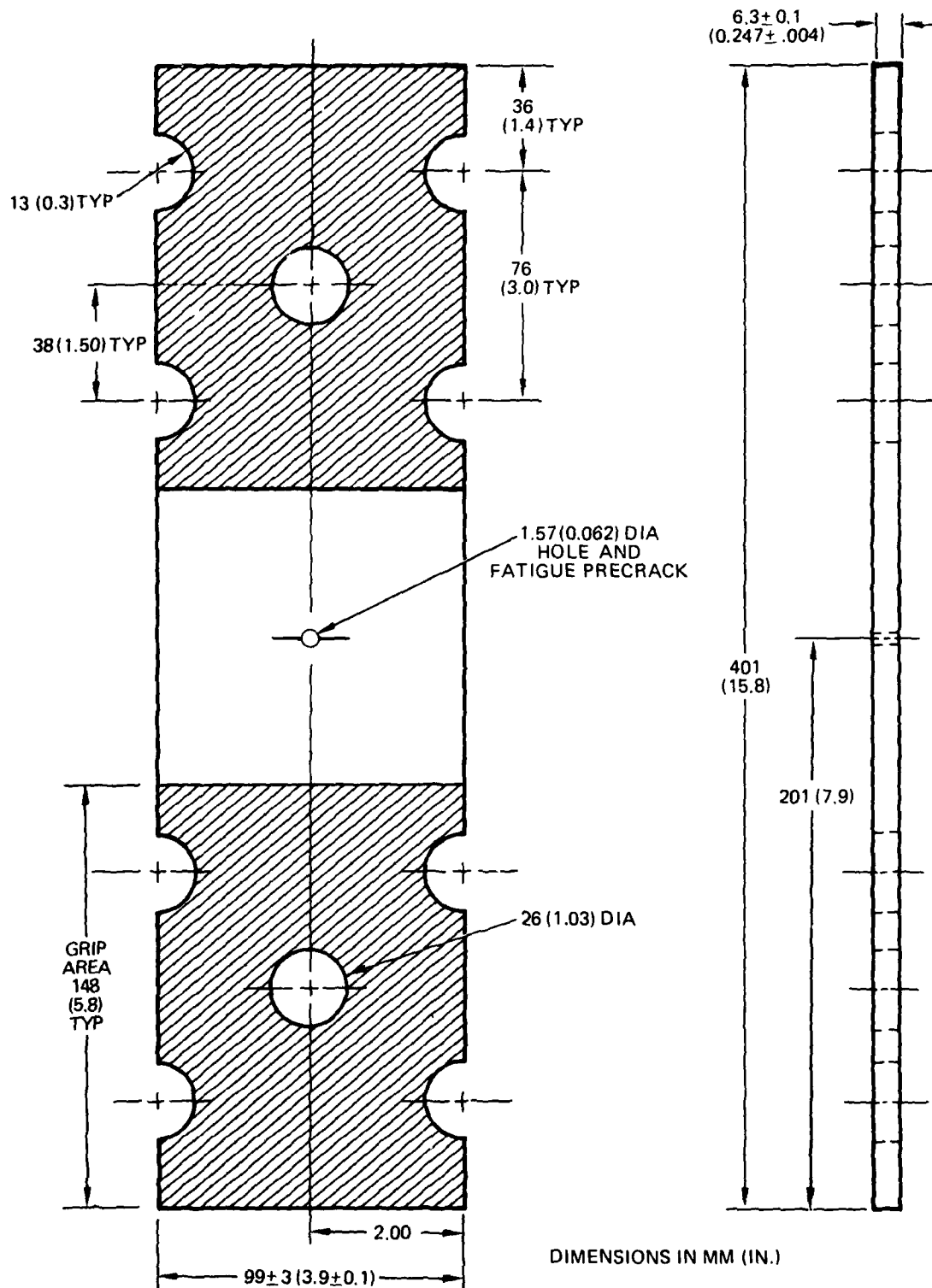201 (7.9)

DIMENSIONS IN MM (IN.)

FIGURE 6. SPECTRUM SPECIMEN

18

The specimen surfaces were polished and grids for measuring crack-lengths were photographically applied on both sides. The grid spacing was 1.27 mm (0.050 inch). Jeweler's saw cuts, 0.2 mm wide and 1 mm deep (0.008 inch wide x 0.04 inch deep), were made at the centrally located hole which provided an adequate "flaw" for precracking the test specimens.

2.6.3 Testing

All spectrum tests were performed on a computer controlled servo-hydraulic machine following the methods of ASTM E647 as appropriate. Precracking was performed under constant amplitude fatigue loading at a stress ratio (R) of 0.1. All of the specimens for testing at the same maximum peak (gross) stress (σ_{hmax}) were precracked with identical loads and for the final stage of precracking the maximum stress was approximately half of the subsequent maximum peak spectrum stress (σ_{hmax}). The final precrack length, a, was targeted for 5 mm (0.2 in.). The relative humidity for all spectrum testing was between 40 and 60 percent.

The load history data are stored on a magnetic tape. The stored data contain all the necessary information, including the desired waveform, frequency, and load points, to control the test. The test setup is shown in Figure 7. Restraints were used to prevent buckling at high compressive loads.

The spectrum tests were performed using a sinusoidal waveform. The linear (theoretical) point-to-point load rate (peak to valley or valley to peak) for tests at each maximum peak stress (σ_{hmax}) was constant. The choice of load rates was primarily governed by the test system response and is shown in Table 3. The maximum frequencies shown in this table, which overrode the loading rate when necessary, insured that even the very small load excursions were applied to the specimens.

A special feature termed Null Pacing was used to insure that peak loads were obtained. When the error between command and feedback exceeded about one percent, computer command rate automatically slowed down so that the peak and valley loads were met and overshoots did not occur.

Spectrum testing was conducted at three maximum peak stresses (σ_{hmax}) of 103, 145, and 169 MPa (15, 21, and 24.5 ksi), selected to give a range of crack growth rates. For the F-18, the maximum peak stress level of 145 MPa corresponds to the lowest stress level that will meet test needs for design purposes.

19
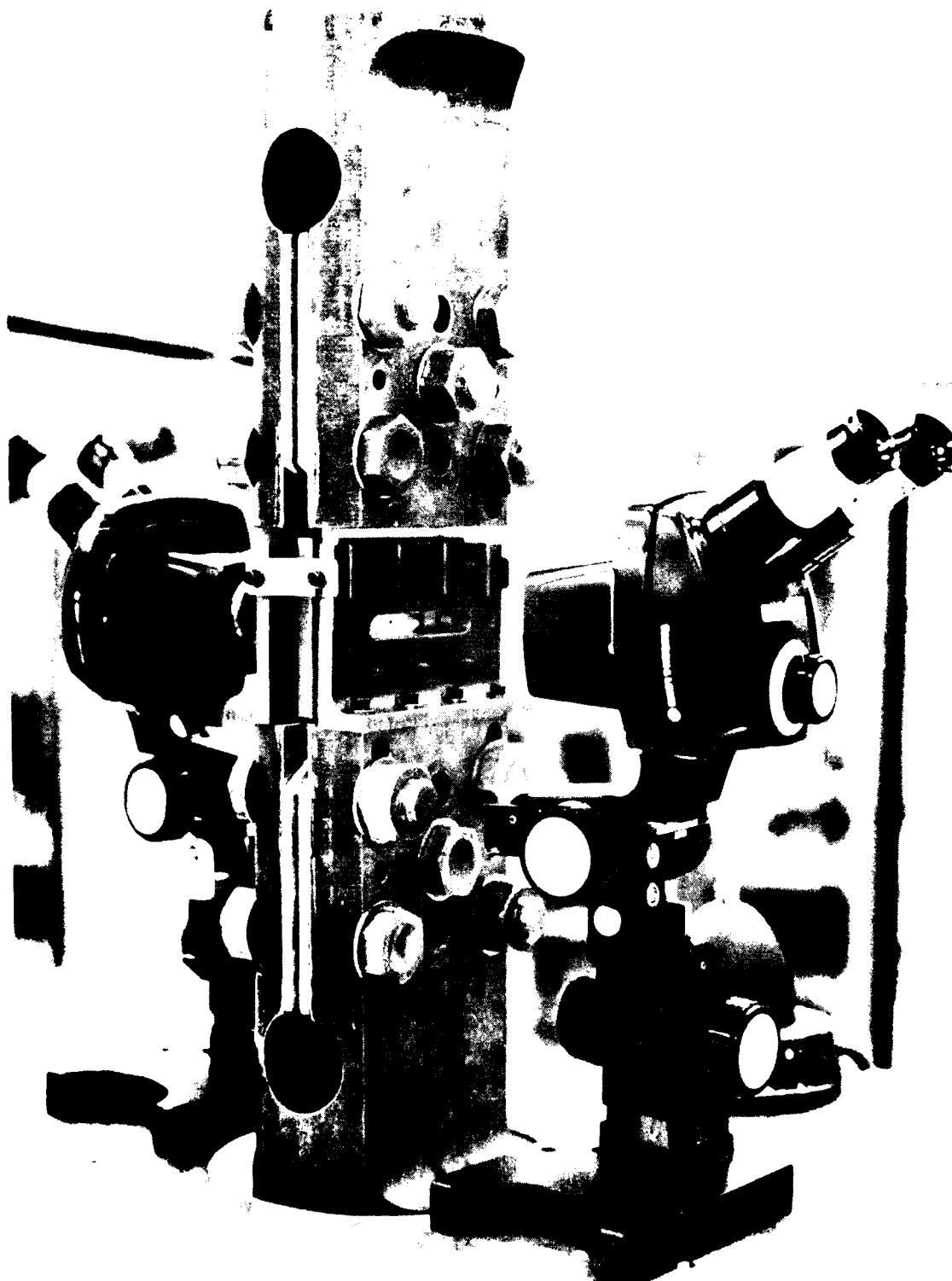
FIGURE 7 SPECTRUM TEST SETUP

80 03800 11

20

To obtain more understanding of the fundamental parameters affecting spectrum FCP, tests were performed at lower and higher maximum peak stresses of 103 and 169 MPa. For the 103 MPa (15 ksi) maximum peak stress tests, the specimens were tested to a crack length of about 14 mm (0.55 in.) i.e., a total crack length, 2a, of about 28 mm (1.1 in.). Subsequently, the same specimen was tested to failure under a maximum peak stress of 169 MPa (24.5 ksi).

TABLE 3. SPECTRUM TEST CONDITIONS

MAXIMUM PEAK STRESS, σ_{hmax}	LINEAR POINT-TO-POINT LOAD RATE		OVERRIDING MAXIMUM FREQUENCY
MPa (ksi)	kN/SEC	(KIP/SEC)	(Hz)
103 (15)	270	(60)	30
145 (21)	220	(50)	20
169 (24.5)	180	(40)	15

Crack length measurements were visually made after each pass for the spectrum tests conducted under maximum peak stress of 145 and 169 MPa (21 and 24.5 ksi). Due to the slower crack growth rates at the 103 MPa (15 ksi) maximum peak stress, the crack length measurements were made after multiple passes. Crack length measurements were made with reference to the photographically printed grid lines at four locations on the specimen (front and rear of specimen, right and left tip of crack). The accuracy of a reading was enhanced by the use of a zoom stereo microscope (7-30X) equipped with a 0.025 mm (0.001 inch increment) reticle.

2.6.4 Test Analysis Procedure

The two-point secant method was used to determine crack growth rate per ASTM E647. To eliminate previous loading history effects, data points with crack growth rates greater than the first minimum crack growth rate were not plotted on the crack growth rate curves.

For comparison of the different materials, the lives (simulated flight hours) over the same crack length regime were used, for example, for tests at 145 MPa (21 ksi), the number of flight hours for the crack to grow from an initial

crack-length, a_i, of 5.5 mm (0.22 in.) to a final crack-length, a_f, of 27.0 mm (1.06 in.) was used. Figure 8 shows schematically the crack-length regimes for different maximum peak stresses (σ_{hmax}). In addition, for the 145 MPa (21 ksi) and 169 MPa (24.5 ksi) tests, life from a_i to failure (F) is listed. A comparison of ranges of the maximum peak stress intensities that these crack growth regimes represent is shown graphically in Figure 9.
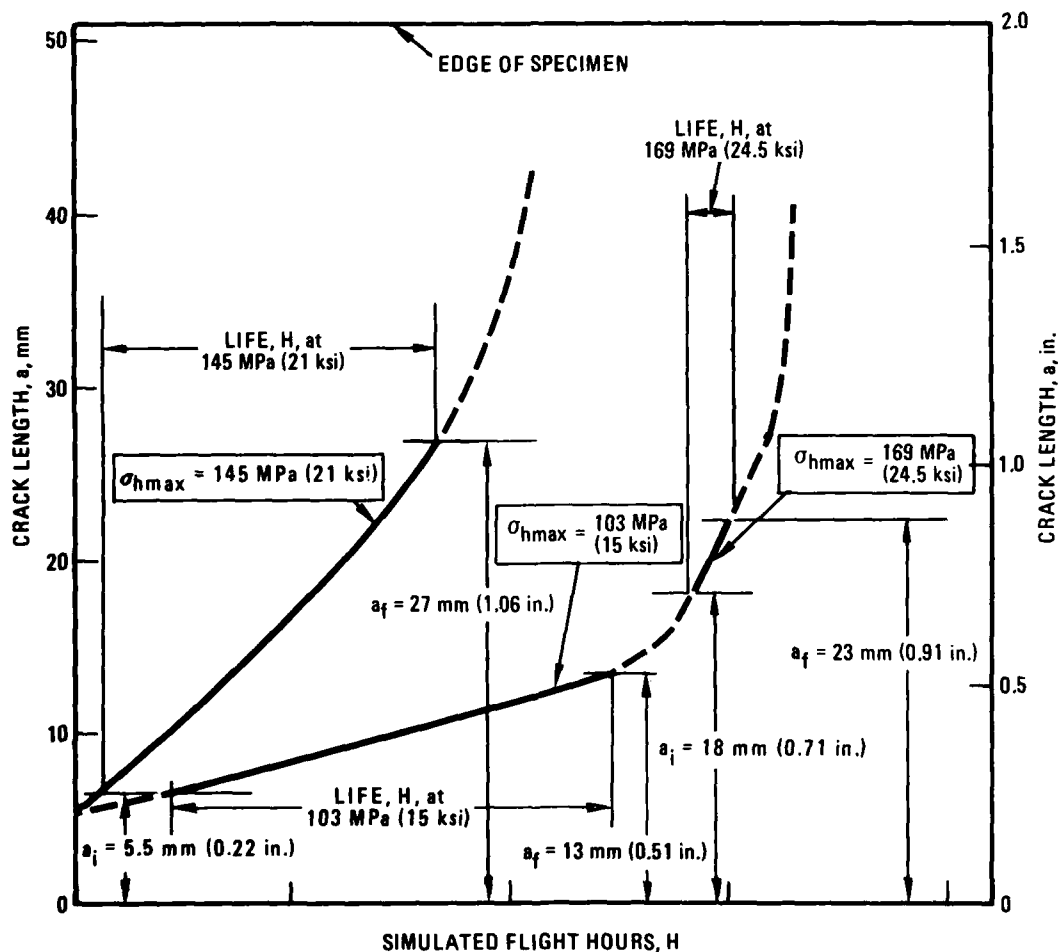

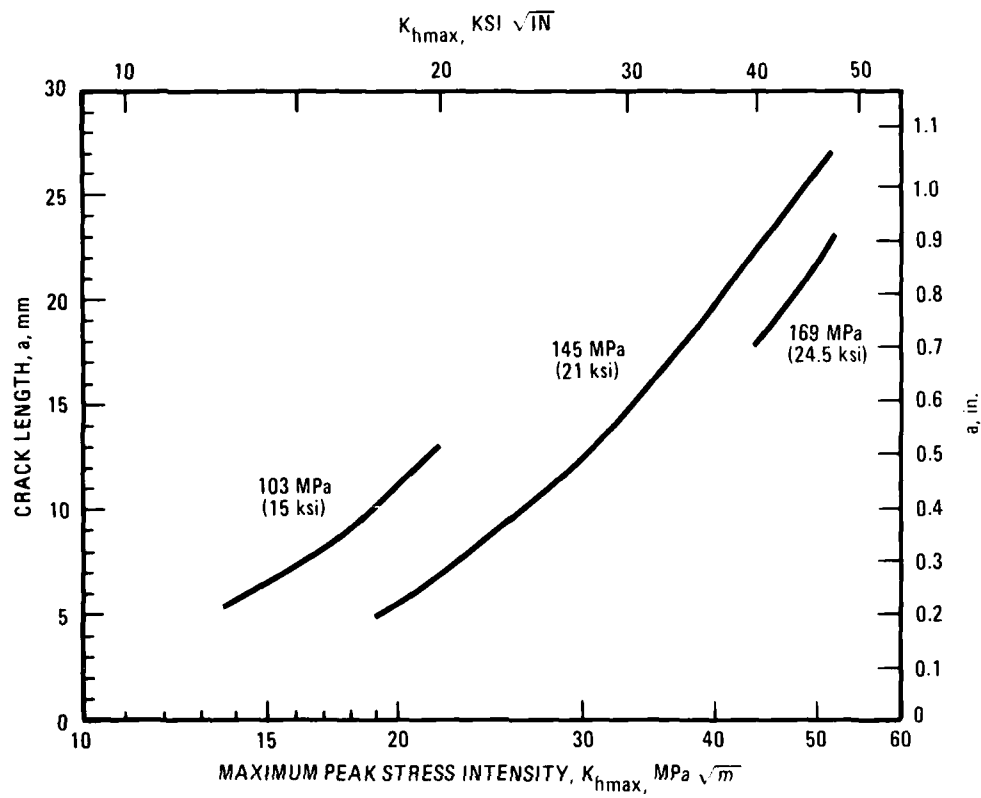FIGURE 8. SCHEMATIC OF SPECTRUM LIFE COMPARISON PROCEDURE

FIGURE 9. COMPARISON OF RANGES OF K_{hmax} VS a FOR THE
THREE VALUES OF σ_{hmax} USED IN THE PROGRAM

III. RESULTS AND DISCUSSION

3.1 CHEMISTRY

The chemical compositions of the program materials are shown in Table 4. Also shown is the required commercial composition limits for each alloy. Each plate met the appropriate composition requirements.

3.2 METALLOGRAPHY

The materials investigated in this program are commercial plate products that have been well characterized in the literature. The purpose of the section is to summarize the microstructural features of these alloys generically with some reference to specific details of the samples from the plates used.

The mechanical properties of heat treatable aluminum alloy plate products are determined primarily by the type, size, and distribution of second-phase particles and by grain structure. Second-phase particles in these alloys are usually categorized into three groups: (1) large (approximately 1 to 30 μm), brittle constituent particles formed during solidification by combination of impurity elements (Fe, Si) and solute elements; (2) smaller (0.02 to 0.3 μm), dispersoid particles formed by solid state precipitation of Cr, Zr or Mn at temperatures above about 425C; and (3) fine (0.0005 to 0.01 μm) precipitates, containing solute elements, formed during quenching or aging. Grain structure includes recrystallized or unrecrystallized grains, subgrain size and shape, texture, and dislocation substructures. These grain structure features generally depend on thermal-mechanical processing history and the size, type, and distribution of second-phase particles, particularly dispersoids.

Optical metallography was used to examine constituents and overall grain structure. Optical micrographs of the three 2X24 alloy plates are shown in Figures 10, 11, and 12. For each alloy, the upper micrograph was obtained from as-polished or slightly etched specimens to show the distribution of secondary intermetallic particles; the lower micrograph represents a standard etching

TABLE 4. CHEMICAL COMPOSITION OF PROGRAM MATERIALS

MATERIAL	SAMPLE NO.	LIMITS	ELEMENT, WEIGHT PERCENT									
			Cu	Mg	Zn	Mn	Cr	Zr	Ti	Be	Fe	Si
2024-T351	511338		4.35	1.54	0.07	0.51	0.00	–	0.03	–	0.23	0.09
–T851	511339		4.41	1.50	0.09	0.50	0.00	–	0.02	–	0.33	0.10
		MINIMUM	3.8	1.2	–	0.30	–	–	–	–	–	–
		MAXIMUM	4.9	1.8	0.25	0.9	0.17	–	0.15	–	0.50	0.50
2124-T851	511340		4.21	1.46	0.03	0.47	0.00	–	0.01	–	0.10	0.05
		MINIMUM	3.8	1.2	–	0.30	–	–	–	–	–	–
		MAXIMUM	4.9	1.8	0.25	0.9	0.10	–	0.15	–	0.30	0.20
7075-T7351	511341		1.95	2.63	5.79	0.04	0.18	–	0.04	–	0.27	0.09
		MINIMUM	1.2	2.1	5.1	–	0.18	–	–	–	–	–
		MAXIMUM	2.0	2.9	6.1	0.30	0.28	–	0.20	–	0.50	0.40
7050-T73651	511464		2.23	2.30	6.27	0.02	0.01	0.12	0.03	0.002	0.13	0.07
		MINIMUM	2.0	1.9	5.7	–	–	0.08	–	–	–	–
		MAXIMUM	2.6	2.6	6.7	0.10	0.04	0.15	0.06	0.05	0.15	0.12
7475-T651	511463		1.48	2.36	5.46	0.00	0.21	–	0.02	0.002	0.07	0.04
–T7351	511630		1.6	2.43	5.67	0.00	0.17	–	0.02	0.001	0.06	0.05
		MINIMUM	1.2	1.9	5.2	–	0.18	–	–	–	–	–
		MAXIMUM	1.9	2.6	6.2	0.06	0.25	–	0.06	0.05	0.12	0.1
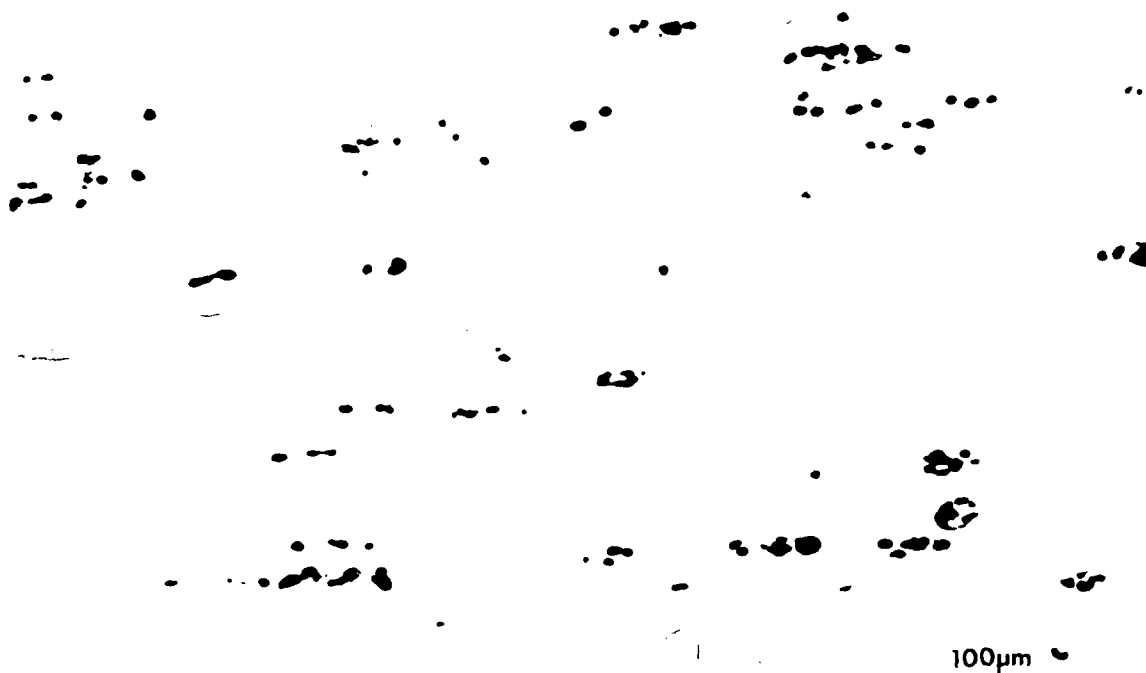
LIGHT KELLER'S ETCH   81-04473-4   500X

100μm
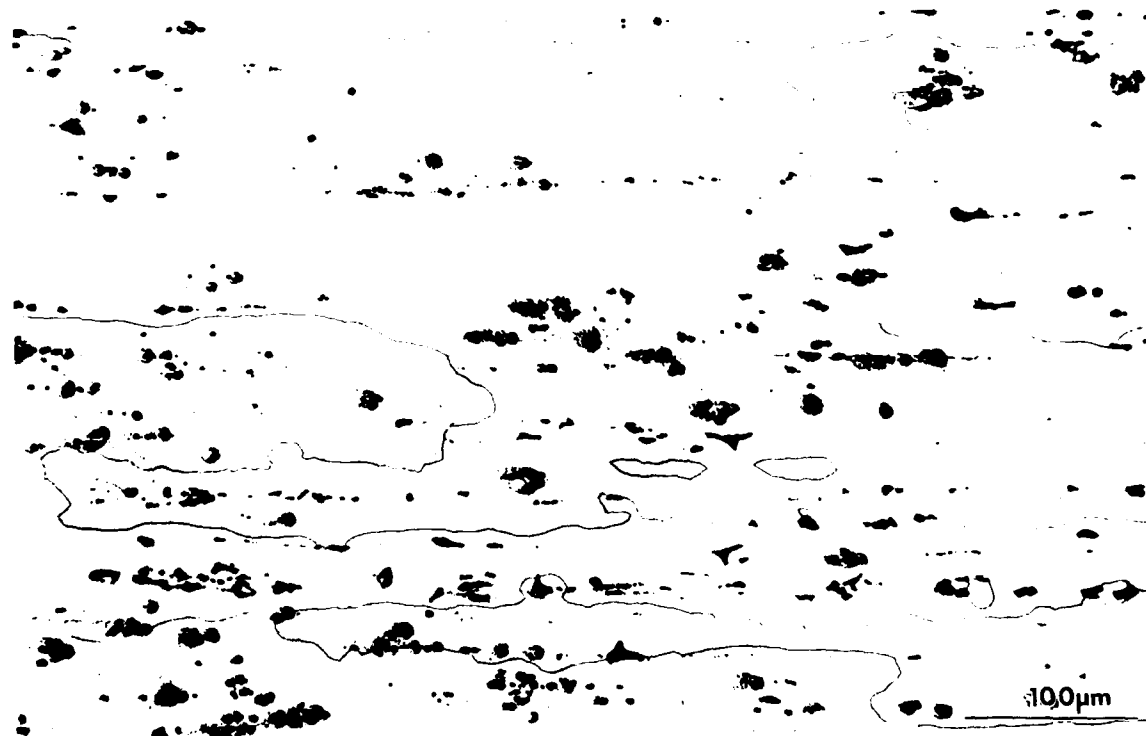
KELLER'S ETCH   81-04473-3A   250X

100μm

FIGURE 10. LONGITUDINAL MICROSTRUCTURE OF 2024-T351
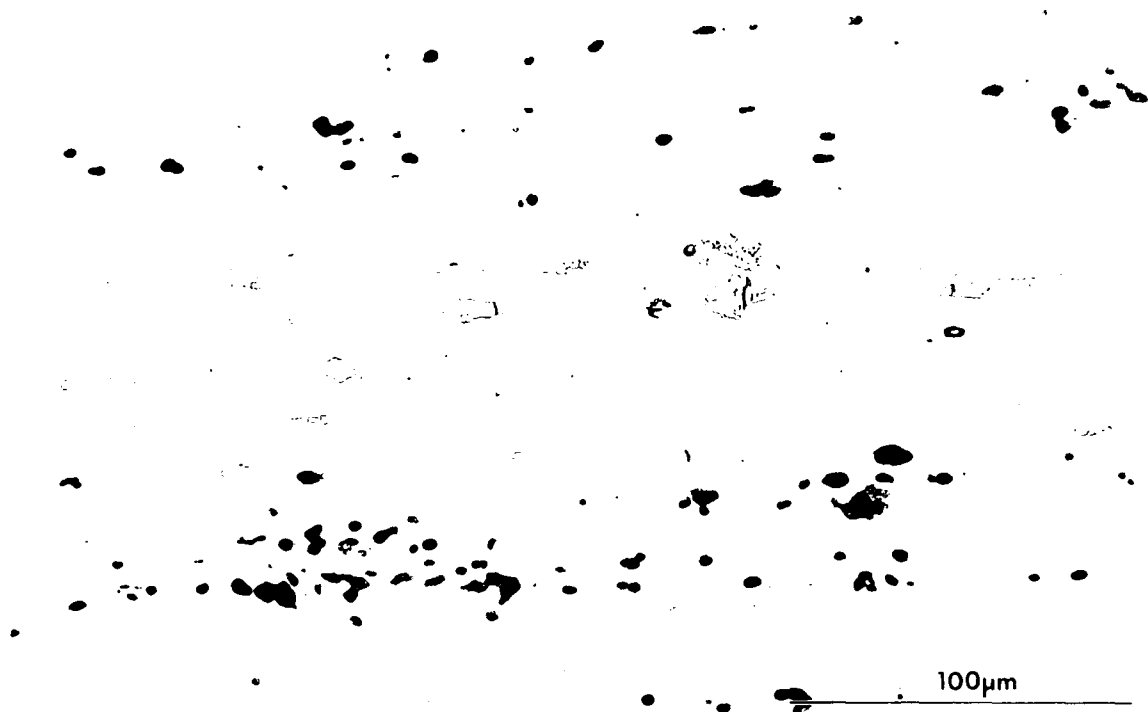
26

LIGHT KELLER'S ETCH   81-04473-14A   500X

KELLER'S ETCH   81-04473-13A   250X
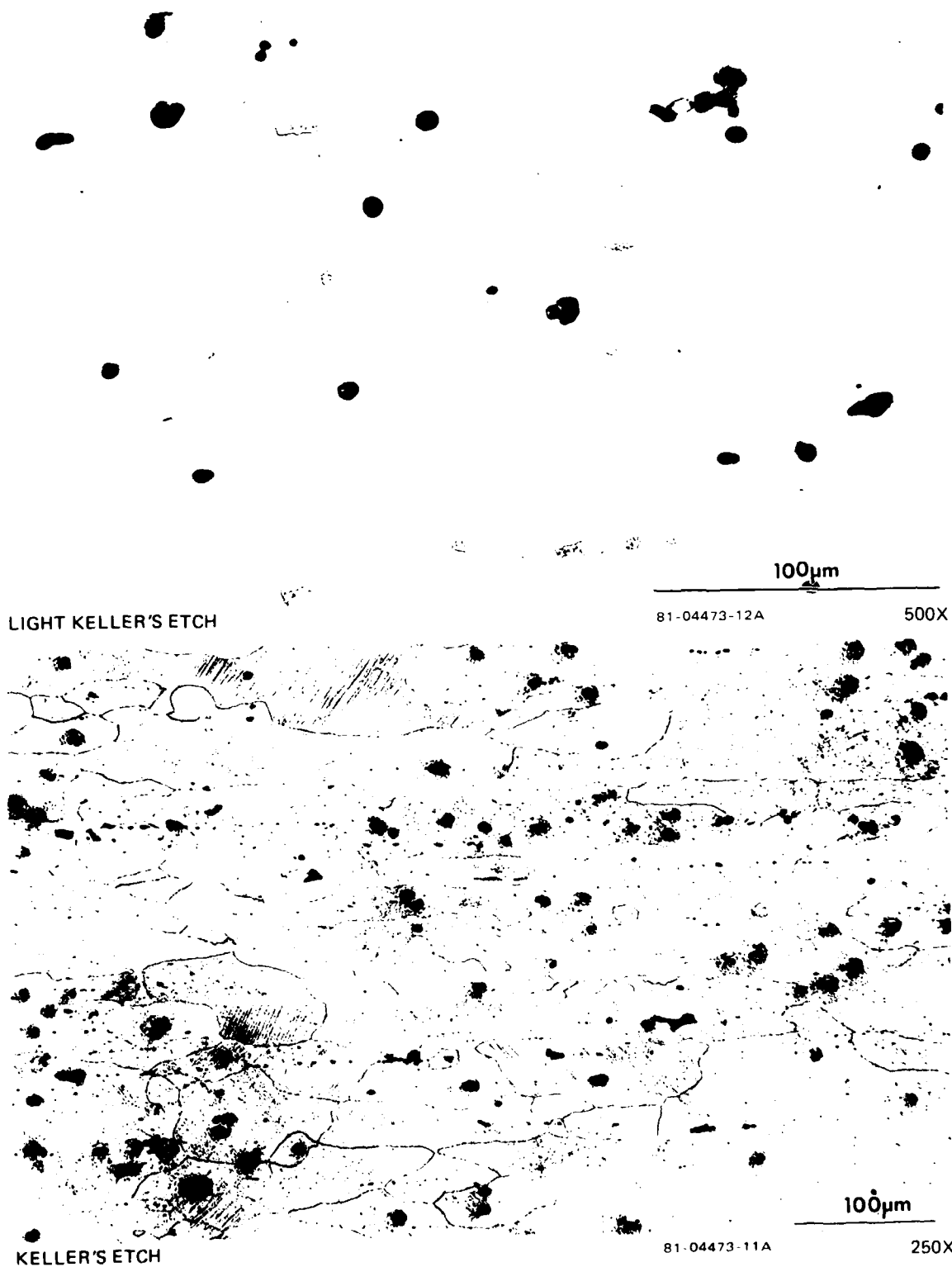
FIGURE 11. LONGITUDINAL MICROSTRUCTURE OF 2024-T851

27

LIGHT KELLER'S ETCH

100μm

81-04473-12A   500X

KELLER'S ETCH

100μm

81-04473-11A   250X

FIGURE 12. LONGITUDINAL MICROSTRUCTURE OF 2124-T851

technique to reveal grain structure. All three contain Fe(Mn)-bearing insoluble constituents, either $Al_{12}(Fe, Mn)_3Si$ or Al_7Cu_2Fe, and partially soluble Mg_2Si and Al_2CuMg constituents. The two 2024 samples contain similar amounts of these phases. Because of its lower Fe and Si contents, the 2124 plate contains far fewer constituent particles.

Grain structures of these three samples are similar – partially recrystallized with fully recovered high angle boundaries outlining areas of recovered and partially recrystallized substructure. Past experience indicates that relatively equiaxed subgrains would be found in these areas along with relatively large (approximately $0.3\,\mu m$) incoherent $Al_{20}Cu_2Mn_3$ dispersoids.

Hardening precipitates for 2X24-type alloys are based on the following precipitation sequence:

$$SS \rightarrow GP \rightarrow S' \rightarrow S \quad (Al_2CuMg)$$
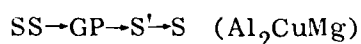
Normally, T3-type tempers contain GP zones while T8-type tempers contain needle-like S' precipitates. Examples of the appearance of these S' precipitates and of the Mn-bearing dispersoids are shown in the TEM micrograph presented in Figure 13.

For the 7XXX alloys, representative optical micrographs for each are shown in Figures 14 through 17. Constituents in these alloys are the insoluble Al_7Cu_2Fe, partially soluble Mg_2Si, and soluble Al_2CuMg-types. All of these phases are found in the 7075 plate. Much smaller amounts of the Fe and Si-bearing phases are found in the 7475 and 7050 samples because of the lower Fe and Si contents in these alloys. Also, lesser amount of Al_2CuMg (S phase) constituent is found in the 7475 plate due to differences in thermal processing. A somewhat greater amount of S phase is found in the 7050 sample because of this alloy's higher Cu content. All four samples appear fully recovered with varying degrees of recrystallization. Both fully recovered high-angle boundaries and well-defined subgrains are found in each plate, although the subgrain size in the 7050 material was greater. Past experience indicates that the dispersoids in both the 7075 and 7475 plates are large (approximately $0.1\,\mu m$) incoherent $Al_{12}Mg_2Cr$ phase. In contrast, 7050 contains small (approximately $0.02\,\mu m$) fully coherent Al_3Zr dispersoids. Hardening precipitates in these 7XXX alloys are similar and based on the following precipitation sequence.
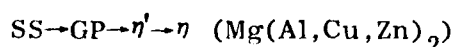
$$SS \rightarrow GP \rightarrow \eta' \rightarrow \eta \quad (Mg(Al,Cu,Zn)_2)$$

29

81-04473-17A   44,000X

**FIGURE 13. TEM MICROGRAPH OF 2024–T851 PLATE SHOWING ROD-LIKE
Mn–BEARING DISPERSOIDS AND NEEDLE-LIKE S′ PRECIPITATES**

The T651 temper is normally characterized by a mixture of GP and η' while the T7351 and T73651 tempers normally contain both η' and η precipitates. Examples of the appearance of these features are shown in the TEM micrographs presented in Figures 18, 19, and 20.
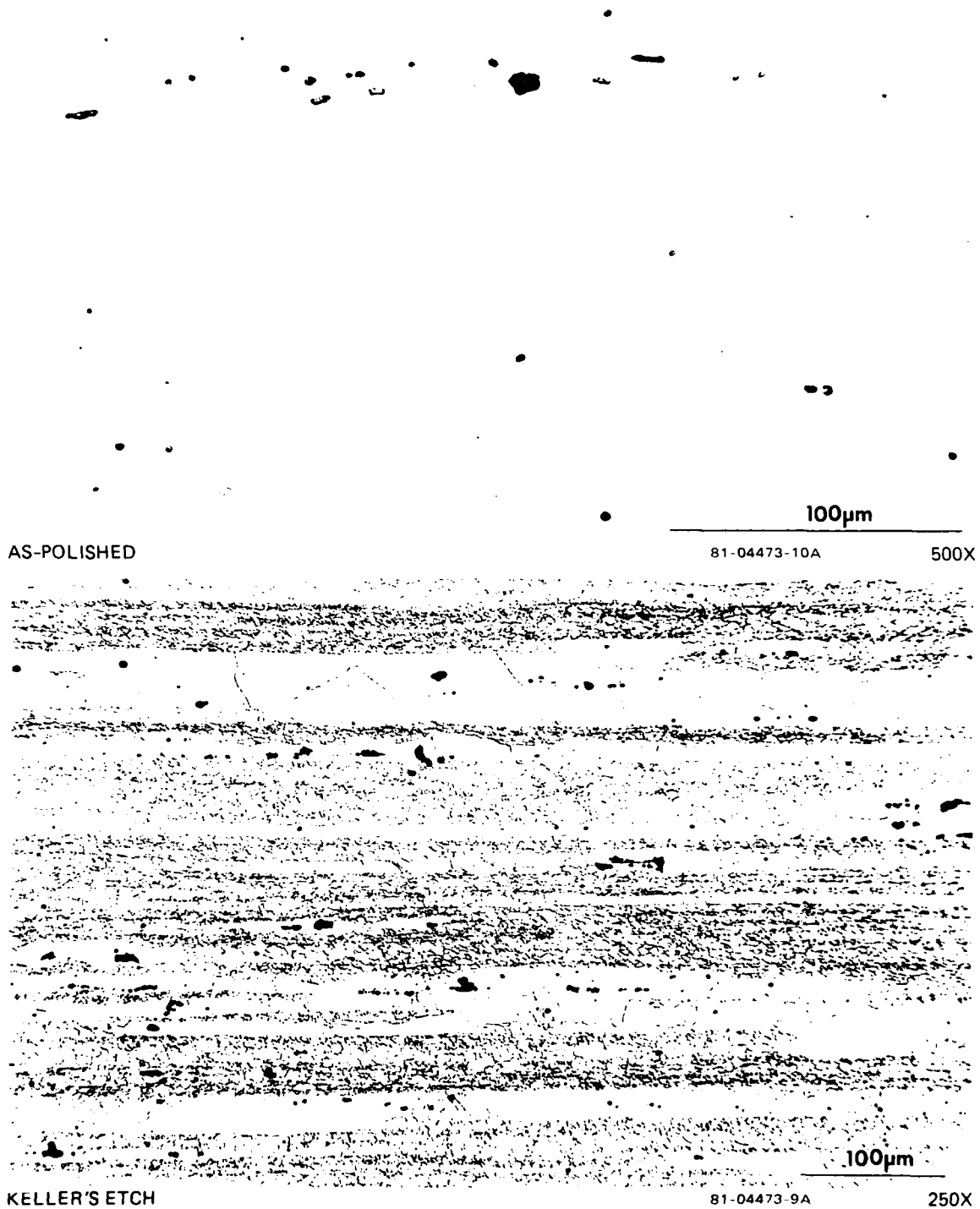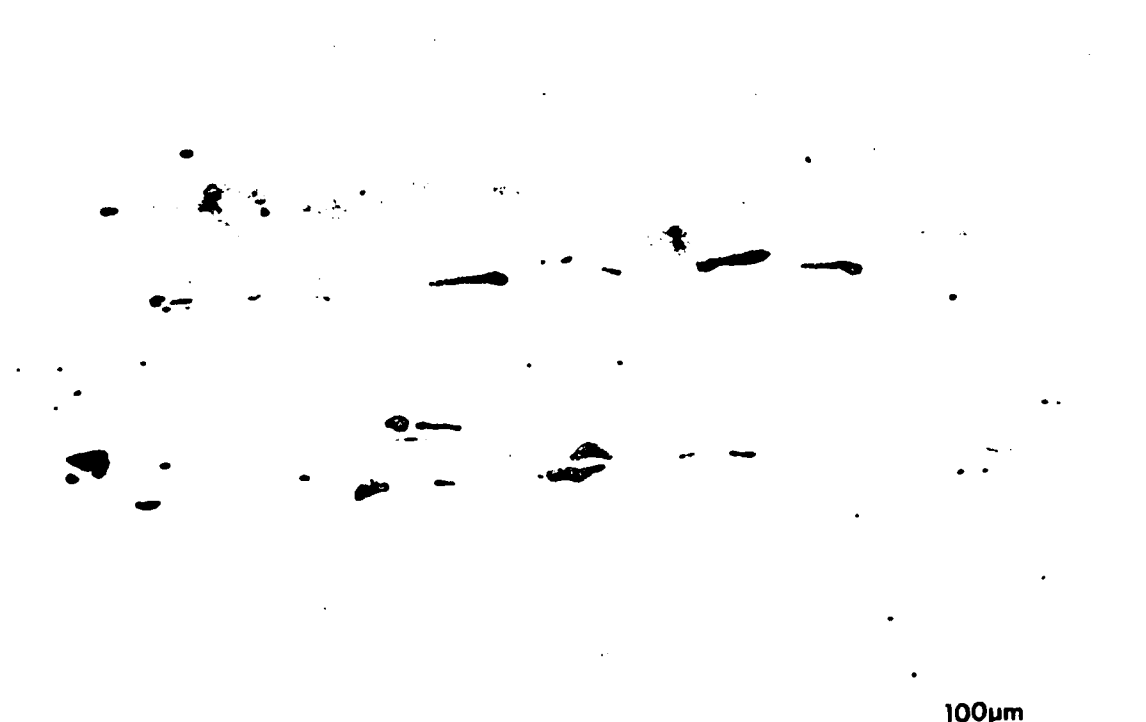
AS-POLISHED   81-04473-10A   500X

KELLER'S ETCH   81-04473-9A   250X
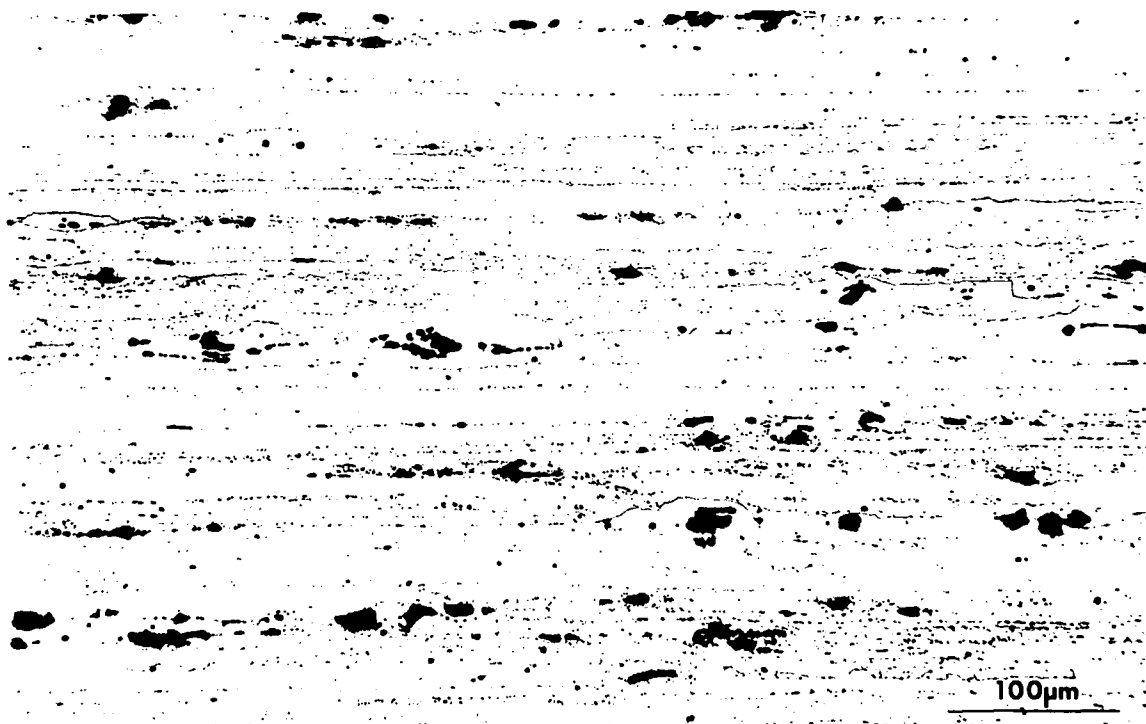
FIGURE 14. LONGITUDINAL MICROSTRUCTURE OF 7050-T73651

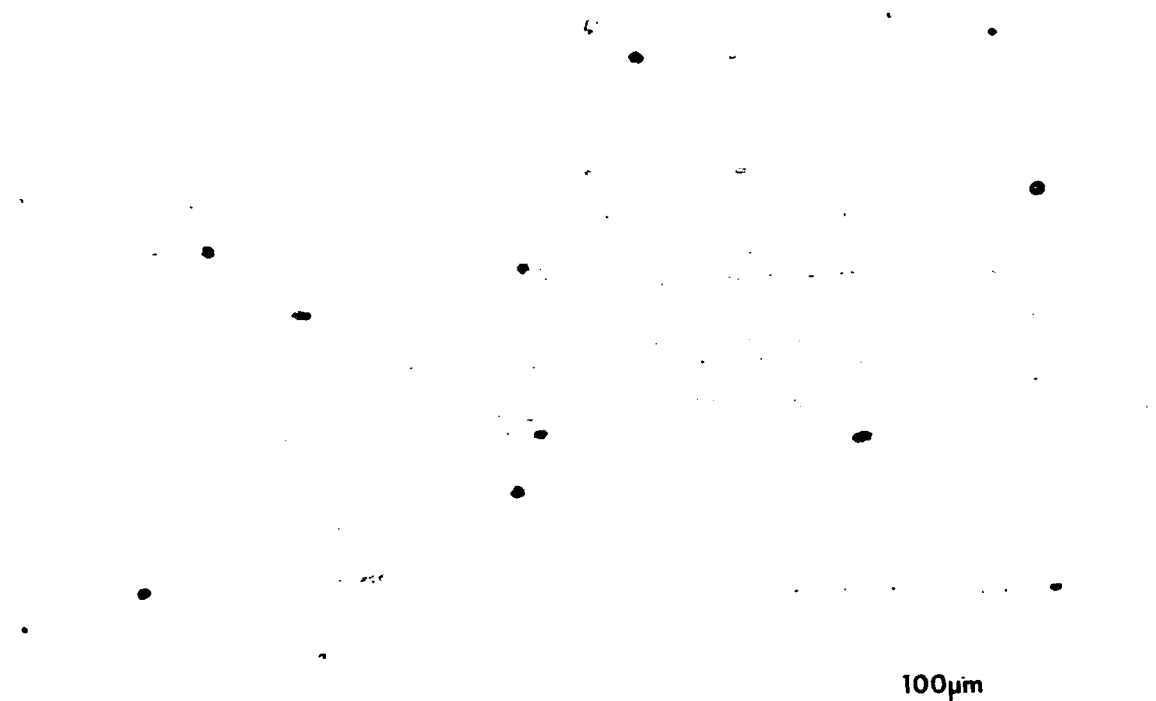AS-POLISHED   81-04473-8A   500X

100μm

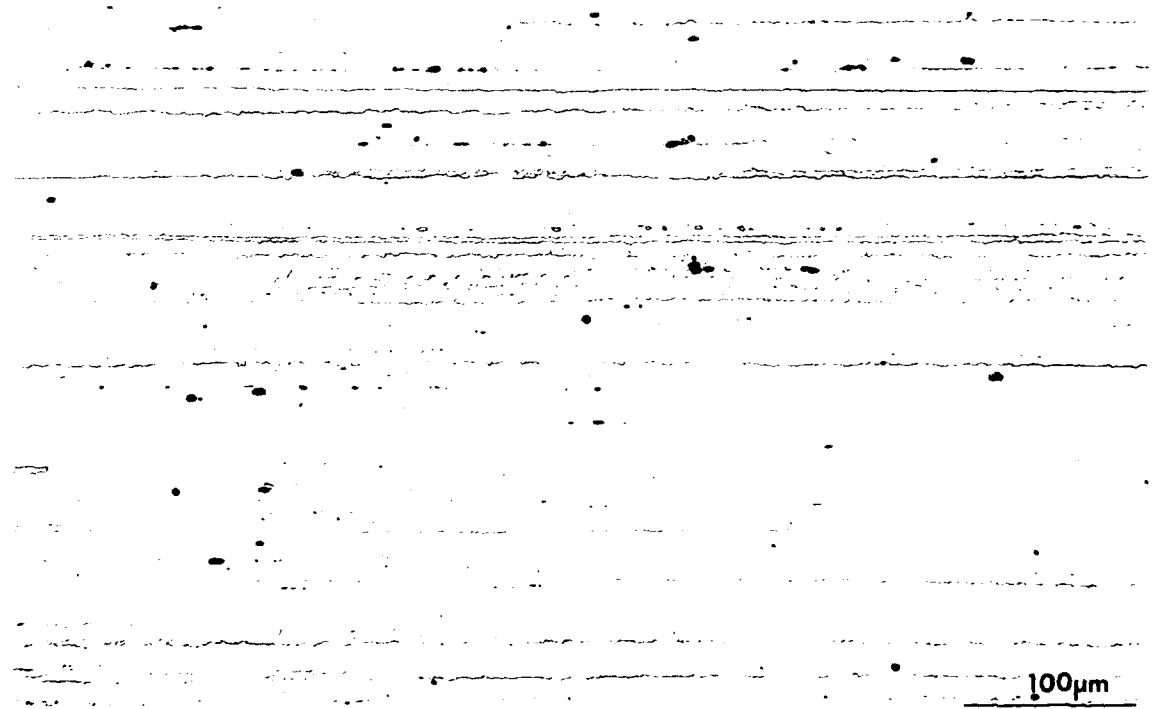KELLER'S ETCH   81-04473-7A   250X

100μm

FIGURE 15. LONGITUDINAL MICROSTRUCTURE OF 7075-T7351

32

100μm

AS-POLISHED   81-04473-6A   500X

100μm

KELLER'S ETCH   81-04473-5A   250X

FIGURE 16. LONGITUDINAL MICROSTRUCTURE OF 7475-T651

AS-POLISHED

100µm

81 04473-2A   500X

GRAFF-SARGENT ETCH

100µm

81 04473 1A   250X

FIGURE 17. LONGITUDINAL MICROSTRUCTURE OF 7475-T7351

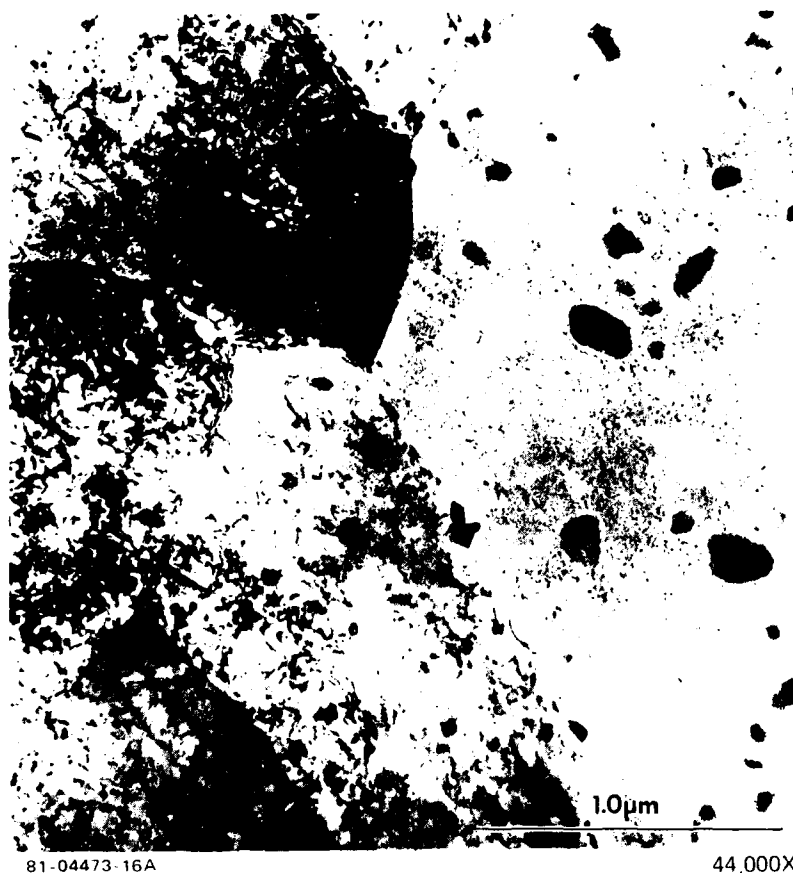81-04473-16A   44,000X

**FIGURE 18. TEM MICROGRAPH OF 7075-T651 PLATE SHOWING LARGE Cr-BEARING
DISPERSOIDS, SUBGRAINS, AND STRENGTHENING PRECIPITATES. BACKGROUND
DISLOCATIONS WERE PRODUCED BY THE STRETCHING OPERATION USED
FOR RESIDUAL STRESS RELIEF.**

81-04473-18A

39,000X

FIGURE 19. TEM MICROGRAPH OF 7075-T7351 PLATE SHOWING INCREASED
PRECIPITATE SIZE OVER THE T6 TEMPER MATERIAL

81-04473-15A   39,000X

FIGURE 20. TEM MICROGRAPH OF 7050-T73651 PLATE SHOWING SUBGRAINS AND
RELATIVELY LARGE STRENGTHENING PRECIPITATES

3.3 TENSILE RESULTS

Tensile tests were conducted on specimens from each plate taken in the longitudinal direction from the center (T/2), quarter thickness (T/4 and 3T/4), and near surface (top and bottom) locations.

Tensile test results through the thickness of each plate are shown in Table 5. Typical and minimum tensile properties which represent each of the alloys and tempers investigated are also shown for comparison. The average tensile properties of each plate were near typical, with the exception of the average yield strength of the 2024-T351 plate which was somewhat higher, 39 MPa (6 ksi), than typical.

There was no variation in tensile properties through the thickness of the 2024-T851 and 2124-T851 plates, and only a small variation (no more than 20 MPa (3 ksi) in strength) in the 2024-T351 plate. There were significant variations in the through-the-thickness properties of the 7075-T7351 plate (as much as 46 MPa

37

TABLE 5. SUMMARY OF TENSILE RESULTS — LONGITUDINAL

MATERIAL PLATE THICKNESS MM (IN.)	SPECIMEN LOCATION[a][b]	ULTIMATE STRENGTH MPa	(KSI)	YIELD STRENGTH MPa	(KSI)	ELONGATION IN 4D %[b]	REDUCTION OF AREA %[b]
2024-T351 31.8 (1.25)	TOP SURFACE	467	(68)	364	(53)	17	20
	T/4	450	(65)	360	(52)	19	26
	T/2	470	(68)	–	–	20	24
		470	(68)	372	(54)	19	24
	3T/4	451	(65)	361	(52)	21	24
	BOTTOM SURFACE	464	(67)	365	(53)	18	18
	AVERAGE	462	(67)	364	(53)	15	23
	AVERAGE T/4, 3T/4	451	(65)	360	(52)	20	25
	TYPICAL[c]	470	(68)	325	(47)	17[d]	–
	MINIMUM[c]	435	(63)	290	(42)	7[d]	–
2024-T851 19.0 (0.75)	TOP SURFACE	492	(71)	460	(67)	9	26
	T/4	490	(71)	461	(67)	8	23
	T/2	493	(72)	465	(67)	8	22
		493	(72)	463	(67)	8	23
	3T/4	491	(71)	461	(67)	8	25
	BOTTOM SURFACE	499	(72)	465	(67)	9	23
	AVERAGE	493	(72)	463	(67)	8	24
	AVERAGE T/4, 3T/4	491	(71)	461	(67)	8	24
	TYPICAL[e]	483	(70)	448	(65)	8	–
	MINIMUM[c]	455	(66)	400	(58)	4[d]	–
2124-T851 38.1 (1.5)	TOP SURFACE	486	(70)	456	(66)	11	36
	T/4	488	(71)	457	(66)	10	30
	T/2	486	(70)	457	(66)	10	28
		488	(71)	457	(66)	10	30
	3T/4	487	(71)	455	(66)	10	30
	BOTTOM SURFACE	488	(71)	454	(66)	11	35
	AVERAGE	487	(71)	455	(66)	10	32
	AVERAGE T/4, 3T/4	487	(71)	456	(66)	10	30
	TYPICAL[c]	483	(70)	441	(64)	9	–
	MINIMUM[c]	455	(66)	395	(57)	5[e]	–
7050-T73651 25.4 (1.0)	TOP SURFACE	520	(75)	462	(67)	15	40
	T/4	535	(78)	478	(69)	15	33
	T/2	555	(80)	504	(73)	14	32
		553	(80)	500	(73)	13	32
	3T/4	534	(77)	478	(69)	15	35
	BOTTOM SURFACE	518	(75)	466	(68)	15	35
	AVERAGE	536	(78)	481	(70)	15	34
	AVERAGE T/4, 3T/4	534	(77)	478	(69)	15	34
	TYPICAL[f]	510	(74)	455	(66)	11	–
	MINIMUM[f]	490	(71)	427	(62)	9	–
7075-T7351 25.4 (1.0)	TOP SURFACE	486	(70)	409	(59)	14	33
	T/4	502	(73)	429	(62)	12	28
	T/2	526	(76)	453	(66)	11	24
		527	(76)	454	(66)	11	24
	3T/4	502	(73)	431	(63)	13	28
	BOTTOM SURFACE	488	(71)	408	(59)	14	31
	AVERAGE	505	(73)	431	(62)	13	28
	AVERAGE T/4, 3T/4	502	(73)	430	(62)	13	28
	TYPICAL[e]	503	(73)	434	(63)	13	–
	MINIMUM[c]	475	(69)	390	(57)	6[d]	–

FOOTNOTES ON NEXT PAGE

38

TABLE 5. SUMMARY OF TENSILE RESULTS – LONGITUDINAL (CONTINUED)

MATERIAL PLATE THICKNESS MM (IN.)	SPECIMEN LOCATION[a][b]	ULTIMATE STRENGTH		YIELD STRENGTH		ELONGATION IN 4D %[b]	REDUCTION OF AREA %[b]
		MPa	(KSI)	MPa	(KSI)		
7475-T651 19.0 (0.75)	TOP SURFACE	532	(77)	501	(73)	15	27
	T/4	605	(88)	548	(79)	13	21
	T/2	585	(85)	541	(78)	12	17
		586	(85)	542	(79)	12	17
	3T/4	606	(88)	551	(80)	13	21
	BOTTOM SURFACE	537	(78)	506	(73)	15	22
	AVERAGE	575	(83)	531	(77)	14	21
	AVERAGE T/4, 3T/4	605	(88)	549	(80)	13	21
	TYPICAL[g]	–	–	–	–	–	–
	MINIMUM[g]	531	(77)	469	(68)	8	–
7475-T7351 38.1 (1.5)	TOP SURFACE	493	(71)	423	(61)	17	51
	T/4	511	(74)	441	(64)	17	47
	T/2	529	(77)	464	(67)	15	39
		527	(76)	461	(67)	14	37
	3T/4	514	(75)	444	(64)	17	46
	BOTTOM SURFACE	486	(70)	420	(61)	17	47
	AVERAGE	510	(74)	442	(64)	16	44
	AVERAGE T/4, 3T/4	513	(74)	442	(64)	17	47
	TYPICAL[g]	–	–	–	–	–	–
	MINIMUM[g]	469	(68)	393	(57)	10	–

[a] SPECIMENS TAKEN FROM THE T/2 LOCATION ARE FROM THE CENTER OF THE PLATE THICKNESS AND THOSE FROM THE T/4 AND 3T/4 ARE FROM MIDWAY BETWEEN THE CENTER AND THE TOP SURFACE OR BOTTOM SURFACE, RESPECTIVELY

[b] THE NOMINAL DIAMETER OF THE REDUCED-SECTION OF T/2 SPECIMENS WAS 12.7MM, T/4 AND 3T/4 SPECIMENS WAS 6.4MM, AND SURFACE SPECIMENS WAS 4.1MM

[c] "ALUMINUM STANDARDS AND DATA," THE ALUMINUM ASSOCIATION, 1978

[d] ELONGATION MEASURED OVER 5D

[e] ALCOA ALUMINUM HANDBOOK, 1967

[f] "ALCOA ALLOY 7050," ALCOA GREEN LETTER, ISSUED APRIL 1976

[g] "ALCOA 7475 SHEET AND PLATE," ALCOA GREEN LETTER, ISSUED FEBRUARY 1978

(7 ksi) in strength). The ductility increased from the center toward the surfaces; however, the properties at the T/4 and 3T/4 locations were almost the same and comparable to the typical properties for the 7075-T7351 alloy. There was also a variation in properties through the thickness of both the 7050-T73651 and 7475-T651 plates. The strength through the thickness of the 7050-T73651 plate varied as much as 42 MPa (6 ksi) while the strength through the thickness of the 7475-T651 plate varied as much as 50 MPa (7 ksi). Nevertheless, for all alloys these strengths are above minimums regardless of through-thickness location. For consistency, the constant amplitude and spectrum FCP specimens were obtained only from the T/4 and 3T/4 locations in all plates. The averages of the tensile properties at these locations also are shown in Table 5, and were used for correlation of FCP behavior to yield strength.

3.4 FRACTURE TOUGHNESS RESULTS

Fracture toughness test results are shown in Table 6. All the tests were valid per ASTM E399, except for the 2024-T351 and 7475-T651 alloys. However, these tests are still considered meaningful since only one of the test criteria ($P_{max}/P_Q < 1.1$) was marginally invalid for three of the four tests. All the values were within the acceptance range reported in literature for these alloys.

TABLE 6. FRACTURE TOUGHNESS RESULTS – LT ORIENTATION

ALLOY AND TEMPER	PLATE THICKNESS mm (in.)	SPECIMEN THICKNESS mm	K_Q MPa $\sqrt{m}$ (ksi $\sqrt{in.}$)	VALID K_{IC} PER ASTM E399	AVERAGE VALID K_{IC} OR MEANINGFUL K_Q MPa $\sqrt{m}$ (ksi $\sqrt{in.}$)
2024-T351	31.8 (1.25)	31.8	39 (36)	NO[a]	
		31.8	39 (36)	NO[a]	39 (36)
2024-T851	19.0 (0.75)	18.0	24 (22)	YES	
		18.0	24 (22)	YES	24 (22)
2124-T851	38.1 (1.5)	38.1	33 (30)	YES	
		38.1	33 (30)	YES	33 (30)
7050-T73651	25.4 (1.0)	24.8	39 (36)	YES	
		24.8	39 (36)	YES	39 (36)
7075-T7351	25.4 (1.0)	25.4	32 (29)	YES	
		25.4	32 (29)	YES	32 (29)
7475-T651	19.0 (0.75)	18.0	48 (44)	NO[b]	
		18.0	41 (38)	NO[a]	41 (38)
7475-T7351	38.1 (1.5)	38.1	55 (50)	YES	
		38.1	56 (50)	YES	55 (50)

[a]TEST INVALID PER ASTM E399 SINCE $P_{MAX}/P_Q > 1.10$. HOWEVER, DATA STILL MEANINGFUL, SINCE P_{MAX}/P_Q WAS 1.15

[b]TEST INVALID PER ASTM E399 DUE TO INSUFFICIENT THICKNESS AND FATIGUE CRACK LENGTH

3.5 FATIGUE CRACK GROWTH RESULTS UNDER CONSTANT AMPLITUDE LOADING

Constant-load amplitude, fatigue-crack propagation tests were performed on all seven materials in the near-threshold, intermediate, and high ΔK regimes. Measured FCP rates (da/dN) in the near-threshold regime approached 10^{-10} m/cycle (4×10^{-9} in./cycle). The FCGR data for each alloy are presented in Figures A-2 through A-8 in Appendix A; comparisons of these data are shown in Figures 21 and 22. Figure 21 includes conventional da/dN vs. ΔK curves for all the seven materials. In Table 7 and Figure 22, the FCGR data are presented in terms of the stress intensity necessary to propagate a fatigue crack at a speci- fied growth rate for each material and are grouped into 2000 and 7000 series.
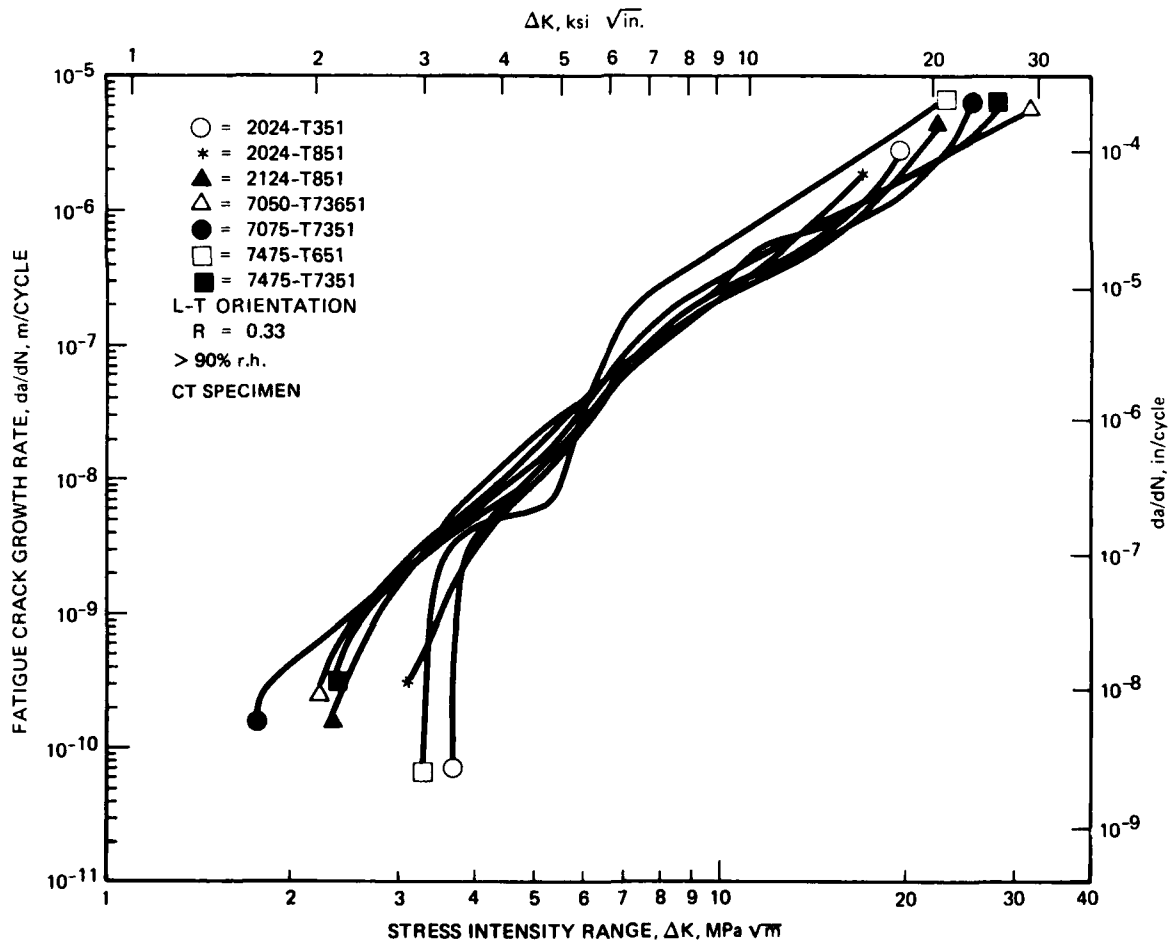
FIGURE 21. COMPARISON OF FATIGUE CRACK GROWTH BEHAVIOR UNDER CONSTANT AMPLITUDE LOADING

FIGURE 22. STRESS INTENSITY NEEDED TO OBTAIN A GIVEN FATIGUE CRACK GROWTH RATE UNDER CONSTANT AMPLITUDE LOADING.
(R = 0.33, >90% rh, L-T ORIENTATION)

The materials within each series have been arranged by the spectrum ranking at 145 MPa (see Section 3.6). In this format, greater resistance to crack growth is indicated by a higher K_{max} magnitude to produce a given da/dN.

Both Figures 21 and 22 show that the variation in FCP resistance among these seven materials was greatest in the near-threshold regime, while for ΔK levels above 4 MPa $\sqrt{m}$, crack growth rates varied only by a factor of 2 to 4. Since crack growth in the near-threshold regime can dominate the fatigue life of an engineering component, these data suggest that selection of alloys with superior near-threshold FCP resistance may result in substantial improvements in fatigue life.

FIGURE 22. STRESS INTENSITY NEEDED TO OBTAIN A GIVEN FATIGUE
CRACK GROWTH RATE UNDER CONSTANT AMPLITUDE LOADING.
(R = 0.33, >90% rh, L-T ORIENTATION)

The materials within each series have been arranged by the spectrum ranking at 145 MPa (see Section 3.6). In this format, greater resistance to crack growth is indicated by a higher K_{max} magnitude to produce a given da/dN.

Both Figures 21 and 22 show that the variation in FCP resistance among these seven materials was greatest in the near-threshold regime, while for ΔK levels above $4 \, MPa\sqrt{m}$, crack growth rates varied only by a factor of 2 to 4. Since crack growth in the near-threshold regime can dominate the fatigue life of an engineering component, these data suggest that selection of alloys with superior near-threshold FCP resistance may result in substantial improvements in fatigue life.

42

TABLE 7. RANKING OF MATERIALS BY STRESS INTENSITY RANGE TO OBTAIN A GIVEN FATIGUE CRACK GROWTH RATE UNDER CONSTANT AMPLITUDE LOADING

FCGR MATERIAL	ΔK, MPa $\sqrt{m}$ (ksi $\sqrt{in.}$) TO OBTAIN A GIVEN FCGR									
	RANK	10^{-10} m/CYCLE (4×10^{-9} in/CYCLE)	RANK	10^{-9} m/CYCLE (4×10^{-8} in/CYCLE)	RANK	10^{-8} m/CYCLE (4×10^{-7} in/CYCLE)	RANK	10^{-7} m/CYCLE (4×10^{-6} in/CYCLE)	RANK	10^{-6} m/CYCLE (4×10^{-5} in/CYCLE)
2024-T351	1	3.7 MPa $\sqrt{m}$ (3.4 ksi $\sqrt{in.}$)	1	3.8 MPa $\sqrt{m}$ (3.5 ksi $\sqrt{in.}$)	1	5.5 MPa $\sqrt{m}$ (5.0 ksi $\sqrt{in.}$)	4	7.6 MPa $\sqrt{m}$ (6.9 ksi $\sqrt{in.}$)	5	16.2 MPa $\sqrt{m}$ (14.7 ksi $\sqrt{in.}$)
2024-T851	3	2.7 MPa $\sqrt{m}$[a] (2.5 ksi $\sqrt{in.}$)	2	3.5 MPa $\sqrt{m}$ (3.2 ksi $\sqrt{in.}$)	4	4.8 MPa $\sqrt{m}$ (4.4 ksi $\sqrt{in.}$)	1	8.0 MPa $\sqrt{m}$ (7.3 ksi $\sqrt{in.}$)	6	15.0 MPa $\sqrt{m}$ (13.7 ksi $\sqrt{in.}$)
2124-T851	4	2.2 MPa $\sqrt{m}$[a] (2.0 ksi $\sqrt{in.}$)	4	2.8 MPa $\sqrt{m}$ (2.5 ksi $\sqrt{in.}$)	7	4.3 MPa $\sqrt{m}$ (3.9 ksi $\sqrt{in.}$)	1	8.0 MPa $\sqrt{m}$ (7.3 ksi $\sqrt{in.}$)	2	17.2 MPa $\sqrt{m}$ (15.7 ksi $\sqrt{in.}$)
7050-T73651	5	2.1 MPa $\sqrt{m}$[a] (1.9 ksi $\sqrt{in.}$)	5	2.7 MPa $\sqrt{m}$ (2.5 ksi $\sqrt{in.}$)	5	4.7 MPa $\sqrt{m}$ (4.3 ksi $\sqrt{in.}$)	6	7.2 MPa $\sqrt{m}$ (6.6 ksi $\sqrt{in.}$)	3	16.9 MPa $\sqrt{m}$ (15.4 ksi $\sqrt{in.}$)
7075-T7351	7	1.7 MPa $\sqrt{m}$[a] (1.6 ksi $\sqrt{in.}$)	7	2.5 MPa $\sqrt{m}$ (2.3 ksi $\sqrt{in.}$)	6	4.4 MPa $\sqrt{m}$ (4.0 ksi $\sqrt{in.}$)	4	7.6 MPa $\sqrt{m}$ (6.9 ksi $\sqrt{in.}$)	1	19.0 MPa $\sqrt{m}$ (17.3 ksi $\sqrt{in.}$)
7475-T651	2	3.3 MPa $\sqrt{m}$ (3.0 ksi $\sqrt{in.}$)	3	3.4 MPa $\sqrt{m}$ (3.1 ksi $\sqrt{in.}$)	2	5.4 MPa $\sqrt{m}$ (4.9 ksi $\sqrt{in.}$)	7	6.6 MPa $\sqrt{m}$ (6.0 ksi $\sqrt{in.}$)	7	12.1 MPa $\sqrt{m}$ (11.0 ksi $\sqrt{in.}$)
7475-T7351	6	2.0 MPa $\sqrt{m}$[a] (1.8 ksi $\sqrt{in.}$)	6	2.6 MPa $\sqrt{m}$ (2.4 ksi $\sqrt{in.}$)	3	4.9 MPa $\sqrt{m}$ (4.5 ksi $\sqrt{in.}$)	1	8.0 MPa $\sqrt{m}$ (7.3 ksi $\sqrt{in.}$)	4	16.6 MPa $\sqrt{m}$ (15.1 ksi $\sqrt{in.}$)

[a] EXTRAPOLATED

43

Closer inspection of Figures 21 and 22 reveals that the relative rankings of constant load amplitude FCP resistance for these seven materials vary with ΔK as further illustrated in Table 7. For example, 2024-T351 had the greatest fatigue resistance in the near-threshold region ($da/dN < 10^{-9}$ m/cycle), but not at higher growth rates (see Figure 22). Alloy 7475-T651 also exhibited excellent FCP resistance in the near-threshold regime, significantly better than the other three 7XXX materials. In contrast, growth rates for 7475-T651 in the intermediate ΔK region were a factor of two faster than those of any of the other materials. Crack growth rates for 7050-T73651, 7075-T7351, and 7475-T7351 were comparable at all ΔK levels, and are generally somewhat faster than FCGR for the 2XXX alloys. As previously noted, though, variations in FCP resistance among these alloys are small in the intermediate ΔK region (4 MPa$\sqrt{m}$ to 15 MPa$\sqrt{m}$).

3.5.1 Temper Effects

The microstructural variations controlled by temper and purity and their effects on constant amplitude FCP resistance can be examined individually in Figures 21 and 22. The temper comparisons are 2024-T351 vs. 2024-T851 and 7475-T651 vs. 7475-T7351. In the 2024 comparison, 2024-T351 exhibits crack growth rates less than or equal to 2024-T851 at almost all ΔK levels with the greatest difference occurring in the near-threshold region. A change in temper from T651 to T7351 in alloy 7475 results in a striking crossover in FCP resistance from low to intermediate ΔK levels. Peak-aged 7475-T651 is significantly more resistant to FCP in the near-threshold region, while overaging to the T7351 temper improves FCP resistance at intermediate ΔK levels.

The effect of temper on crack growth rates in 7XXX alloys has been studied previously, including the crossover in FCP resistance from low to intermediate ΔK. It is well established that overaging from a T651 temper to T7351 improves intermediate ΔK FCGR by reducing the acceleration of crack growth rates in the presence of an environment such as high humidity air. At high ΔK levels, lower growth rates in an overaged 7XXX alloy in comparison to the peak-aged temper condition are related to toughness[1-3, 15-19]. Recent studies[19, 29, 30] of FCP characteristics in the near-threshold region suggest that resistance to crack growth is particularly sensitive to microstructural details such as precipitate

44

morphology and distribution; in particular, peak-aged 7XXX alloys (commercially-produced as well as laboratory-fabricated) exhibit greater near-threshold FCP resistance than do the same alloys in overaged tempers.

3.5.2 Purity Effects

The effect of alloy purity (Fe, Si content) on FCP resistance can be examined by comparing data for 2024-T851 with 2124-T851 and 7075-T7351 with 7475-T7351. In both cases, the primary effect of increasing purity is to reduce crack growth rates at high ΔK levels, concurrent with increasing fracture toughness (Figure 22). This observation agrees with those reported in the literature [3, 15-18, 31]. At intermediate and near-threshold ΔK levels, however, there is no significant effect of purity on constant amplitude FCP resistance. The insensitivity of low and intermediate ΔK FCP behavior to alloy purity in 7XXX alloys is related to the absence of second phase particle fracture during crack growth at these stress intensities [2-3, 15-19].

3.6 SPECTRUM TESTING

The spectrum life results for each test are presented in Table 8. Overall the results were reproducible with the maximum difference between lives of the duplicate tests being 21 percent. Crack length versus simulated flight hour data (a vs H) are shown graphically in Appendix B, while the spectrum crack growth rate vs maximum peak stress intensity (da/dH vs K_{hmax}) are shown in Appendix C. For comparison, crack growth rate curves (da/dH vs K_{hmax}) for all seven materials and all three maximum peak stress levels are shown in Figures 23a and 23b. To allow comparison of resistance to spectrum crack growth between all seven materials for both spectra, the maximum peak stress intensities to obtain a given crack growth rate are presented in Figure 24 and Table 9 in a presentation similar to that for the constant amplitude data in Figure 22 and Table 7.

In general, the spectrum FCGR curves (Figures 23a and 23b) for each material and the two spectra have the same trends, i.e., the magnitudes are similar and the crossovers are in similar places. The fatigue crack growth rates (da/dH vs K_{hmax}) for the 169 MPa testing are essentially the same as for the 145 MPa testing in the range of K_{hmax} where they overlap for the same material and spectrum (see Appendix C). The one exception may be 7475-T651 for which the crack growth rates at 169 MPa appear to be faster than at 145 MPa — the

45

TABLE 8. SPECTRUM FATIGUE RESULTS

SIMULATED FLIGHT HOURS, H

MAXIMUM PEAK STRESS σ_{hmax}	103 MPa (15 ksi)		145 MPa (21 ksi)				169 MPa (24.5 ksi)			
SPECTRUM	TD	TC	TD		TC		TD		TC	
CRACK GROWTH REGIME, a_i-a_f	5.5-13 mm 0.22-0.51 in.	5.5-13 mm 0.22-0.51 in.	5.5-27 mm 0.22-1.06 in.	5.5 mm-F[a] 0.22 in.-F	5.5-27 mm 0.22-1.06 in.	5.5 mm-F 0.22 in.-F	18-23 mm 0.71-0.91 in.	18 mm-F 0.71 in.-F	18-23 mm 0.71-0.91 in.	18 mm-F 0.71 in.-F
MATERIAL										
2024-T351	31,579	28,717	22,970	23,610	16,335	16,682	1,730	2,451	796	1,092
	32,899	28,065	23,948	24,692	16,503	16,805	1,686	2,363	858	1,192
2024-T851	21,239	20,743	b	9,741	b	8,000	b	196	c	c
	22,086	20,292	b	9,592	b	8,193	b	184	c	c
2124-T851	19,804	18,037	12,902	12,356	d	9,502	597	851	d	1,085
	19,178	18,016	11,807	12,125	10,160	10,386	564	828	460	1,245
7050-T73651	21,798	22,832	15,746	16,450	14,179	14,498	1,245	2,260	1,040	1,638
	21,448	18,692	14,837	15,862	13,802	14,218	1,347	2,455	1,085	1,837
7075-T7351	20,179	19,158	14,374	14,775	11,323	11,508	905	1,300	534	740
	19,279	18,848	13,189	13,417	11,902	12,120	1,069	1,601	572	781
7475-T651	17,988	17,440	16,828	19,340	14,232	15,608	1,789	3,777	1,433	2,661
	17,384	18,835	18,825	20,981	15,372	16,349	1,625	3,197	1,577	2,608
7475-T7351	21,363	19,874	15,604	16,704	13,674	14,565	1,471	2,714	1,206	2,152
	21,799	19,064	14,799	15,954	13,777	14,715	1,502	2,852	1,245	2,256

a. F = FAILURE

b. SPECIMEN FRACTURED BEFORE REACHING FINAL CRACK LENGTH, a_f; THE HOURS TO FAILURE (F) WERE USED FOR GRAPHS AND COMPARISONS

c. SPECIMEN FRACTURED BEFORE REACHING INITIAL CRACK LENGTH, a_i, OF 18 MM, FOR THESE 169 MPa (24.5 ksi) TESTS, IN FATIGUE

d. SPECIMEN FRACTURED BEFORE REACHING FINAL CRACK LENGTH, a_f; THE RESULT FOR THE COMPANION TEST WAS USED FOR GRAPHS AND COMPARISONS
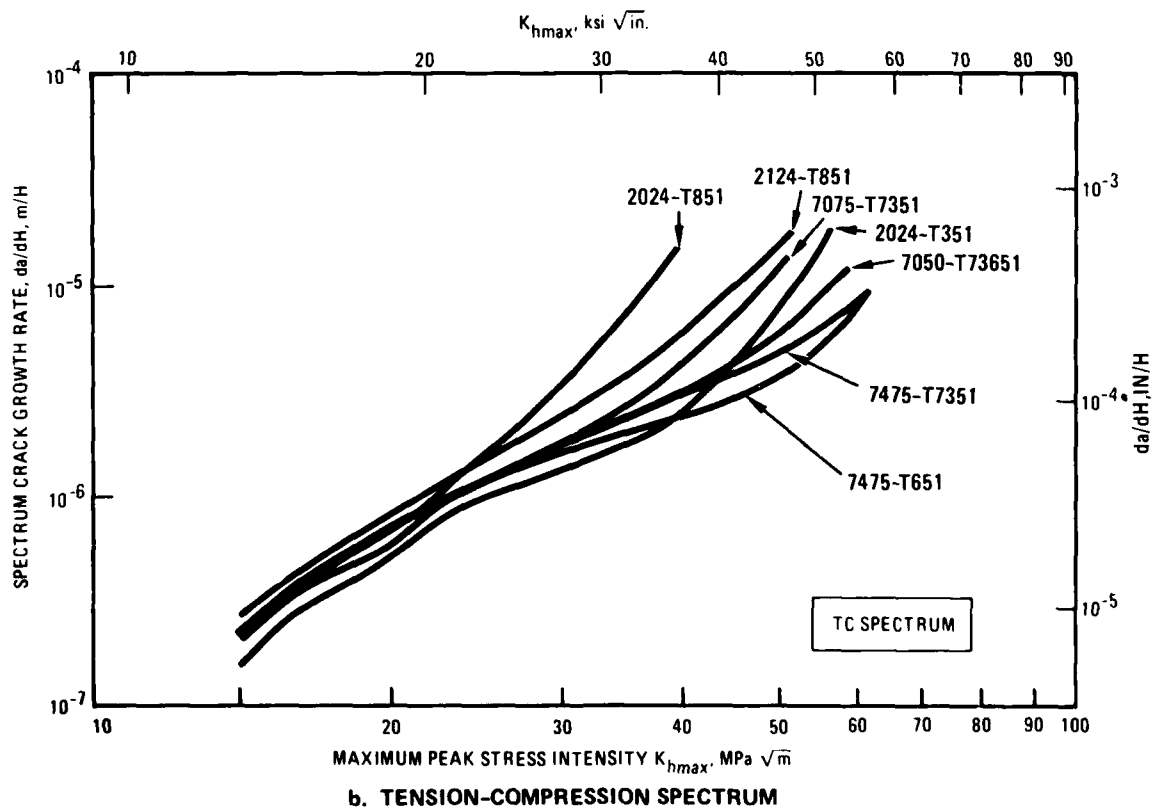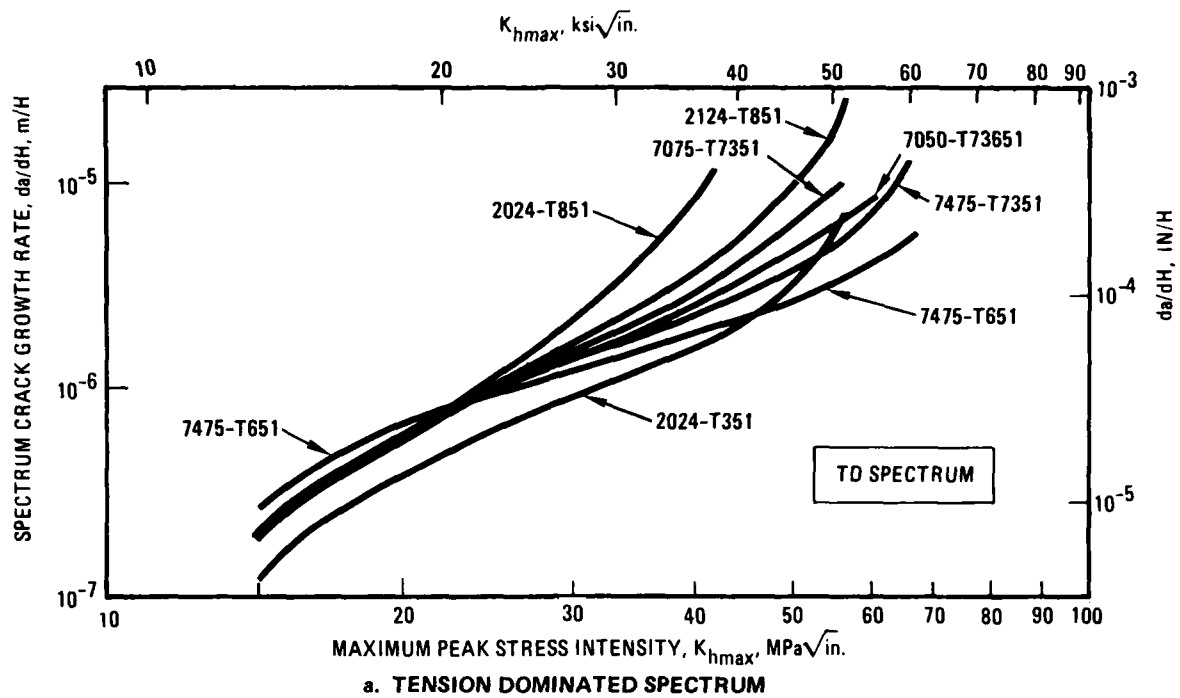
FIGURE 23. SPECTRUM FCGR CURVES

47
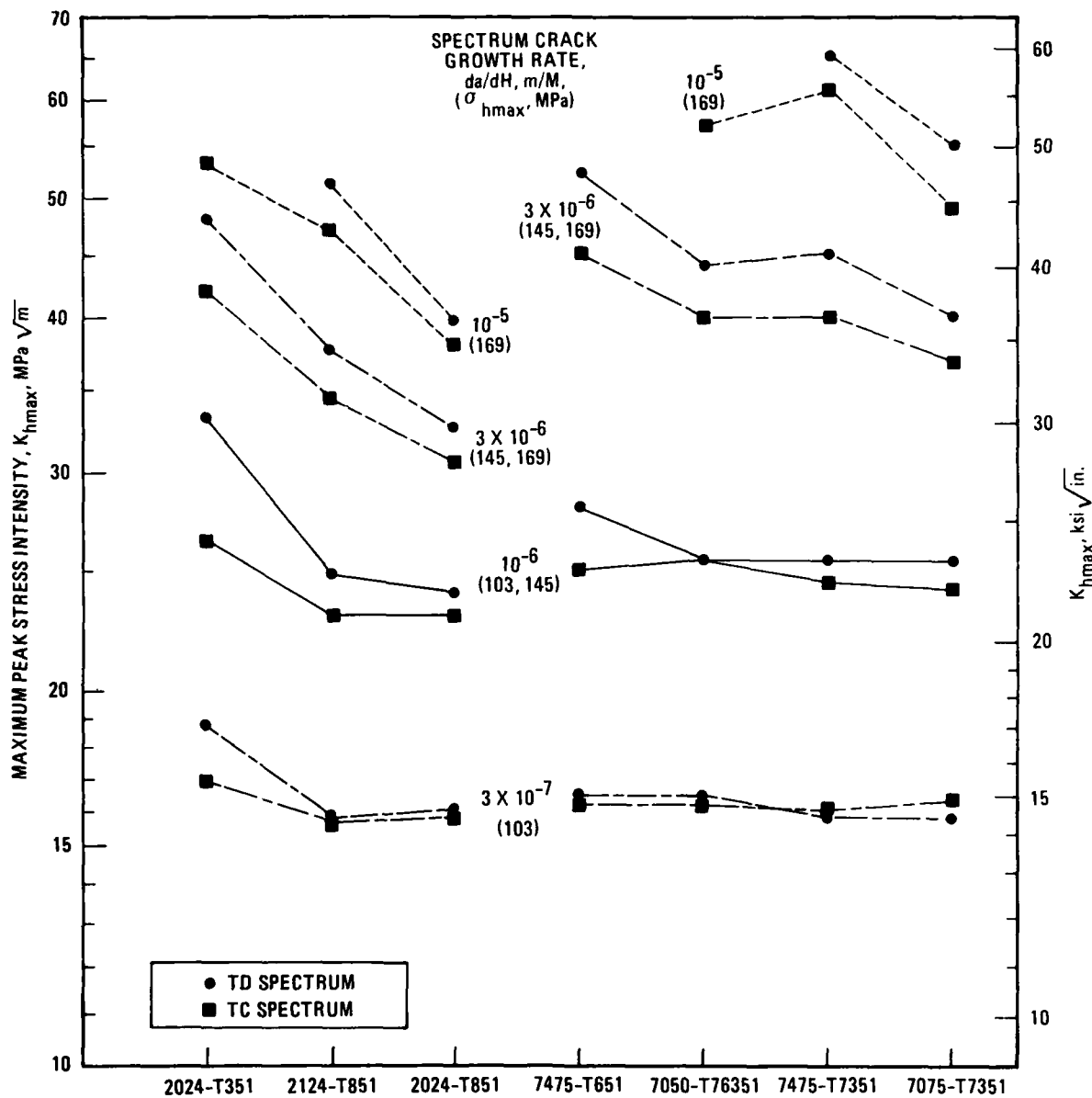
FIGURE 24. MAXIMUM PEAK STRESS INTENSITY NEEDED TO OBTAIN
A GIVEN SPECTRUM FATIGUE CRACK GROWTH RATE
(40–60% rh, L – T ORIENTATION)

interpretation is difficult because the data for 7475-T651 exhibit more scatter than any of the other materials (compare Figures C-11 and C-12 with C-1 through C-10, C-13 and C-14). However, the 103 MPa and 145 MPa results differed at the slower crack growth rates for some of the materials with the rates for 145 MPa slower for the same K_{hmax} up to about 5×10^{-7} m/H where they became the

TABLE 9. RANKING OF MATERIALS IN SPECTRUM FATIGUE BY MAXIMUM PEAK STRESS INTENSITY TO OBTAIN A GIVEN FATIGUE CRACK GROWTH RATE

K_{hmax}, MPa $\sqrt{m}$ (ksi $\sqrt{in.}$) TO OBTAIN A GIVEN SPECTRUM FCGR

FCGR SPECTRUM MATERIAL	3×10^{-7} m/H[a] (1.2×10^{-5} in./H)			10^{-6} m/H (4×10^{-5} in./H)[b]			3×10^{-6} m/H (1.2×10^{-4} in./H)[c]			10^{-5} m/H (4×10^{-4} in./H)[d]		
	TD	RANK[e]	TC	TD	RANK[e]	TC	TD	RANK[e]	TC	TD	RANK[e]	TC
2024-T351	18.8 (17.1)	1	17.0 (15.5)	33.0 (30.0)	1	26.5 (24.1)	48 (44)	2	42 (38)	-- --	4	53 (48)
2024-T851	16.0 (14.6)	5	15.9 (14.5)	24.0 (21.8)	7	23.0 (20.9)	32 (29)	7	31 (28)	41 (37)	7	38 (35)
2124-T851	15.8 (14.4)	7	15.7 (14.3)	24.8 (22.6)	6	23.0 (20.9)	38 (35)	6	34 (31)	51 (46)	6	47 (43)
7050-T73651	16.2 (14.7)	2	16.5 (15.0)	25.5 (23.2)	3	25.5 (23.2)	44 (40)	4	40 (36)	-- --	3	57 (52)
7075-T7351	16.4 (14.9)	4	15.9 (14.5)	25.5 (23.2)	5	24.2 (22.0)	40 (36)	5	37 (34)	55 (50)	5	49 (45)
7475-T651	16.2 (14.7)	2	16.5 (15.0)	28.0 (25.5)	2	24.7 (22.5)	52 (47)	1	45 (41)	-- --	1[f]	-- --
7475-T7351	16.0 (14.7)	5	15.9 (14.5)	25.5 (23.2)	4	24.5 (22.3)	45 (41)	3	40 (36)	65 (59)	2	61 (56)

a σ_{hmax} = 103 MPa (15 ksi)

b σ_{hmax} = 103 MPa (15ksi) and 145 MPa (21 ksi)

c σ_{hmax} = 145 MPa (21 ksi)

d σ_{hmax} = 145 MPa (21 ksi) and 169 MPa (24.5 ksi)

e BASED ON AVERAGE TD AND TC SPECTRUM

f BASED ON EXTRAPOLATION

same (see, for example, Figure C-1 in Appendix C). A review of the test procedure showed no apparent reason for this anomaly. Nevertheless, several tests were performed at 145 MPa using no precracking or a modified precracking procedure, both of which allowed obtaining data at lower values of K_{hmax}. These FCGR data duplicated the results at 103 MPa, indicating that the anomaly was due to residual effects of the precracking procedure; therefore, the slower FCGR for 145 MPa are not shown in Figure 23, Table 9, nor in the other data presentations in this report. Further testing and analysis will be performed to determine the reason for the anomaly and to correct the test procedure for future work.

3.6.1 Ranking of the Materials

The alloys are ranked by their spectrum fatigue lives for each spectrum (average of the two duplicate tests) in Table 10 as the initial step in determining critical material and spectrum parameters. These results are shown graphically in Figure 25. Several observations for the 145 MPa test results ("a" from 5.5 to 27 mm) can be made:

1. The ranking of the seven alloys is the same for the two spectra.

2. For each material the TD spectrum consistently resulted in longer lives.

3. The differences in life for the same material between the two spectra was small — not more than an 18 percent difference between the lives for the two spectra for the same material, except for 2024-T351 which had a 35 percent difference.

4. Among all the 7XXX materials tested, there was only a 25 percent difference in life between the alloy with the shortest life (7075-T7351) and the alloy with the longest life (7475-T651).

5. There was a much larger difference in lives among the 2XXX materials with an 84 percent difference for the TD spectrum and a 68 percent difference for the TC spectrum between the material with the shortest life (2024-T851) and the material with the longest life (2024-T351).

A comparison of spectrum lives from "a" of 5.5 mm to failure at 145 MPa gives the same ranking as for from "a" of 5.5 to 27 mm except for the exchange of 7050-T73651 and 7475-T7351 (Table 10b); the similarity is not surprising since little of the life is spent in growing the crack from 27 mm to failure (high stress intensities).

TABLE 10. RANKING OF MATERIALS UNDER SPECTRUM LOADING

AVERAGES ROUNDED TO NEAREST HUNDRED HOURS

a. σ_{hmax} = 103 MPa FROM a = 5.5 MM TO 13 MM

TD SPECTRUM		TC SPECTRUM	
MATERIAL	**HOURS**	**MATERIAL**	**HOURS**
2024–T351	32,200	2024–T351	28,400
2024–T851	21,700	7050–T73651	20,700
7050–T73651	21,600	2024–T851	20,500
7475–T7351	21,600	7475–T7351	19,500
7075–T7351	19,700	7075–T7351	19,000
2124–T851	19,500	7475–T651	18,100
7475–T651	17,700	2124–851	18,000

b. σ_{hmax} = 145 MPa FROM a = 5.5 MM TO 27 MM OR FAILURE

TD SPECTRUM				TC SPECTRUM			
MATERIAL	**HOURS TO 27 MM**	**MATERIAL**	**HOURS TO FAILURE**	**MATERIAL**	**HOURS TO 27 MM**	**MATERIAL**	**HOURS TO FAILURE**
2024–T351	23,500	2024–T351	24,100	2024–T351	16,400	2024–T351	16,700
7475–T651	17,800	7475–T651	20,100	7475–T651	14,800	7475–T651	16,000
7050–T73651	15,300	7475–T7351	16,300	7050–T73651	14,000	7475–T7351	14,600
7475–T7351	15,200	7050–T73651	14,700	7475–T7351	13,700	7050–T73651	14,400
7075–T7351	13,800	7075–T7351	14,100	7075–T7351	11,600	7075–T7351	11,800
2124–T851	12,000	2124–T851	12,200	2124–T851	10,200[b]	2124–T851	9,900
2024–T851	a	2024–T851	9,700	2024–T851	a	2024–T851	8,100

c. σ_{hmax} = 169 MPa FROM a = 18 MM TO 23 MM OR FAILURE

TD SPECTRUM				TC SPECTRUM			
MATERIAL	**HOURS TO 23 MM**	**MATERIAL**	**HOURS TO FAILURE**	**MATERIAL**	**HOURS TO 23 MM**	**MATERIAL**	**HOURS TO FAILURE**
2024–T351	1,700	7475–T651	3,500	7475–T651	1,500	7475–T651	2,600
7475–T651	1,700	7475–T7351	2,800	7475–T7351	1,200	7475–T7351	2,200
7475–T7351	1,500	2024–T351	2,400	7050–T73651	1,100	7050–T73651	1,700
7050–T73651	1,300	7050–T73651	2,400	2024–T351	800	2124–T851	1,200
7075–T7351	1,000	7075–T7351	1,400	7075–T7351	600	2024–T351	1,100
2124–T851	600	2124–T851	800	2124–T851	500[b]	7075–T7351	800
2024–T851	a	2024–T851	190	2024–T851	c	2024–T851	c

a. FRACTURED BEFORE REACHING FINAL CRACK LENGTH IN FATIGUE, THE HOURS TO FAILURE WERE USED FOR GRAPHS AND COMPARISONS

b. SINGLE VALUE, OTHER SPECIMEN PER FOOTNOTE a

c. SPECIMEN FRACTURED BEFORE REACHING INITIAL CRACK LENGTH, a_i
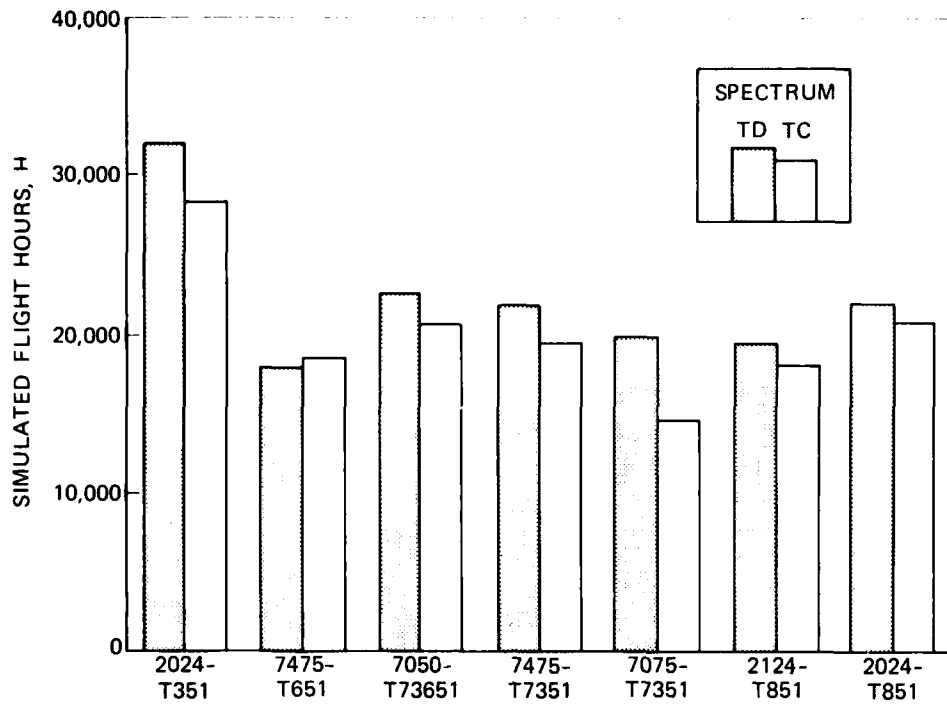
a. SPECTRUM LIFE AT 103 MPa, "a" FROM 5.5 TO 13 MM — THE MATERIALS ARE
LISTED IN DESCENDING ORDER FOR LIFE AT 145 MPa.
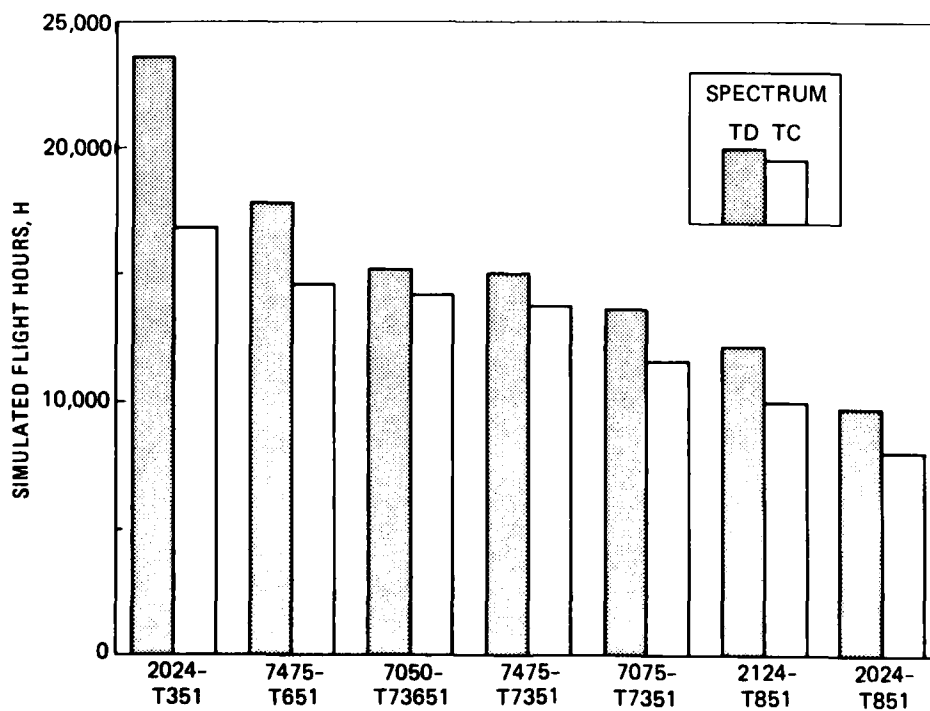
b. SPECTRUM RANKING AT 145 MPa, "a" FROM 5.5 TO 27 MM

FIGURE 25. SPECTRUM FATIGUE LIVES
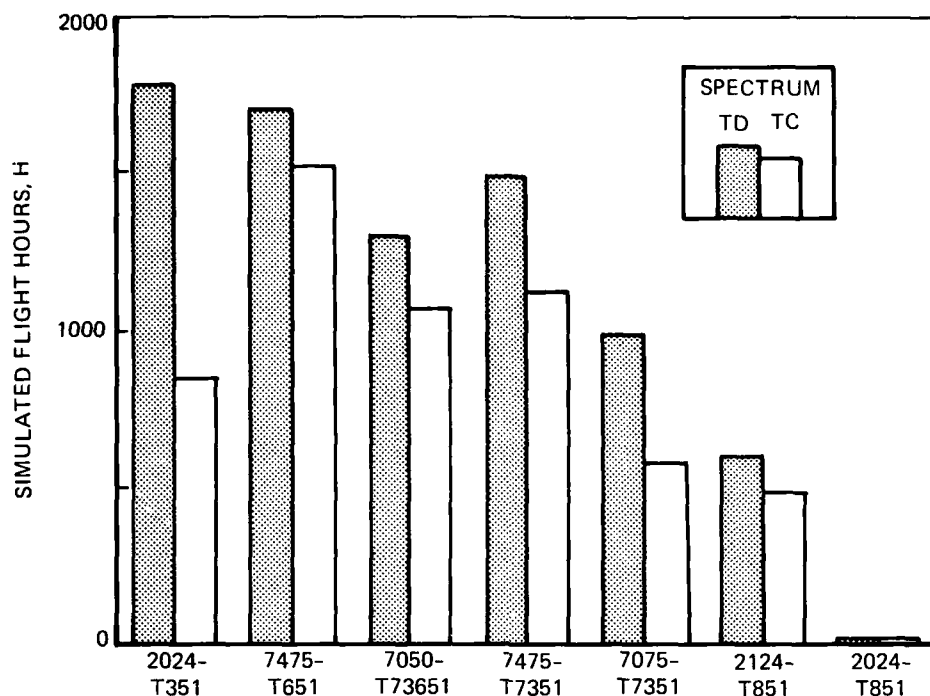
c. SPECTRUM LIFE AT 169 MPa, "a" FROM 18 TO 23 MM — THE MATERIALS ARE LISTED IN DESCENDING ORDER FOR LIFE AT 145 MPa.

FIGURE 25. SPECTRUM FATIGUE LIVES (Continued)

Due to the test methodology, the lives of the specimens for the testing at the other two maximum peak stress levels (103 and 169 MPa) represent a much smaller range of crack growth (or range of maximum peak stress intensity). Specifically, for the 103 MPa testing, the range of maximum peak stress inten-sity is only from 13.7 to 21.8 MPa$\sqrt{m}$ (see Figures 8 and 9). Several observations from the 103 MPa test results ("a" from 5.5 to 13 mm) can be made (Figure 25a):

1. Except for 2024-T351, each alloy had about the same spectrum fatigue life. The 2024-T351 alloy had a significantly longer spectrum fatigue life than the other alloys.

2. For each alloy, the TD spectrum resulted in a nearly equal or some-what longer spectrum fatigue life than the same alloy tested with the TC spectrum.

3. Except for 2024-T351, the rankings do not correlate with the rankings for testing at 145 MPa.

53

4. The first two observations reflect similarity of the crack growth rates for all alloys except 2024-T351, which had significantly slower crack growth rates.

For the 169 MPa testing the range of maximum peak stress intensity is from 43.6 to 52.2 MPa$\sqrt{m}$. In comparison to the testing at the other two maximum peak stresses, the lives are an order of magnitude shorter. The lives represent less than one aircraft lifetime and, therefore, are of lesser value for airframe applications. Nevertheless, several observations from these results ("a" from 18 to 23 mm) can be made (Figure 25c and Table 10c):

1. Overall, the rankings are similar to the results at 145 MPa with the following exceptions:

    a. Alloy 2024-T351 still had the longest life for the TD spectrum; however, for the TC spectrum it had a lower life than 7050-T73651, 7475-T651, and 7475-T7351.

    b. Alloys 7050-T73651 and 7475-T7351 have switched rankings (compared to the results at 145 MPa) for both spectra, but the differences in life are relatively small.

2. The rankings change if the comparisons are made to failure, Table 10c. However, the rankings within the 2XXX group and the 7XXX group remained the same.

3.6.2 Effects of Yield Strength and Temper

The relationship between yield strength and spectrum fatigue lives is shown in Figure 26. Looking first at the 145 MPa results (Figure 26b) for all the materials, no overall relationship can be seen. However, looking at the 2XXX and 7XXX alloys as two separate groups the following trends are seen:

1. For the 2XXX alloys, there is an inverse relationship between life and yield strength.

2. However, for the 7XXX alloys, there is a weak direct relationship.

3. For the 2XXX alloys, the inverse relationship between life and yield strength also holds over the shorter ranges of crack growth for tests at the other two maximum peak stresses (Figures 26a and 26c), however, for the 7XXX alloys, no clear relationship exists; while at 169 MPa, the weak direct relationship still exists.

54
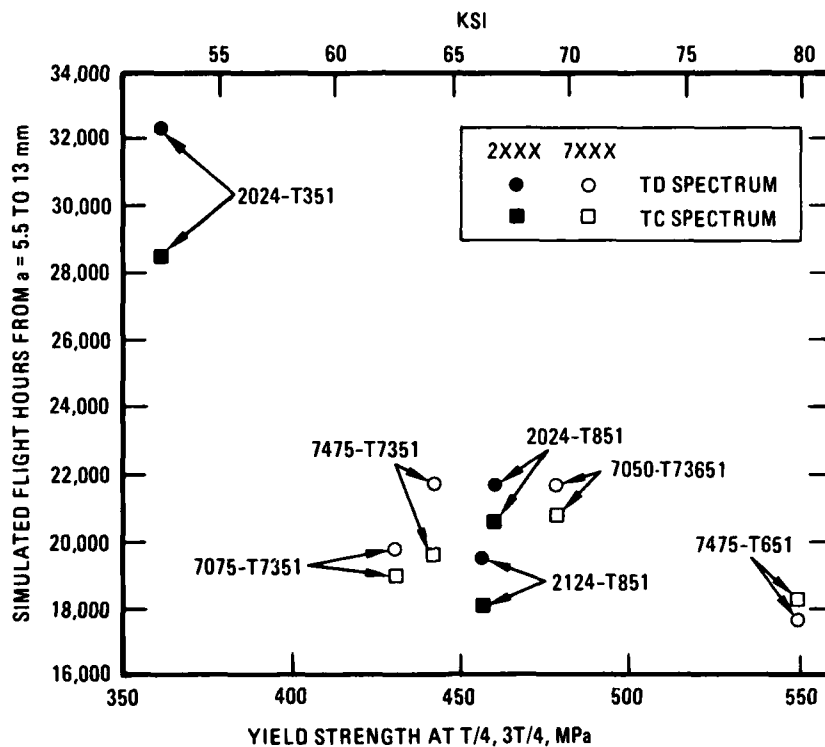
a. σ_{hmax} = 103 MPa (15 ksi)
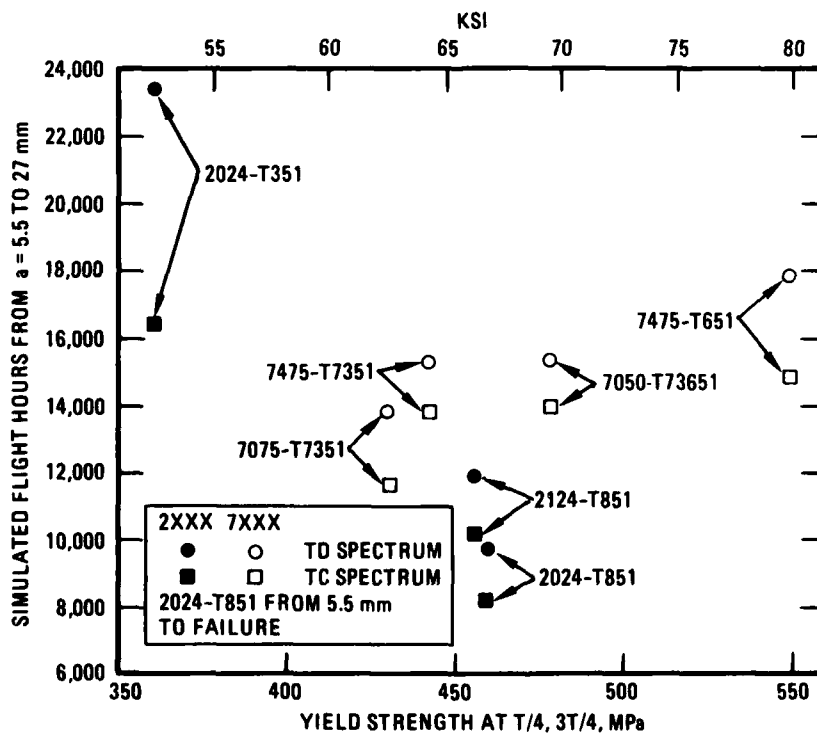
b. σ_{hmax} = 145 MPa (21 ksi)

FIGURE 26. SPECTRUM LIFE VS YIELD STRENGTH

55

4. In general, these results do not fit models such as Willenborg[20], which predict increased life with lower yield strength.
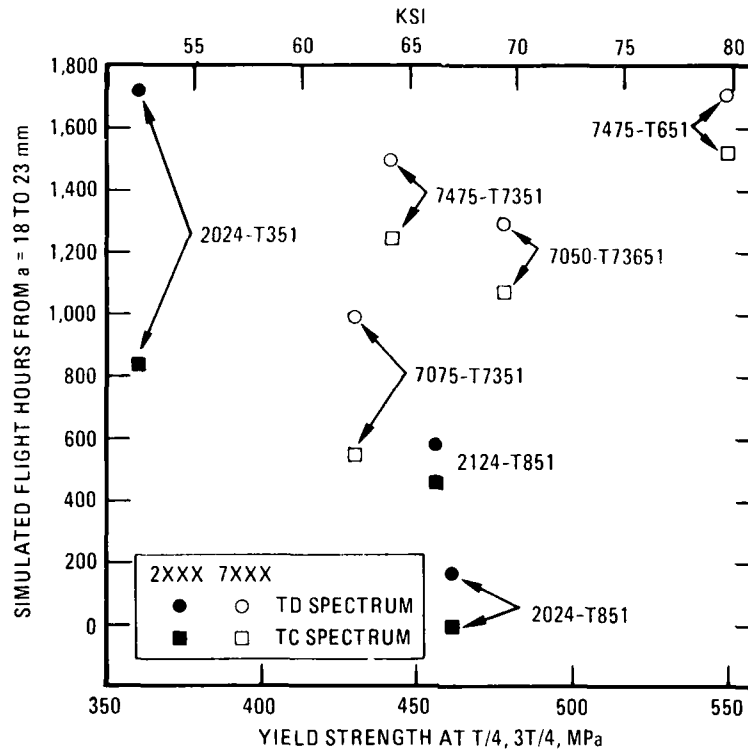
c. σ_{hmax} = 169 MPa (24.5 ksi)

FIGURE 26. SPECTRUM LIFE VS YIELD STRENGTH (Continued)

The effect of different tempers was investigated by comparing the spectrum fatigue behavior of 2024-T351 with 2024-T851 and 7475-T651 with 7475-T7351. Microstructurally, the difference in temper manifests itself in precipitate struc-ture, size, and distribution. As far as mechanical properties are concerned, temper manifests itself in differences in yield strength and toughness, which is shown graphically in Figure 27. A clear inverse relationship between yield strength and spectrum life exists at all three maximum peak stress levels for the 2024 alloy, with the lower yield strength 2024-T351 having twice the life as that of 2024-T851. In terms of spectrum crack growth rates, the lower strength T351 conditions (YS = 360 MPa, 52 ksi) has slower crack growth rates than the higher strength T851 condition (YS = 460 MPa, 67 ksi) at all maximum peak stress intensities (Figure 28). This is consistent with the constant amplitude FCGR results where the lower strength T351 exhibits slower FCGR than the higher strength T851 at almost all stress intensities.

56
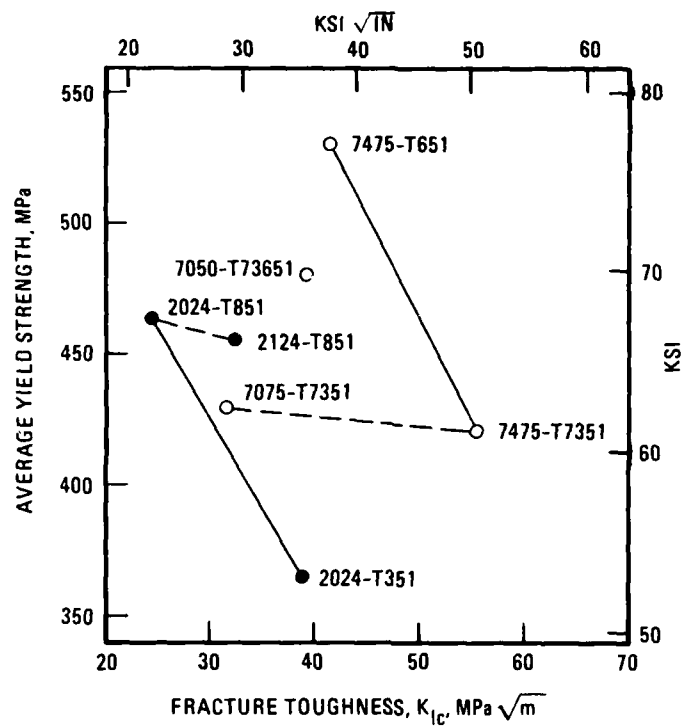
FIGURE 27. RELATIONSHIP BETWEEN YIELD STRENGTH AND FRACTURE TOUGHNESS
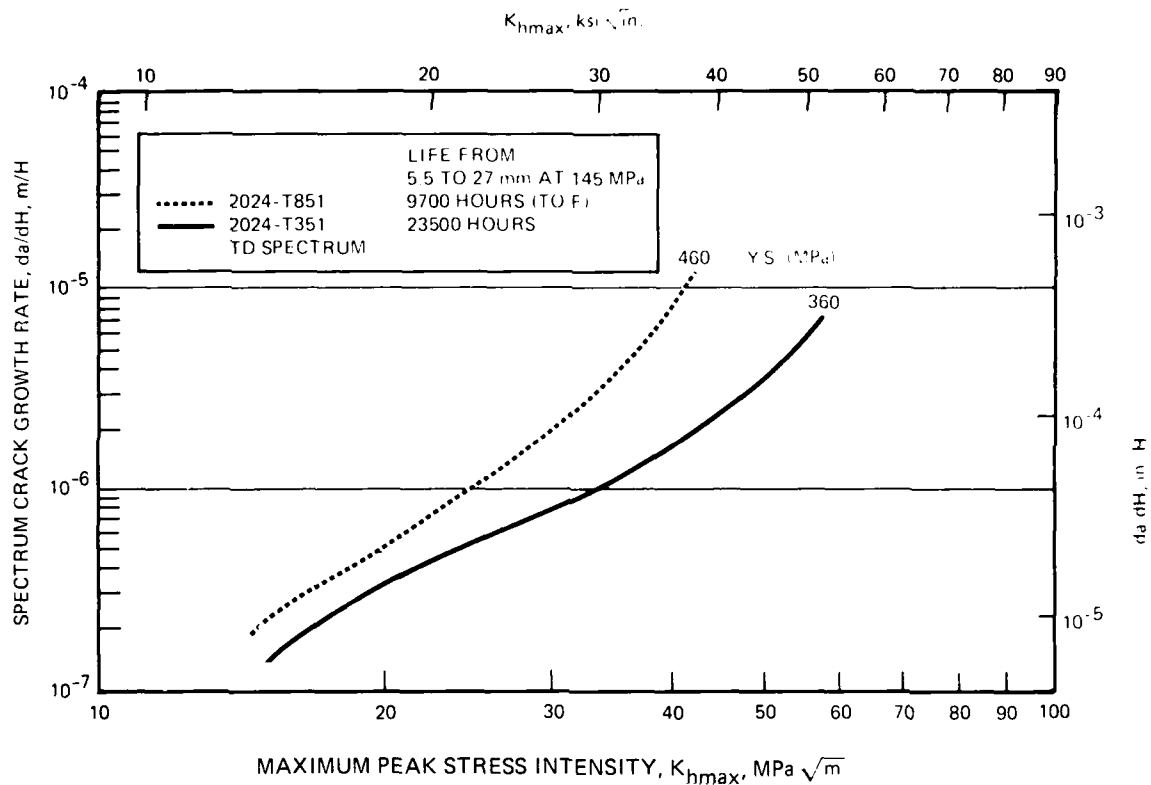
**FIGURE 28. EFFECT OF PRECIPITATE STRUCTURE (TEMPER)
ON SPECTRUM FCGR FOR 2024**

However, for the 7475 alloy, the difference in spectrum crack growth rates
between the two tempers is smaller and varies depending upon the maximum peak
stress intensity (Figure 29). For the tests at 145 MPa (longest range of crack
growth), the higher yield strength T651 temper had a 12 percent longer life
(average of both spectra) than the lower yield strength T7351 temper. Similarly,
for the testing at 169 MPa, the T651 temper had a 15 percent longer life than that
for the T7351 temper. In contrast, over the shorter range of crack growth for
testing at 103 MPa, the T651 temper had a 15 percent shorter life than the T7351
temper. The small differences in spectrum FCP behavior for these two tempers
are also apparent in the FCGR curves (Figure 29), which indicate a crossover in
ranking at about $K_{hmax} = 21$ MPa $\sqrt{m}$.
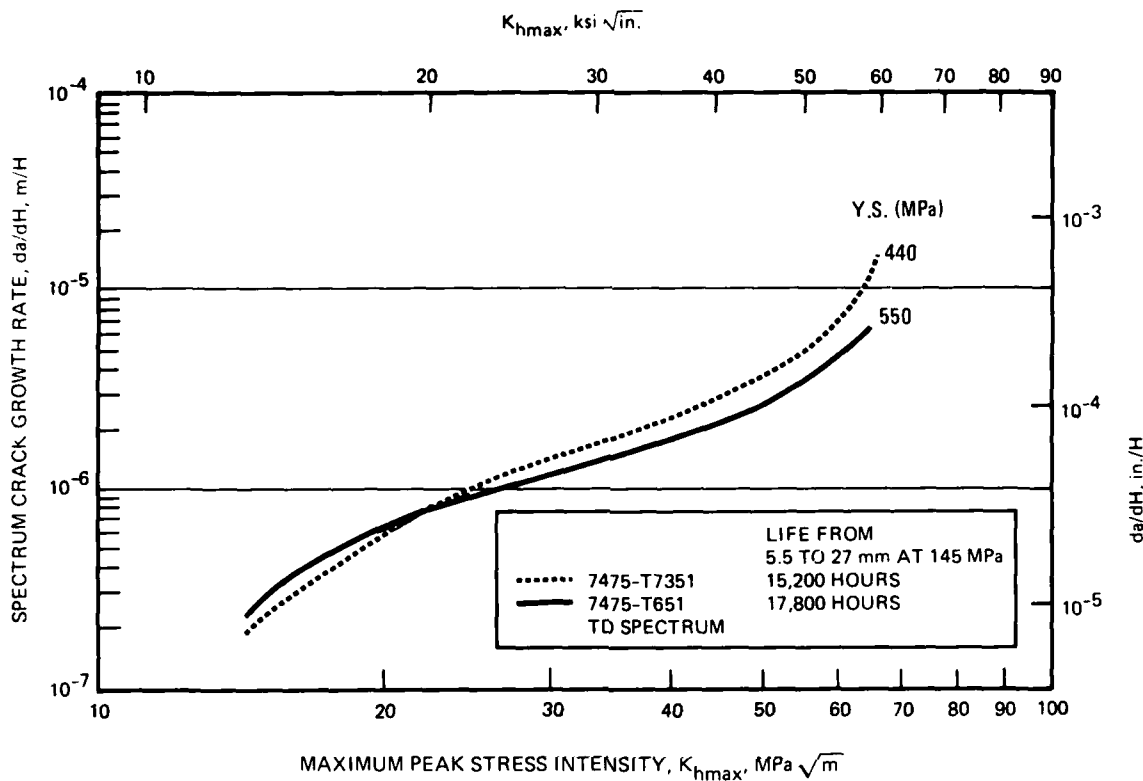
FIGURE 29. EFFECT OF PRECIPITATE STRUCTURE (TEMPER)
ON SPECTRUM FCGR FOR 7475

3.6.3 Effects of Fracture Toughness and Purity

The relationship between fracture toughness and spectrum fatigue life is
shown in Figure 30. As seen in Figure 30b, spectrum fatigue life generally in-
creases with increasing fracture toughness for the tests conducted at the maxi-
mum peak stress of 145 MPa (21 ksi). As a group the 2XXX alloys show a
stronger correlation between spectrum life and fracture toughness; and the
7XXX alloys show a positive correlation except for the 7475-T7351 alloy. Even
though 7475-T7351 has the highest fracture toughness of all the materials in this
program, it had a spectrum life less than or equal to 7050-T73651 and 7475-T651.

KSI $\sqrt{IN}$

SIMULATED FLIGHT HOURS FROM a = 5.5 TO 13 mm

2XXX	7XXX	
●	○	TD SPECTRUM
■	□	TC SPECTRUM

2024-T351

2024-T851

7050-T73651

7475-T7351

7075-T7351

2124-T851

7475-T7651

FRACTURE TOUGHNESS, K_{Ic}, MPa $\sqrt{m}$

a. σ_{hmax} = 103 MPa (15 ksi)

KSI $\sqrt{IN}$

SIMULATED FLIGHT HOURS FROM a = 5.5 TO 27 mm

2024-T351

7475-T651

7050-T73651

7475-T7351

7075-T7351

2124-T851

2024-T851

2XXX	7XXX	
●	○	TD SPECTRUM
■	□	TC SPECTRUM
2024-T851 FROM 5.5 mm TO FAILURE		
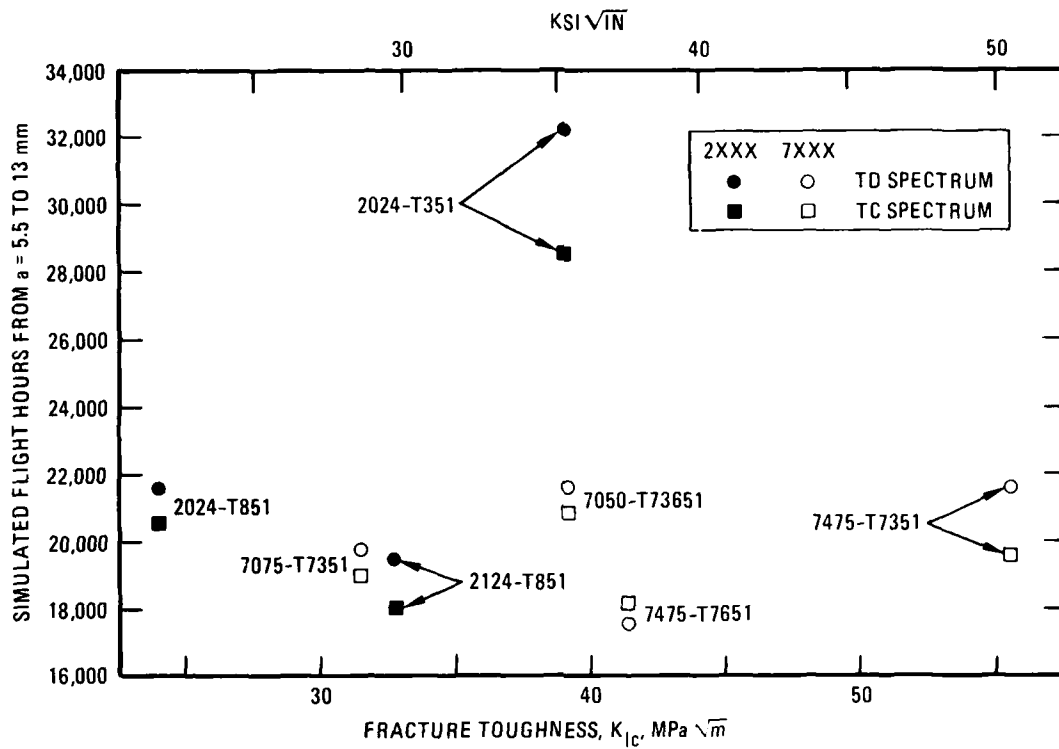
FRACTURE TOUGHNESS, K_{Ic}, MPa $\sqrt{m}$
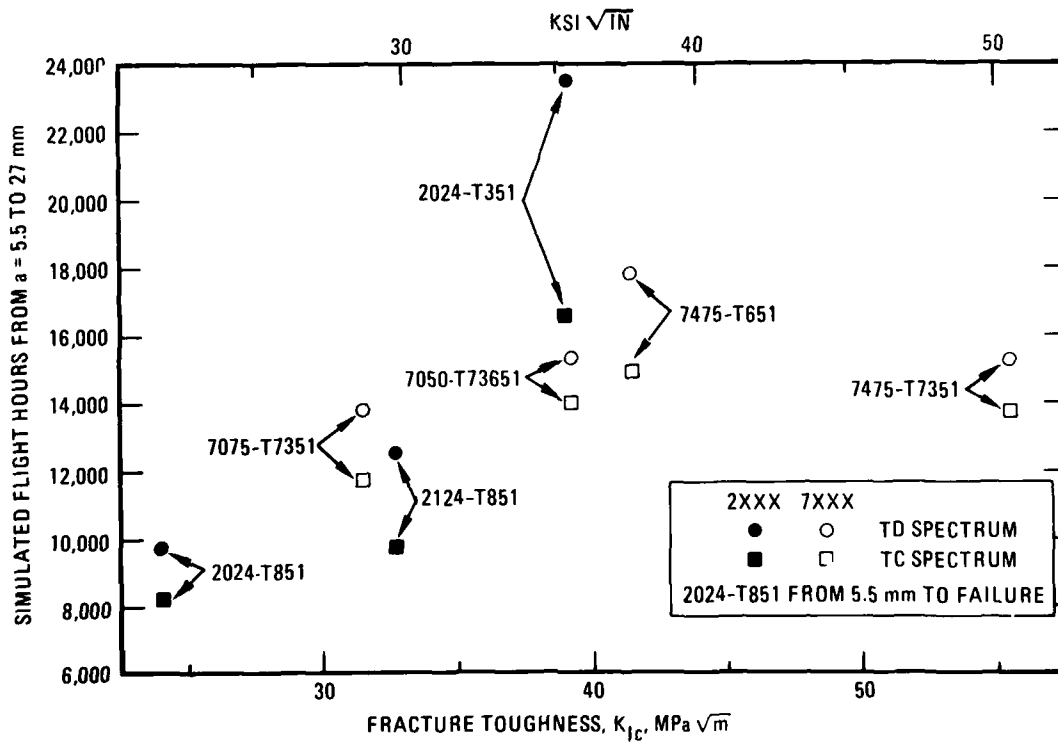
b. σ_{hmax} = 145 MPa (21 ksi)

FIGURE 30. SPECTRUM LIFE VS FRACTURE TOUGHNESS
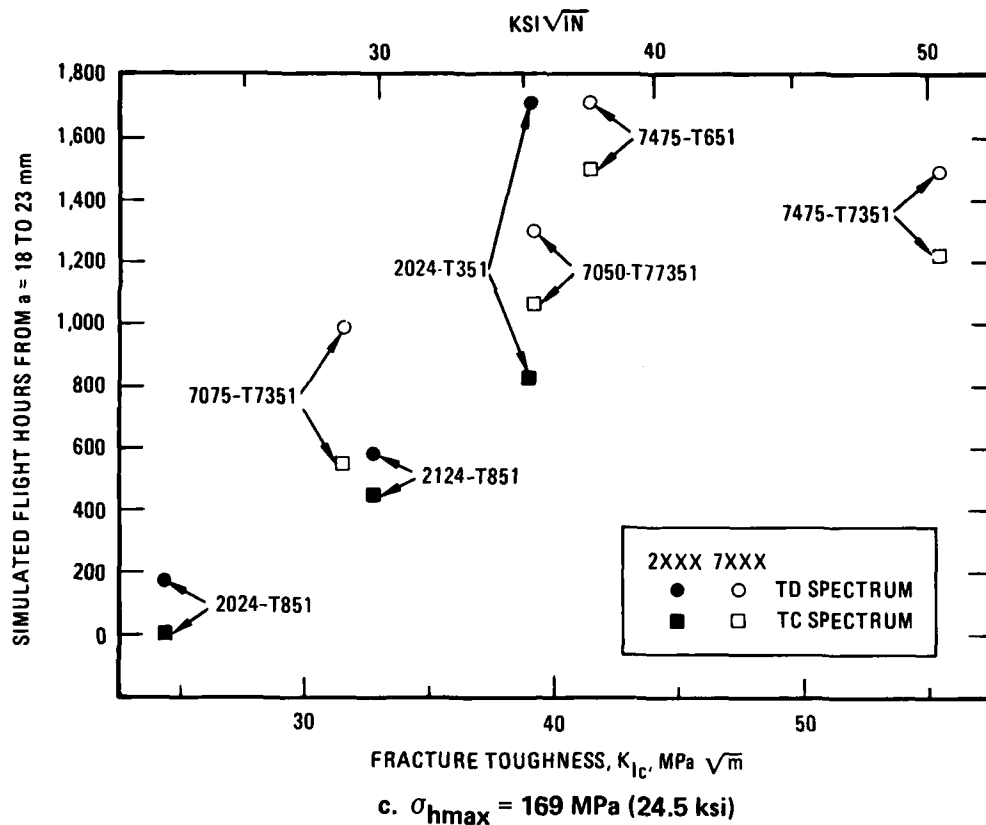
FIGURE 30. SPECTRUM LIFE VS FRACTURE TOUGHNESS (Continued)

K_{hmax} exceeds K_{Ic} during the entire test at 169 MPa for every alloy except 7475-T7351 material. Recognizing that plane strain fracture toughness, K_{Ic}, does not necessarily correlate with the plane stress situation of this testing; there is, nevertheless, a positive correlation between K_{Ic} and spectrum life (Figure 30c). The 7475-T7351 material with its superior fracture toughness (K_{Ic} = 55 MPa $\sqrt{m}$) does not have a longer life than the 7475-T651 (K_{Ic} = 41 MPa $\sqrt{m}$). Even when compared on the basis of from 18 mm to failure (instead of from 18 to 23 mm) the lower toughness 7475-T651 had a longer life than the higher toughness 7475-T7351 (Table 10c). For the 103 MPa tests (with low maximum peak stress intensity relative to the fracture toughness) no correlation exists between fracture toughness and spectrum fatigue life (Figure 30a).

Direct comparisons of the effect of alloy purity on spectrum behavior can be made by comparing 2024-T851 with 2124-T851 and 7075-T7351 with 7475-T7351. The silicon and iron contents of 2124-T851 and 7475-T351 alloys are significantly lower than those of their standard counterparts (Table 4). The fracture toughness values of 2124-T851 and 7475-T7351, as shown in Table 6, are substantially higher than their lower purity counterparts, while yield strengths (Table 5) remain about the same (see also Figure 27). Both higher purity, higher toughness materials had longer spectrum fatigue lives than their counterparts for tests at 145 MPa (28 percent for 2X24-T851 and 10 percent for 7X75-T7351, Figure 30b). Spectrum FGGR curves for these two pairs are shown in Figures 31 and 32. In both cases, the FCGR's are similar at low K_{hmax} values, but become slower for the purer materials at higher values of K_{hmax}.

3.6.4 Effects of Load History

The effect of load history will be considered in more detail in the next phase where the baseline data will be utilized in various life prediction models and correlated with the spectrum FCP results obtained. Some observations that can be made at present follow:

1. For the same material, the crack growth rates are similar for the two spectra at the lower stress intensities (Figure 23 or Figure 24). However, at higher stress intensities the rates for the two spectra generally diverge, with the rates for the TC spectrum faster than those for the TD spectrum. This is shown graphically in Figure 33 as a ratio of the FCGR's for the two spectra at various stress intensities.

2. Since a relatively small percentage of total life is spent at the higher stress intensities where the maximum difference in the crack growth rates was observed, spectrum fatigue lives are similar for the same materials for the two spectra when tested over a long range of crack growth (i.e., the 145 MPa testing).

3. When the lives for the same material are compared only over the higher stress intensities (i.e., the 169 MPa) testing, the difference in lives between the two spectra are somewhat greater.

62
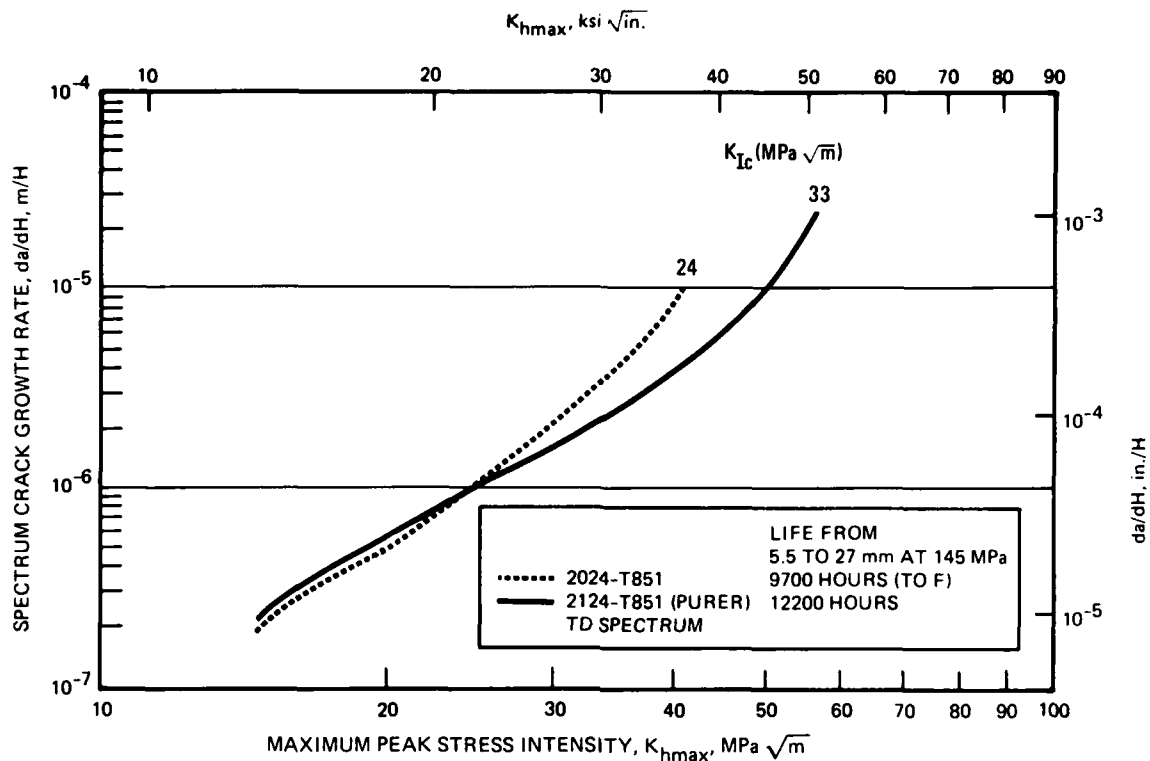
FIGURE 31. EFFECT OF PURITY ON SPECTRUM FCGR FOR 2X24-T851 MATERIALS
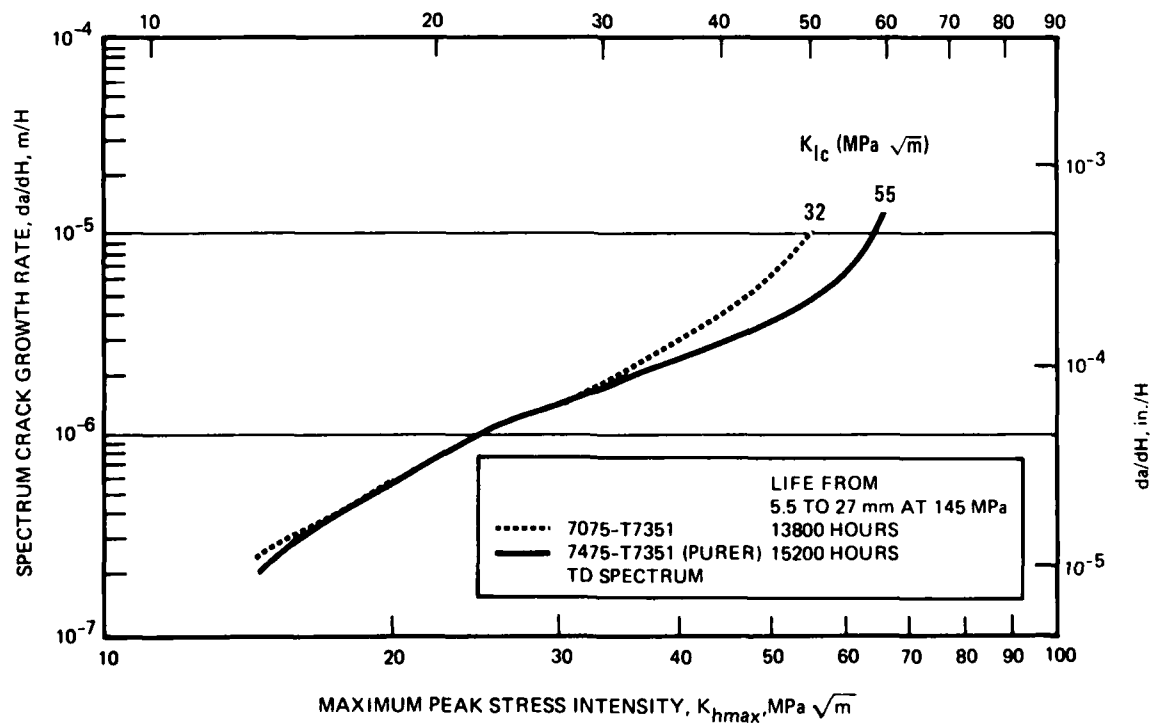
FIGURE 32. EFFECT OF PURITY ON SPECTRUM FCGR FOR 7X75-T7351 MATERIALS

63
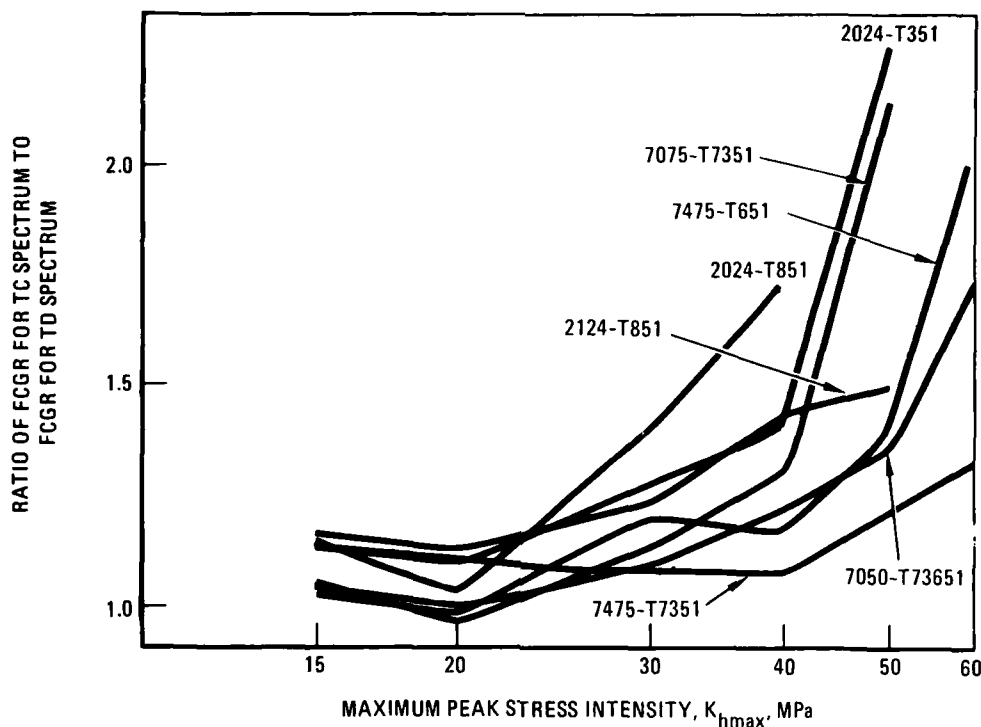
FIGURE 33. RATIO OF THE FCGR'S FOR THE TWO SPECTRA

3.7 FRACTOGRAPHY

3.7.1 General Observations

On a macroscopic scale, the fracture appearances of all seven alloys tested at K_{hmax} of 145 MPa under both spectra are similar. The FCP regions are flat (i.e., perpendicular to the tensile stress axis) at shorter crack lengths, while a gradual transition to slant fracture occurs with increasing crack length. For three of these alloys (2024-T351, 7050-T73651, and 7475-T651) tested under either spectrum, the slant fracture FCP regions contain dark fretting deposits. Such deposits indicate substantial rubbing of fracture surface during crack growth, which were not observed in the other four alloys. Perhaps coincidentally, the three alloys containing fretting deposits are also those which rank highest in spectrum FCP resistance (Figure 25b).

Microscopically, the fracture surface appearance of each alloy at a given crack length (i.e., the same value of K_{hmax}) does not vary noticeably between the two spectra. For example, Figures 34 and 35 compare the fracture topography of 2024-T351 at two crack lengths for the TD and TC spectra, respectively.

64
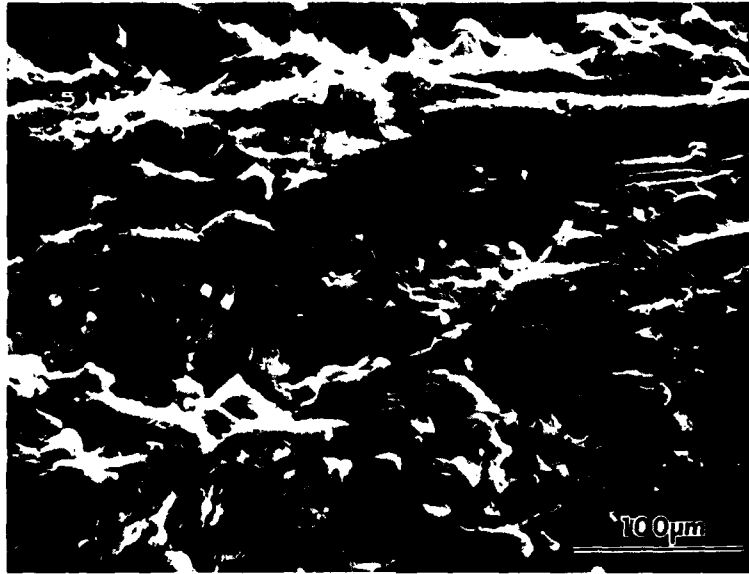
a. a = 6.4MM (0.25 IN.)   250X

CRACK GROWTH DIRECTION

b. a = 6.4MM (0.25 IN.)   1500X

FIGURE 34. FRACTURE SURFACE OF 2024-T351 TESTED USING TD SPECTRUM

c. a 19MM (0.75 IN.)

CRACK GROWTH DIRECTION

d. a 19MM (0.75 IN.)
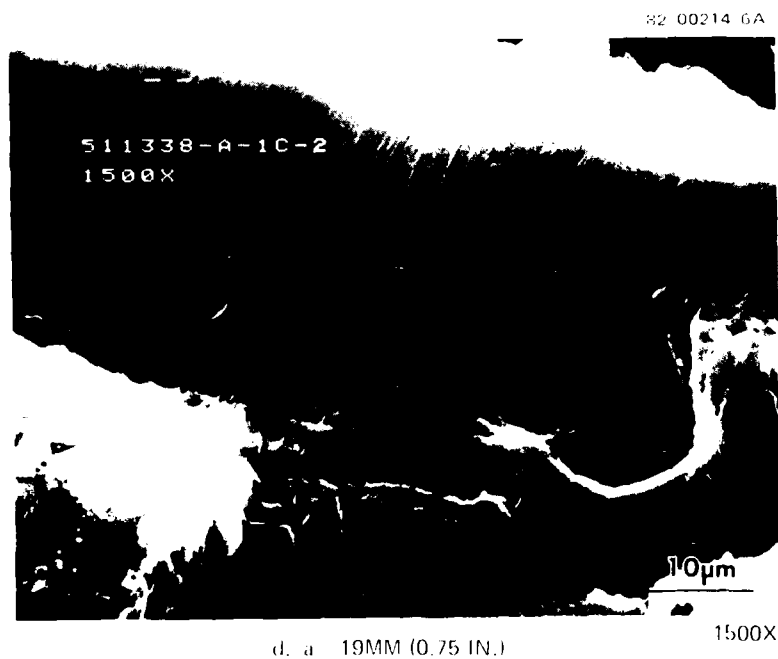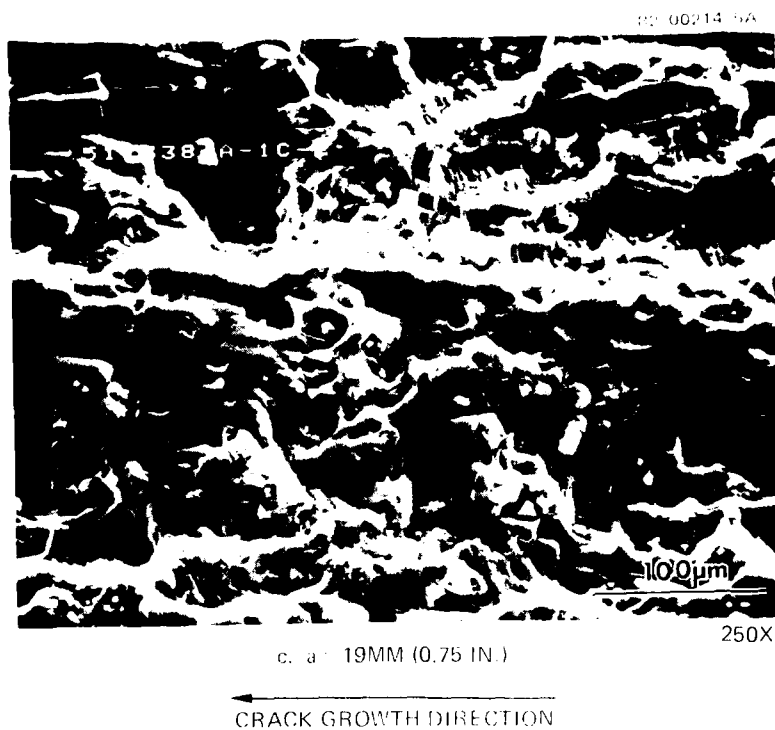
FIGURE 34. FRACTURE SURFACE OF 2024-T351 TESTED
USING TD SPECTRUM (Continued)

66

82-00214-7A

a. a = 6.4MM (0.25 IN.)   250X
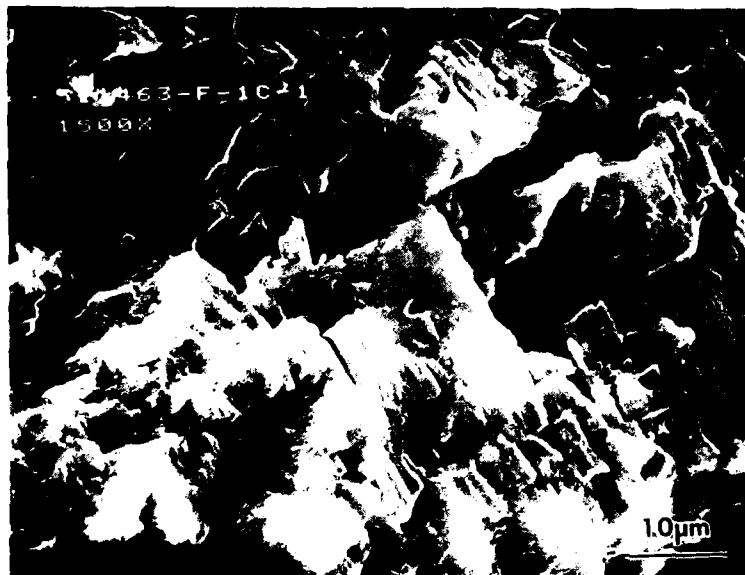
CRACK GROWTH DIRECTION
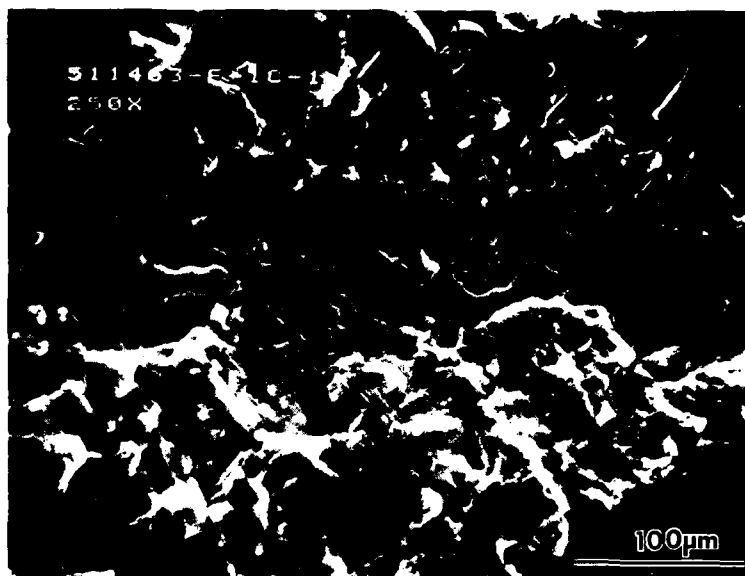
82-00214-8A

b. a = 6.4MM (0.25 IN.)   1500X

FIGURE 35. FRACTURE SURFACE OF 2024-T351 TESTED UNDER TC SPECTRUM

67
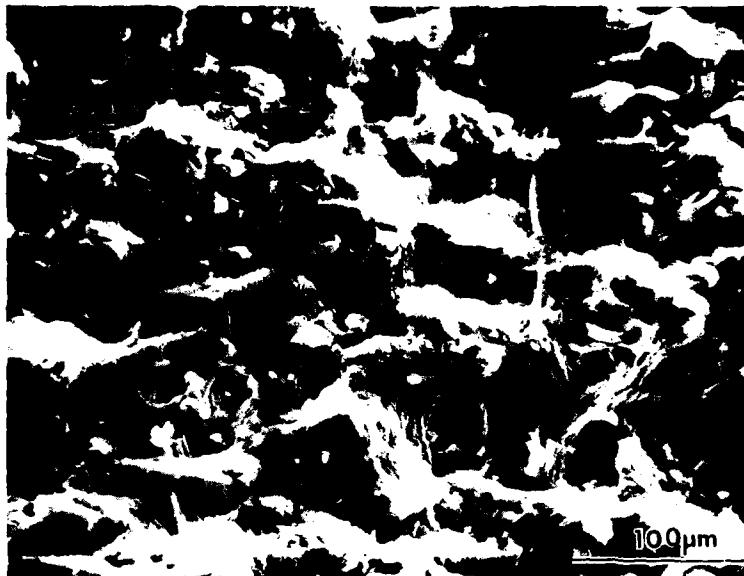
82 00214-9A

c. a — 19MM (0.75 IN.)   250X

CRACK GROWTH DIRECTION

82 00214-10A
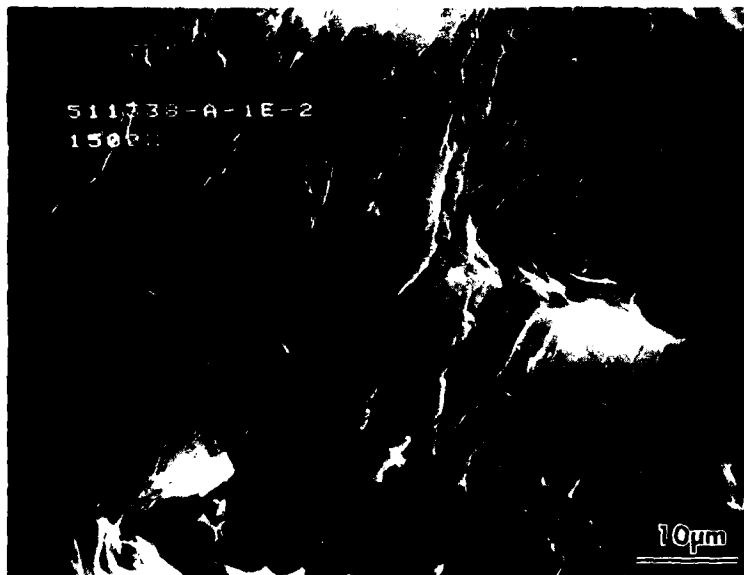
511338-A-1E-2
1500

d. a — 19MM (0.75 IN.)   1500X

FIGURE 35. FRACTURE SURFACE OF 2024-T351 TESTED
UNDER TC SPECTRUM (Continued)

The general fracture topographies are similar at the same crack lengths for both spectra (e.g., compare Figures 34a and 34b with Figures 35a and 35b). Such *similarity in fracture appearance (and, hence, FCP mechanisms) between spectra* for each alloy is consistent with the virtually identical ranking of FCP resistance for the two load histories at 145 MPa.

One subtle difference in fracture topography with load history is noticeable only in the 7XXX-type alloys. In Figure 36, arrows indicate regions on the fracture surface which appear smooth or burnished, as though contact with the mating fracture surface occurred during testing. At 1500X (Figure 36b), there is evidence of material being pushed or squeezed. Since this specimen was tested using the TC spectrum, fracture surface contact most probably occurred during compressive load excursions. In contrast, the same alloy when tested using the TD spectrum shows no evidence of abrasion on the fracture surface (Figure 37). This difference in fracture appearance probably occurs because σ_{hmin}, the minimum peak stress (valley), in the TC spectrum is approximately -90 percent of σ_{hmax}, the maximum peak stress, whereas in the TD spectrum σ_{hmin} is approximately -25 percent of σ_{hmax} (Table 1).

The general appearance at higher magnification of the fracture surfaces of all seven alloys at a = 6.4 mm reflects the respective microstructural texture of each alloy. The microstructure of all the 2XXX alloys consists of large, recrystallized grains (Figures 10 to 12). Since crack growth at relatively low K levels (i.e., shorter crack lengths) occurs along preferred crystallographic directions, such grains will cause crack deflection along these directions resulting in a rough, faceted fracture surface as can be seen for 2024-T351 in Figures 34a and 35a. The fracture surfaces of 2024-T851 and 2124-T851 at a = 6.4 mm also reflect this phenomena.

In contrast, the fracture surface of 7475-T651 at the same crack length is smooth, though FCP seems to occur on several layers or plateaus (Figure 38a). The micrograph for this alloy (Figure 16) indicates a highly textured, unre-crystallized structure. This grain structure should cause relatively little crack deflection from one grain to another and result in a smooth fracture path. It is interesting to note that the width of these plateaus on the fracture surface (as marked in Figure 38a) is of the same scale as those in the microstructure (Figure 16). A similar fracture surface appearance was noted for 7475-T7351.

82 00214 13A
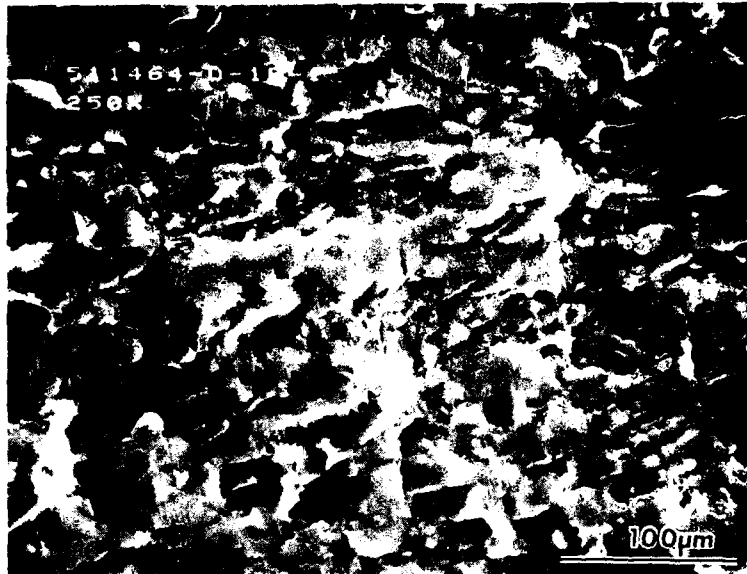
a.　250X

CRACK GROWTH DIRECTION

82-00214-14A

b.　1500X

FIGURE 36. FRACTURE SURFACE OF 7050-T73651 AT a = 6.4MM (0.25 IN.) TESTED
UNDER TC SPECTRUM. ARROWS DENOTE REGIONS OF APPARENT FRACTURE
SURFACE CONTACT AND RUBBING

a.
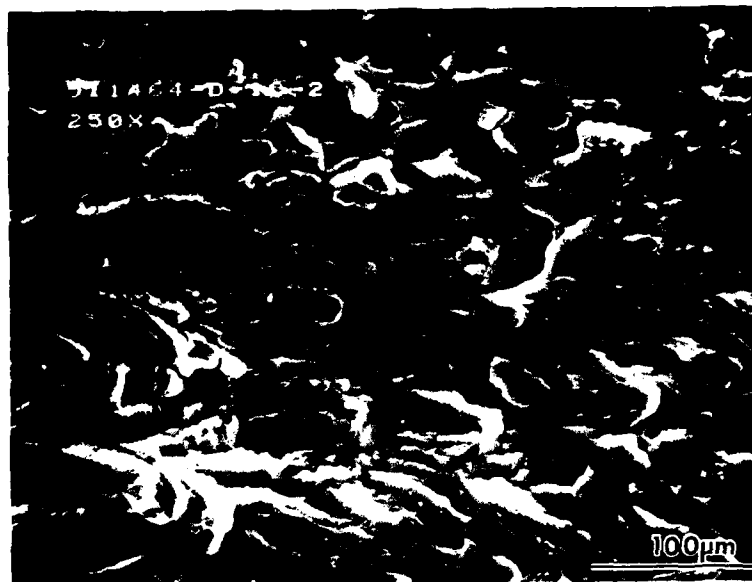
CRACK GROWTH DIRECTION

250X

b.   1500X

**FIGURE 37. FRACTURE SURFACE OF 7050-T73651 AT a = 6.4MM (0.25 IN.)
TESTED UNDER TD SPECTRUM**

82-00214-15A

PLATEAU
WIDTH
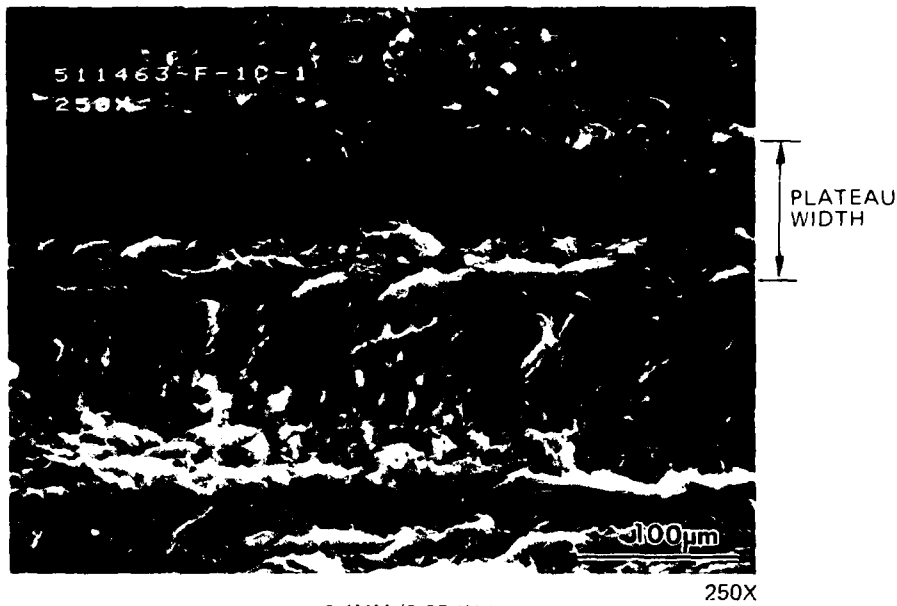
250X
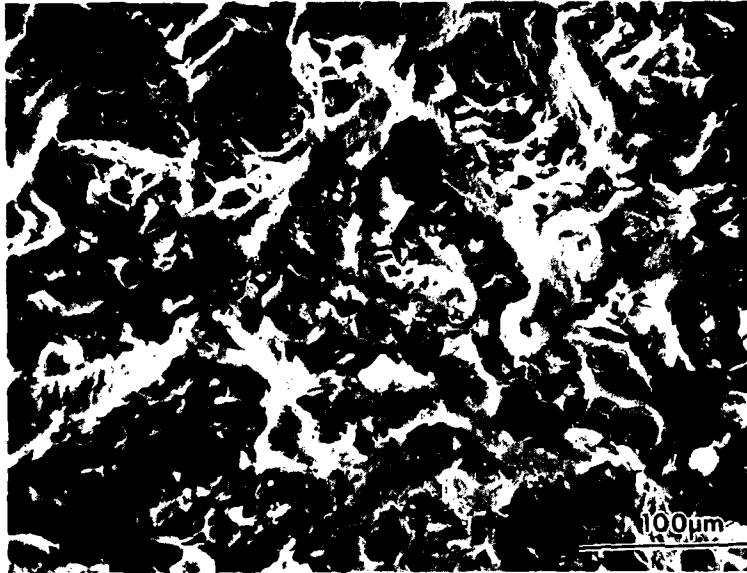
a. a = 6.4MM (0.25 IN.)

CRACK GROWTH DIRECTION

82-00214-16A

1500X

b. a = 6.4MM (0.25 IN.)

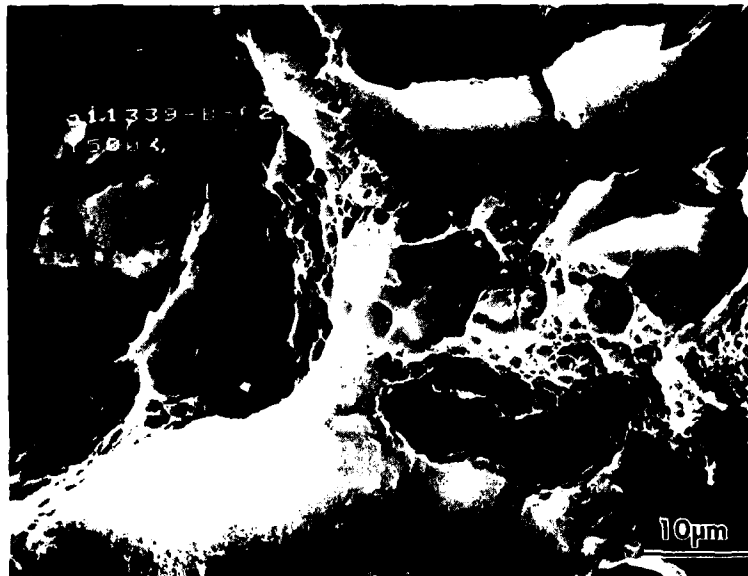FIGURE 38. FRACTURE SURFACE OF 7475-T651 TESTED UNDER TD SPECTRUM

72

c. a = 19MM (0.75 IN.)   250X

CRACK GROWTH DIRECTION

d. a = 19MM (0.75 IN.)   1500X

FIGURE 38. FRACTURE SURFACE OF 7475-T651 TESTED
UNDER TD SPECTRUM (Continued)

The fracture surface appearances of 7050-T73651 and 7075-T7351 at a = 6.4 mm fall in-between those just discussed. As Figure 36a shows, the fracture surface of 7050-T73651 is more uneven than that of 7475-T651, but not as rough as 2024-T351. Since the microstructure of this alloy (Figure 14) appears to be partially recrystallized, it follows that some local crack diversion could have occurred, thereby roughening the fracture surface to some degree. This is also the case for alloy 7075-T7351 at a = 6.4 mm.

At higher values of K_{hmax} (i.e., longer crack lengths), no correlation between general fracture topography and microstructural texture is evident for any of the seven alloys. Crack tip deformation at higher values of K_{hmax} is sufficiently extensive to modify local microstructural texture, so that the fracture surface does not reflect the original alloy microstructure.

3.7.2 Fracture of Secondary Intermetallic Particles

The influence of secondary intermetallic particles on the fatigue fracture process varies considerably between alloy/temper combinations and with crack length. At least some evidence of second phase particles, and occasional fracture of these particles, is seen for all seven alloys tested using both spectra, particularly at longer crack lengths. However, these particles are not always influential in the spectrum fatigue fracture process as discussed below.

A considerable difference in the effect of secondary intermetallic particles on fatigue fracture topography was observed between 2024-T351 and 2024-T851. Although large second phase particles are visible in 2024-T351 (Figures 34 and 35), the absence of pronounced void growth suggests that these particles played no direct role in FCP for either spectrum. Conversely, void initiation at secondary intermetallic particles and growth of these voids (Figures 39 and 40) at higher stress intensities is clearly an important crack growth mechanism in 2024-T851.

This striking change in fracture surface texture with temper in alloy 2024 reflects both the lower fracture toughness and ductility of the T851 temper. Since the matrix in this artificially-aged temper cannot accommodate crack tip plastic strains by flowing around hard second phase particles, void nucleation and growth occurs at the matrix/particle interface. In contrast, the ductile T351 temper matrix can accommodate plastic strains around these same second phase particles without pronounced void growth.

74

82-00214-19A
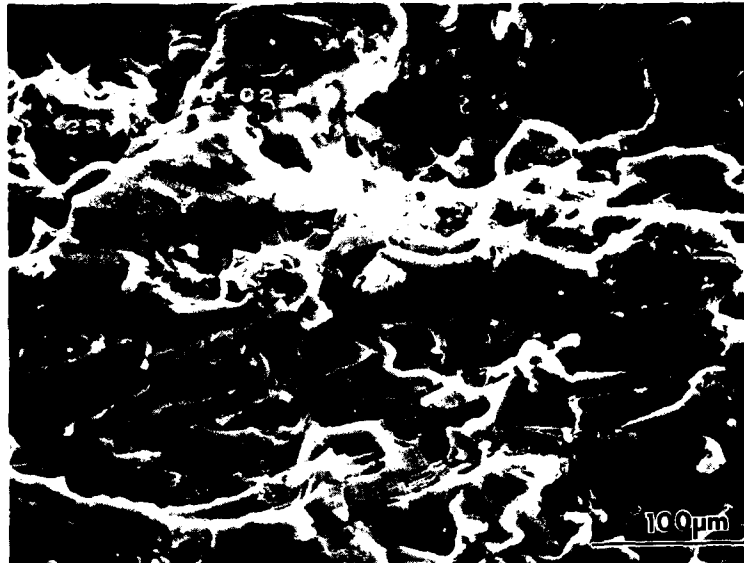
250X

a. a = 6.4MM (0.25 IN.)

CRACK GROWTH DIRECTION

82-00215-2A

1500X

b. a = 6.4MM (0.25 IN.)

FIGURE 39. FRACTURE SURFACE OF 2024-T851 TESTED UNDER TD SPECTRUM

82-00214-21A

250X

c. a = 19MM (0.75 IN.)

CRACK GROWTH DIRECTION

82-00214-20A

1500X

d. a = 19MM (0.75 IN.)

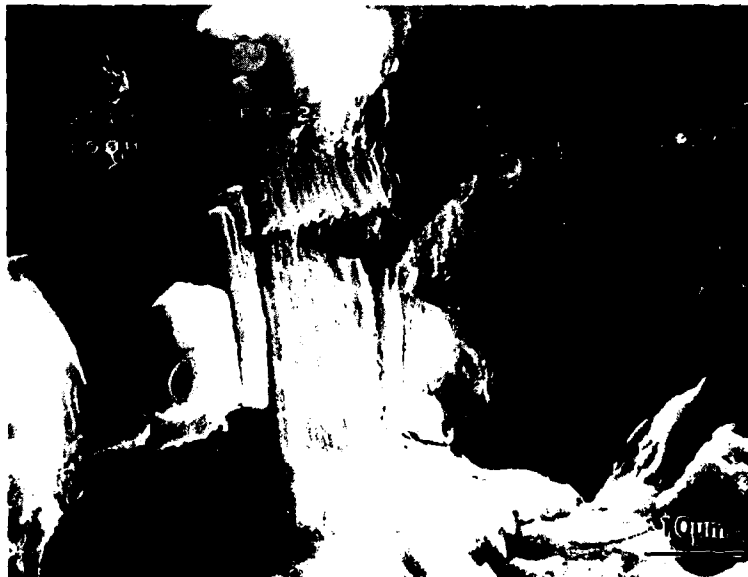**FIGURE 39. FRACTURE SURFACE OF 2024-T851 TESTED UNDER TD SPECTRUM (Continued)**

82-00215-3A
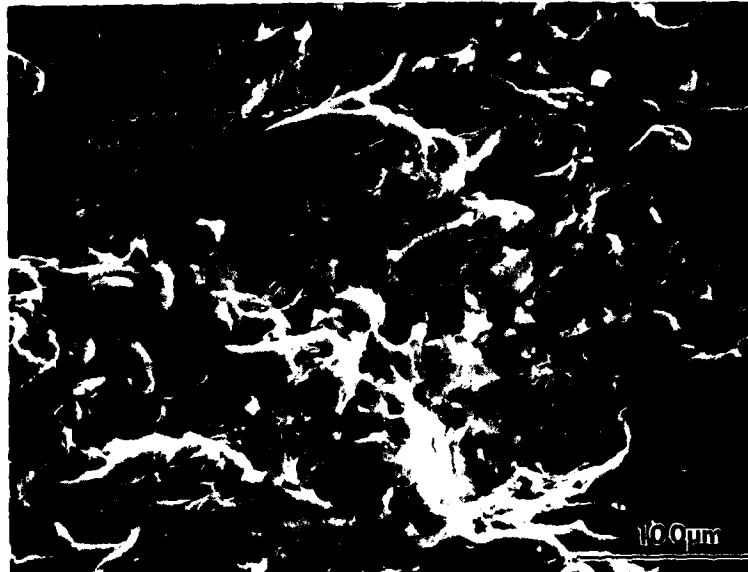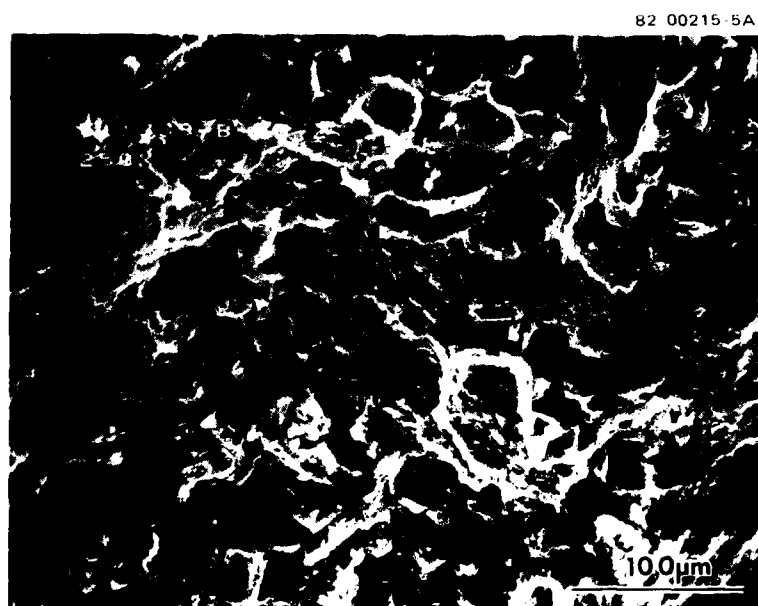

250X

a. a = 6.4MM (0.25 IN.)

CRACK GROWTH DIRECTION

82-00215-4A

1500X

b. a = 6.4MM (0.25 IN.)

FIGURE 40. FRACTURE APPEARANCE OF 2024-T851 TESTED UNDER TC SPECTRUM

82 00215-5A

250X

c. a - 19MM (0.75 IN.)

CRACK GROWTH DIRECTION

82 00215 6A

1500X

d. a - 19MM (0.75 IN.)

FIGURE 40. FRACTURE APPEARANCE OF 2024 – T851 TESTED UNDER TC SPECTRUM (Continued)

In the higher purity alloy 2124-T851, there are fewer secondary inter-metallic particles to initiate void growth (Figure 41). As a result, little or no evidence of particle-initiated fracture is visible at a = 6.4 mm (Figures 41a and 41b). However, at a = 19 mm, the matrix ductility is sufficient to cause secondary particle fracture and void growth in 2124-T851 (Figure 41c), even though the density of the second phase particles is much lower than that in 2024-T851. Crack growth at a = 19 mm is a combination of void growth and fatigue striation formation (Figures 41c and 41d), whereas in lower-purity 2024-T851 at the same crack length, crack growth is predominantly by void coalescence (Figures 39c and 39d). While the higher purity and thus higher fracture toughness of 2124-T851 does improve its spectrum FCP resistance somewhat over 2024-T851 (Figure 31), low matrix ductility for the T851 temper seems to contribute to poor performance of both alloys in this temper for both spectra used (see Figure 25b).

With the possible exception of alloy 7075-T7351 at longer crack lengths, second phase particle fracture seems to be incidental to the FCP process in all four 7XXX alloys. Figures 42 and 43 show the fracture surfaces of high-purity 7475-T7351 and alloy 7075-T7351 at the same crack length (a = 19 mm). No evidence of void growth is visible for the 7475-T7351 (Figure 42), while the fracture surface of 7075-T7351 contains many fractured intermetallic particles and large voids (Figure 43). The greater number of intermetallic particles on the 7075-T7351 fracture surface reflects the lower purity level of this alloy compared to 7475-T7351. In fact, 7475-T651 as well as 7050-T73651 are higher purity alloys in comparison to 7075-T7351. This should account for the absence of significant numbers of second phase particles on the fracture surfaces of 7050-T73651, 7475-T651, and 7475-T7351. As was the case with 2XXX alloys, however, purity alone has a minor influence on 7XXX alloy FCG resistance using these spectra. Comparison of data in Table 10 shows that an increased purity level in 7475-T7351 results in only a small increase in FCG life over that of 7075-T7351.

In addition to the fracture of second phase intermetallics, occasional secondary cracking is observed on many of the fracture surfaces, particularly at longer crack lengths. However, the causes for secondary cracking and its influence on fatigue crack growth cannot be determined from these fractographs. Futher work in this area will be done in the subsequent phases of this program.

82-00215-7A

250X

a. a = 6.4MM (0.25 IN.)

CRACK GROWTH DIRECTION

82-00215-8A

1500X

b. a : 6.4MM (0.25 IN.)

FIGURE 41. FRACTURE SURFACE OF 2124-T851 TESTED UNDER TC SPECTRUM

82-00215-9A

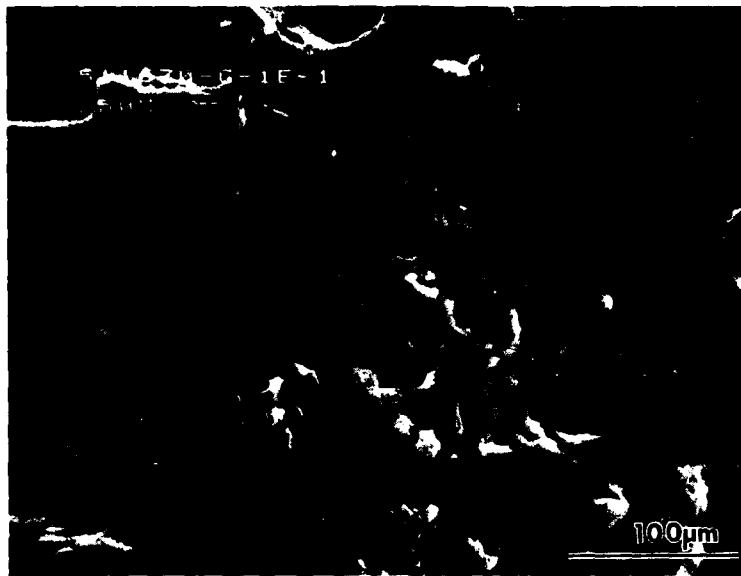c. a = 19MM (0.75 IN.)

CRACK GROWTH DIRECTION

82-00215-10A

d. a = 19MM (0.75 IN.)

FIGURE 41. FRACTURE SURFACE OF 2124-T851 TESTED UNDER TC SPECTRUM (Continued)

82-00215-11A
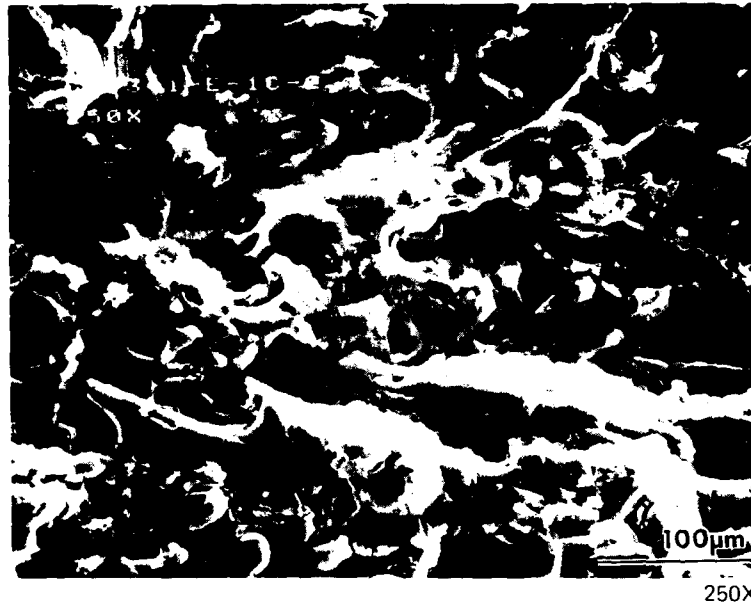
250X

a.

CRACK GROWTH DIRECTION

82-00215-12A

1500X

b.

**FIGURE 42. FRACTURE SURFACE OF 7475-T7351 AT a = 19 MM (0.75 IN.)
TESTED UNDER TC SPECTRUM**

82 00215 13A

100μm

250X

a.

CRACK GROWTH DIRECTION

82-00215-14A

10μm

1500X

b.

FIGURE 43. FRACTURE SURFACE OF 7075-T7351 AT a = 19 MM (0.75 IN.) TESTED UNDER TD SPECTRUM

3.7.3 Fracture Surface "Striations"

Another common feature on most of the fracture surfaces observed is fatigue lineage, which almost certainly represents a striation mechanism of FCG. Since, however, the random lineage spacing cannot be correlated with macroscopic growth rates, it is not possible to confirm that these are true fatigue striations. In any event, this lineage formation represents a ductile FCP mechanism which competes with void growth, and is particularly common at shorter crack lengths. The relatively fine lineage which appears at a = 6.4 mm, (e.g., for 2024-T351, Figures 34a and 34b, 35a and 35b) gradually coarsen with increasing crack length in most of the alloys (e.g., for 2024-T351, Figures 34c and 34d, 35c and 35d). This coarsening reflects higher FCP rates at longer crack length for both load spectra. However, as discussed earlier, in 2024-T851 (Figures 39c and 39d, 40c and 40d), the FCP mechanism was primarily void coalescence at a = 19 mm, and that even in 2124-T851, void coalescence was the primary mechanism and striation formation was limited (Figures 41c and 41d).
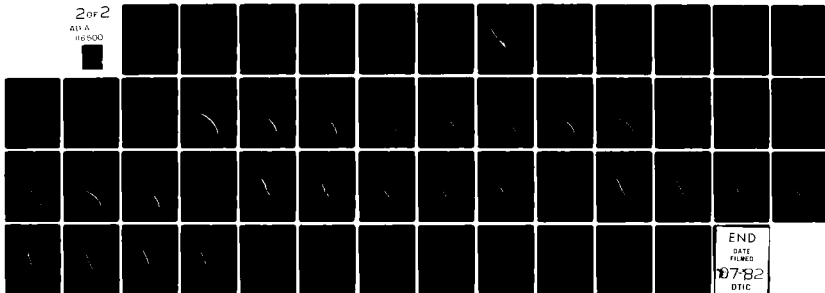
IV. SUMMARY AND CONCLUSIONS

An exploratory investigation to determine the important metallurgical factors that influence spectrum fatigue crack propagation in selected high-strength aluminum alloys is being performed. The purpose of this program is to simplify complex load histories into generic simple spectra and provide information for development and selection of fatigue resistant alloys. The results described in this report represent a baseline characterization of a number of high strength aluminum alloys for use in the investigation.

Seven commercial 2XXX and 7XXX aluminum alloys were chosen for analysis so that the influence of both purity and temper on FCP could be evaluated. All seven alloys have been characterized with respect to chemical composition, microstructure, tensile properties, and fracture toughness. FCP tests were conducted on specimens of each alloy for both constant-amplitude loading (including the low ΔK region) and two F-18 load spectra. The spectrum FCP testing was performed at a maximum peak stress of 145 MPa (21 ksi) as well as limited testing at 103 and 169 MPa (15 and 24.5 ksi) to obtain additional data at the low and high end of the crack-growth range. Pertinent fracture surface features were documented on the spectrum fatigue specimens.

The constant load amplitude FCP tests were performed on each material to provide a baseline characterization of steady-state FCP response. These data are necessary as inputs to life prediction models, which will be used to rank alloys in future programs. Fractographic analyses of these specimens will be used to help explain the spectrum fatigue results. Several observations can be made about the constant load amplitude FCP behavior of these alloys:

1. Rankings of constant load amplitude FCP resistance among the seven materials are ΔK dependent.

2. At near-threshold ΔK levels (<4 MPa $\sqrt{m}$):

   a. 2024-T351 has greater crack growth resistance than the other six alloy-temper combinations.

85

b. Among the 7XXX alloys, the near-threshold FCP resistance of 7475-T651 exceeds that of the other three 7XXX alloys: 7075-T7351, 7475-T7351, and 7050-T73651. These latter three materials have comparable near-threshold FCP behavior.

c. Near-threshold crack growth rates in 2124-T851 are between those for the 7XXX-T73 type alloys and those for 7475-T651.

d. Consistent with information in the literature, these data show that:

 i. increased aging reduces near-threshold FCP resistance.

 ii. purity (Fe, Si content) has little or no effect on near-threshold crack growth rates.

3. At intermediate ΔK levels (4 to 15 MPa$\sqrt{m}$), increased aging time reduces crack growth rates in 7475. This observation is consistent with other studies on FCP behavior of 7XXX alloys.

4. At high ΔK levels (>15 MPa$\sqrt{m}$), FCP resistance is enhanced by increased alloy toughness. Thus, higher toughness (lower strength) 2024-T351 has better FCP resistance at high ΔK than lower toughness (higher strength) 2024-T851. Similarly, higher toughness, overaged 7475-T7351 has better FCP resistance at very high ΔK (>25 MPa$\sqrt{m}$) than lower toughness, peak-aged 7475-T651.

Spectrum FCP tests were conducted on each of the seven alloys, using two complex F-18 load histories. The performance of each alloy in these spectrum tests and the relative rankings of the alloys represent useful information, but are primarily baseline information for future spectrum analyses and spectrum modifications. Several observations can be made based on the results for testing at the maximum peak stress of 145 MPa (21 ksi):

1. The ranking of the seven alloys is the same for both spectra.

2. For each material the TD spectrum consistently results in longer lives.

3. The differences in life between the two spectra for the same alloy were small — not more than an 18 percent difference for any alloy, except 2024-T351, which had a 35 percent difference.

4. Among the four 7XXX alloys tested, there was only a 25 percent difference in life between the alloy with the shortest life (7075-T7351) and the alloy with the longest life (7475-T651) for both spectra.

5. There was a much larger difference in lives among the 2XXX alloys with an 84 percent difference for the TD spectrum and a 68 percent difference for the TC spectrum between the material with the shortest life (2024-T851) and the material with the longest life (2024-T351).

For the spectrum testing at 103 MPa, which was limited to a smaller range of crack growth at lower stress intensities than those for the 145 MPa testing, it was observed that:

1. For each alloy, the TD spectrum resulted in a nearly equal or somewhat longer spectrum fatigue life than the same alloy tested with the TC spectrum.

2. Except for 2024-T351, each alloy had about the same spectrum fatigue life. The 2024-T351 alloy had a significantly longer spectrum fatigue life than the other alloys.

3. Except for 2024-T351, the rankings do not correlate with the rankings for testing at 145 MPa.

4. All the three above observations reflect the similarity of crack growth rates for all alloys except 2024-T351, which had significantly slower crack growth rates.

The spectrum testing at 169 MPa (24.5 ksi) also represented a smaller range of crack growth than the testing at 145 MPa, but overlapped the higher stress intensities of the testing at 145 MPa. Overall the rankings are similar to the results at 145 MPa with the following exceptions:

1. Alloy 2024-T351 still had the longest life for the TD spectrum; however, for the TC spectrum it had a lower life than 7050-T73651, 7475-T651, and 7475-T7351.

2. Alloys 7050-T73651 and 7475-T7351 switch rankings for both spectra, but the differences in life at 169 MPa are relatively small.

In general, the spectrum performance rankings could not be correlated with yield strength or constant amplitude FCP resistance at any ΔK level. However, spectrum performance could be correlated with fracture toughness; specifically for the testing at 145 and 169 MPa, FCP life for both spectra generally increased with increased fracture toughness.

V. FUTURE PLANS

The effort reported herein represented the first phase of a planned four-phase effort to achieve the goals outlined in Section I. Some of the significant areas to be evaluated in the following phases follow:

1. Test additional alloys and tempers to yield additional data on the effects of precipitate structure (temper), grain size, and new alloy approaches (e.g., chemistry modification and powder metallurgy). (See Figure 1.)

2. Use spectrum fatigue crack models to:

   a) Investigate alloy rankings in different load spectra, and identify features of the load history which contribute to spectrum FCP rankings.

   b) Determine the effects of material variables on spectrum FCP behavior.

   c) Simplify the spectra retaining the features that influence spectrum fatigue behavior to obtain a more economical and faster test for evaluation of spectrum fatigue behavior of high-strength aluminum alloys.

3. Correlate microstructural and fractographic features to spectrum fatigue behavior to select microstructures and simplified spectra to be used to critically examine the role of specific microstructural features on crack retardation and growth process in high strength aluminum alloys. If necessary, special alloys will be produced.

4. To identify microstructural/metallurgical factors which can be used to optimize FCGR of high strength aluminum alloys.

APPENDIX A

CONSTANT AMPLITUDE FATIGUE CRACK GROWTH RATE,
da/dN VERSUS ΔK

The first figure is a composite plot of all seven alloys followed by individual plots for each alloy.
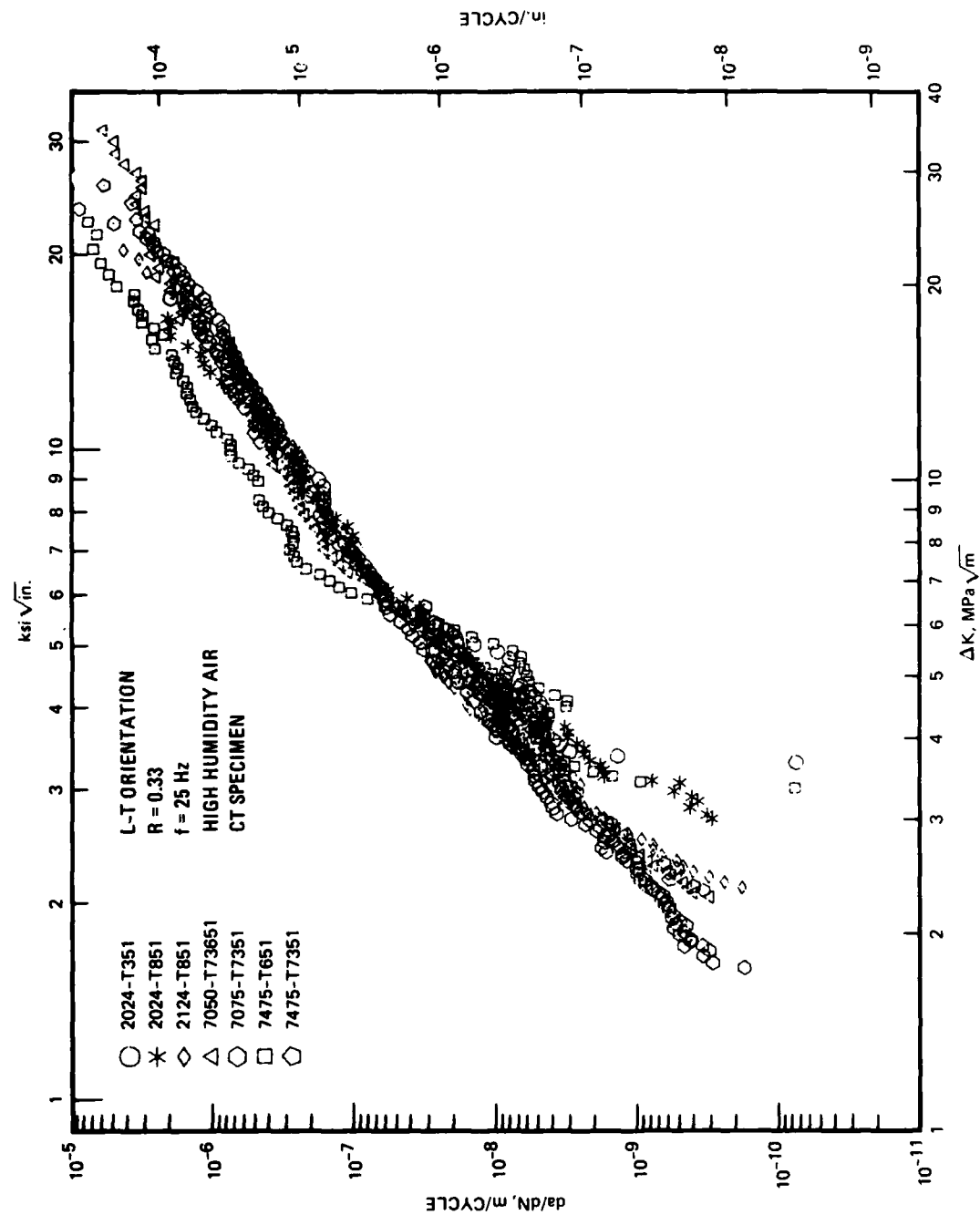
FIGURE A-1. COMPARISON OF CONSTANT LOAD AMPLITUDE FCGR DATA FOR SEVEN ALUMINUM ALLOYS
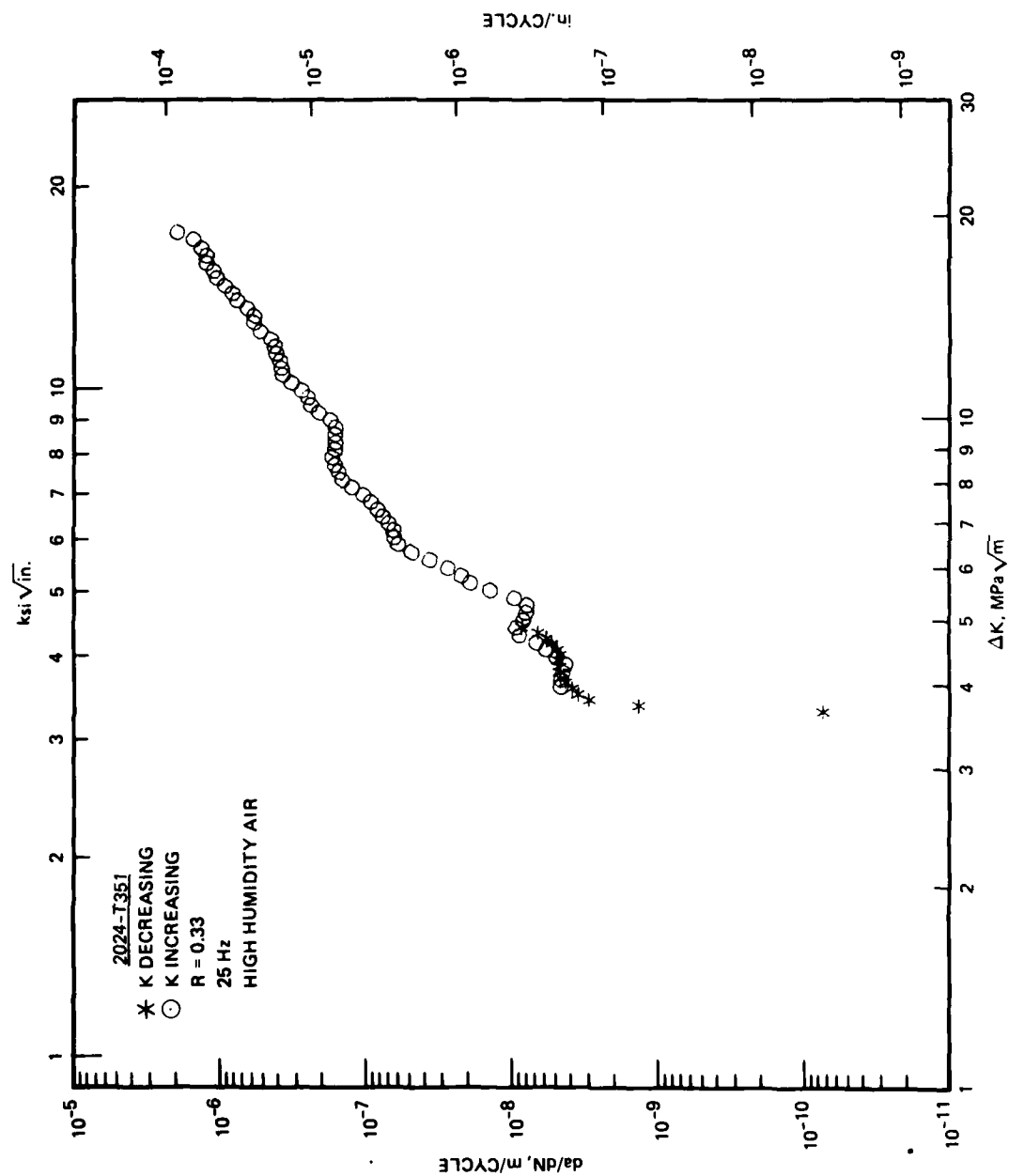
FIGURE A-2. CONSTANT LOAD AMPLITUDE FATIGUE CRACK GROWTH RATE DATA FOR 2024-T351
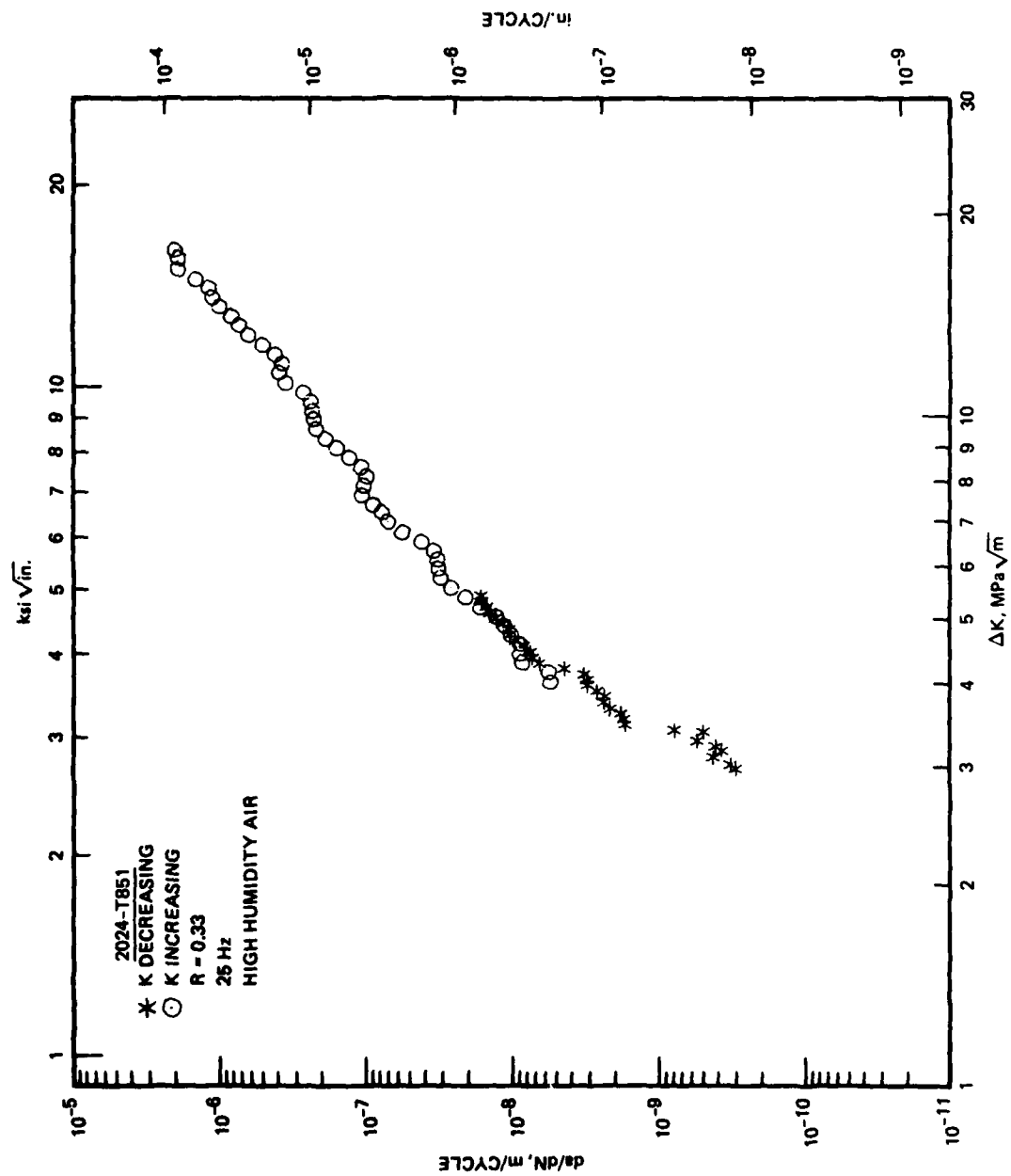
FIGURE A-3. CONSTANT LOAD AMPLITUDE FATIGUE CRACK GROWTH RATE DATA FOR 2024-T851
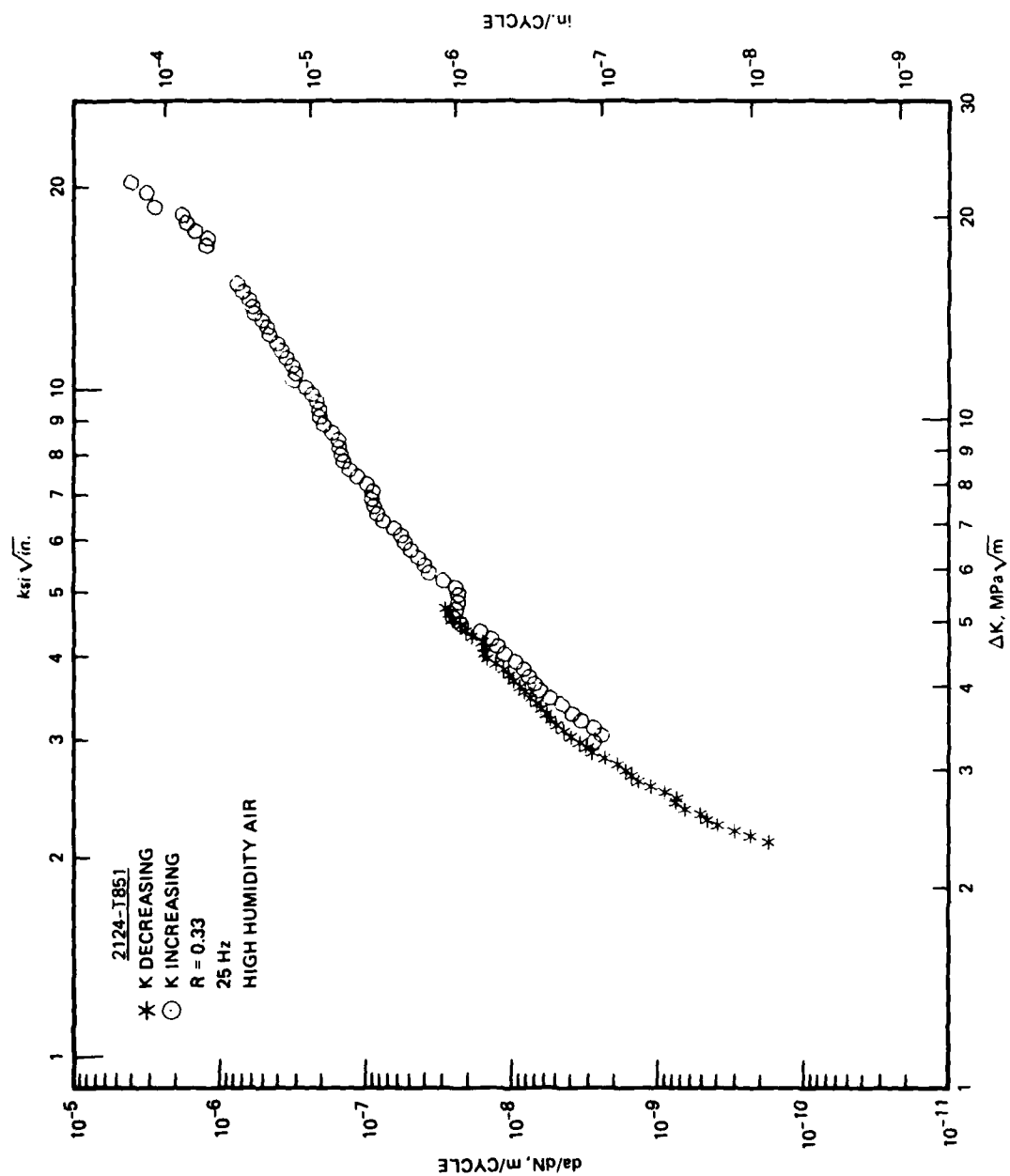
FIGURE A-4. CONSTANT LOAD AMPLITUDE FATIGUE CRACK GROWTH RATE DATA FOR 2124-T851
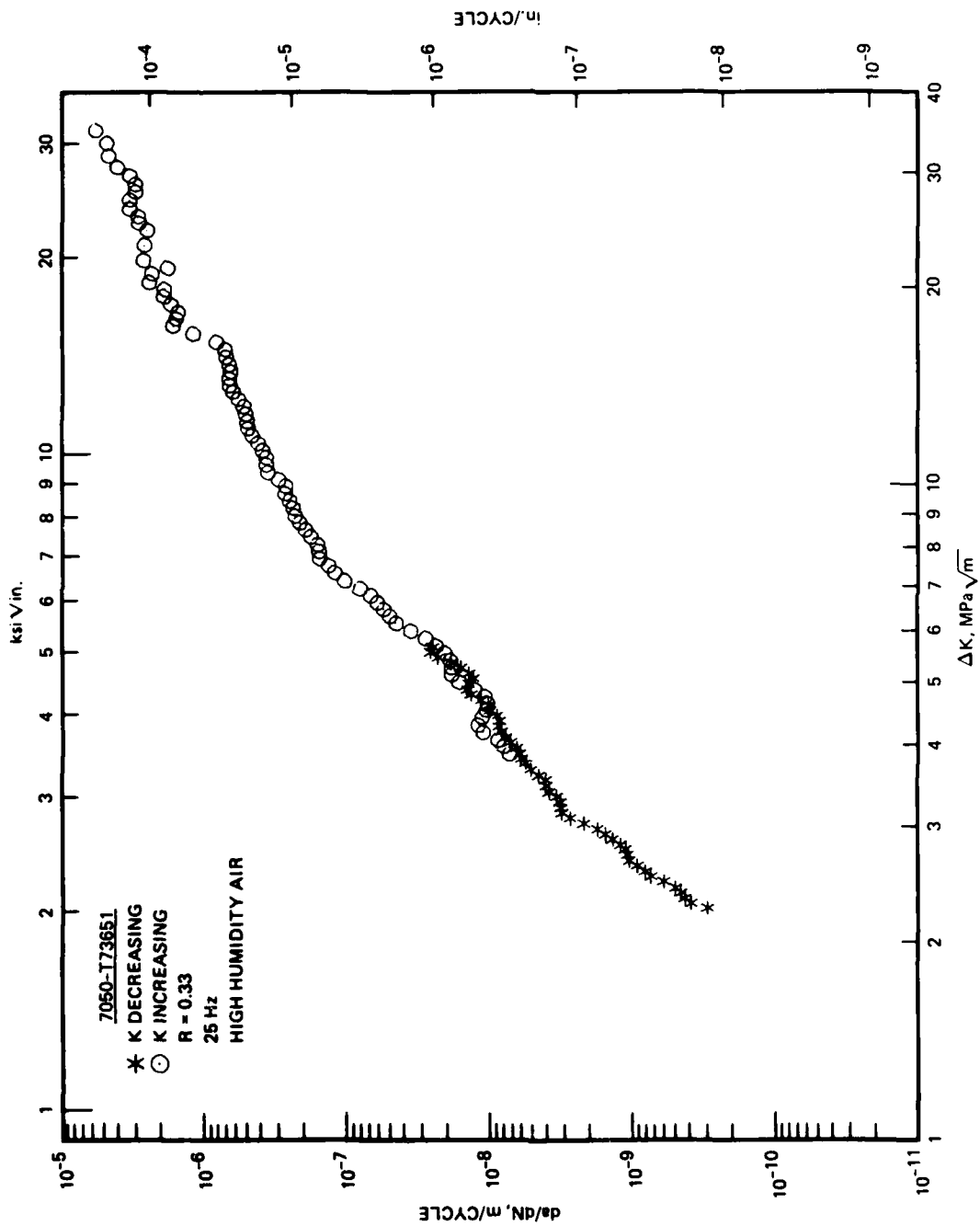
FIGURE A-5. CONSTANT LOAD AMPLITUDE FATIGUE CRACK GROWTH RATE DATA FOR 7050-T73651
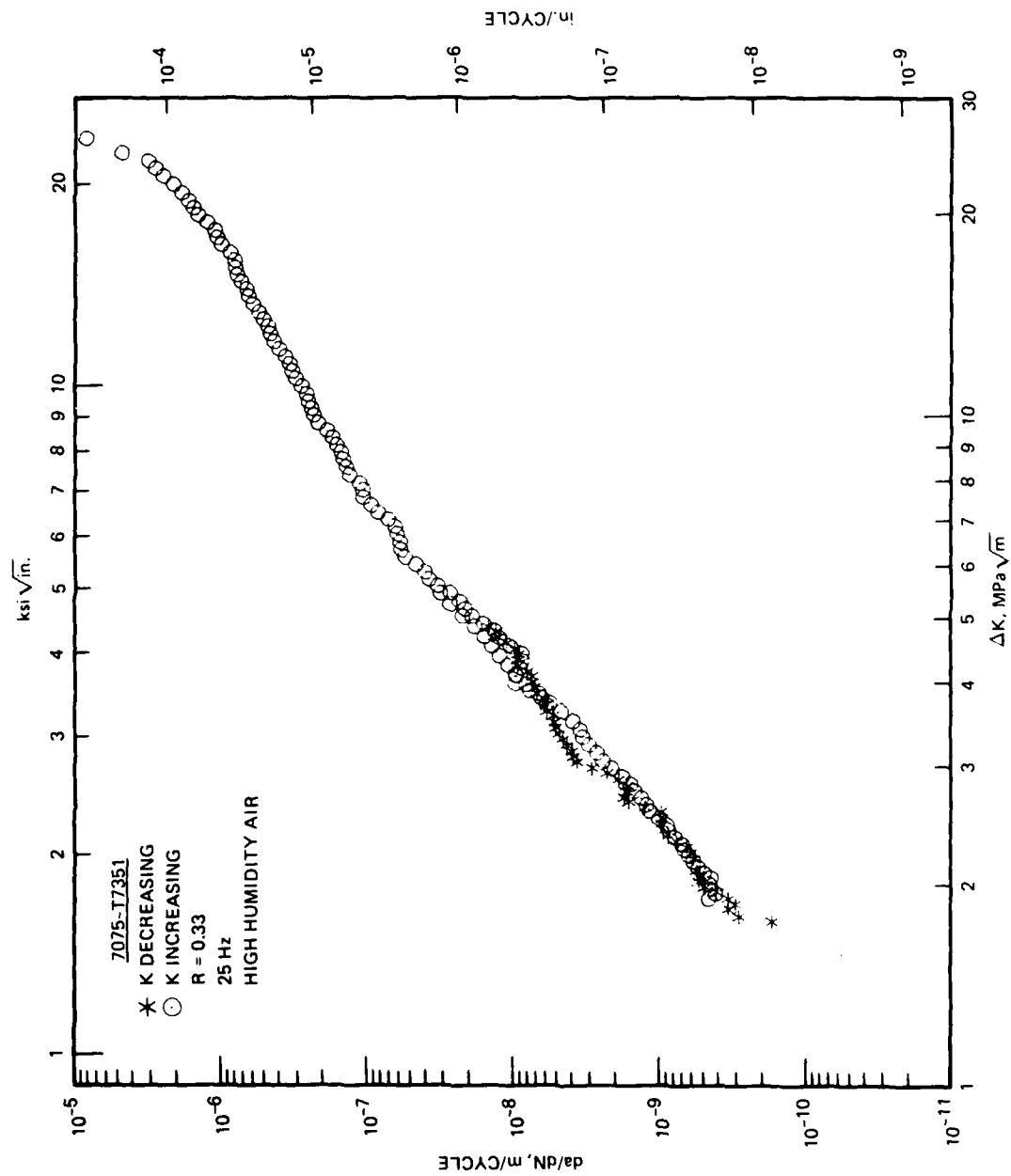
FIGURE A-6. CONSTANT LOAD AMPLITUDE FATIGUE CRACK GROWTH RATE DATA FOR 7075-T7351

96
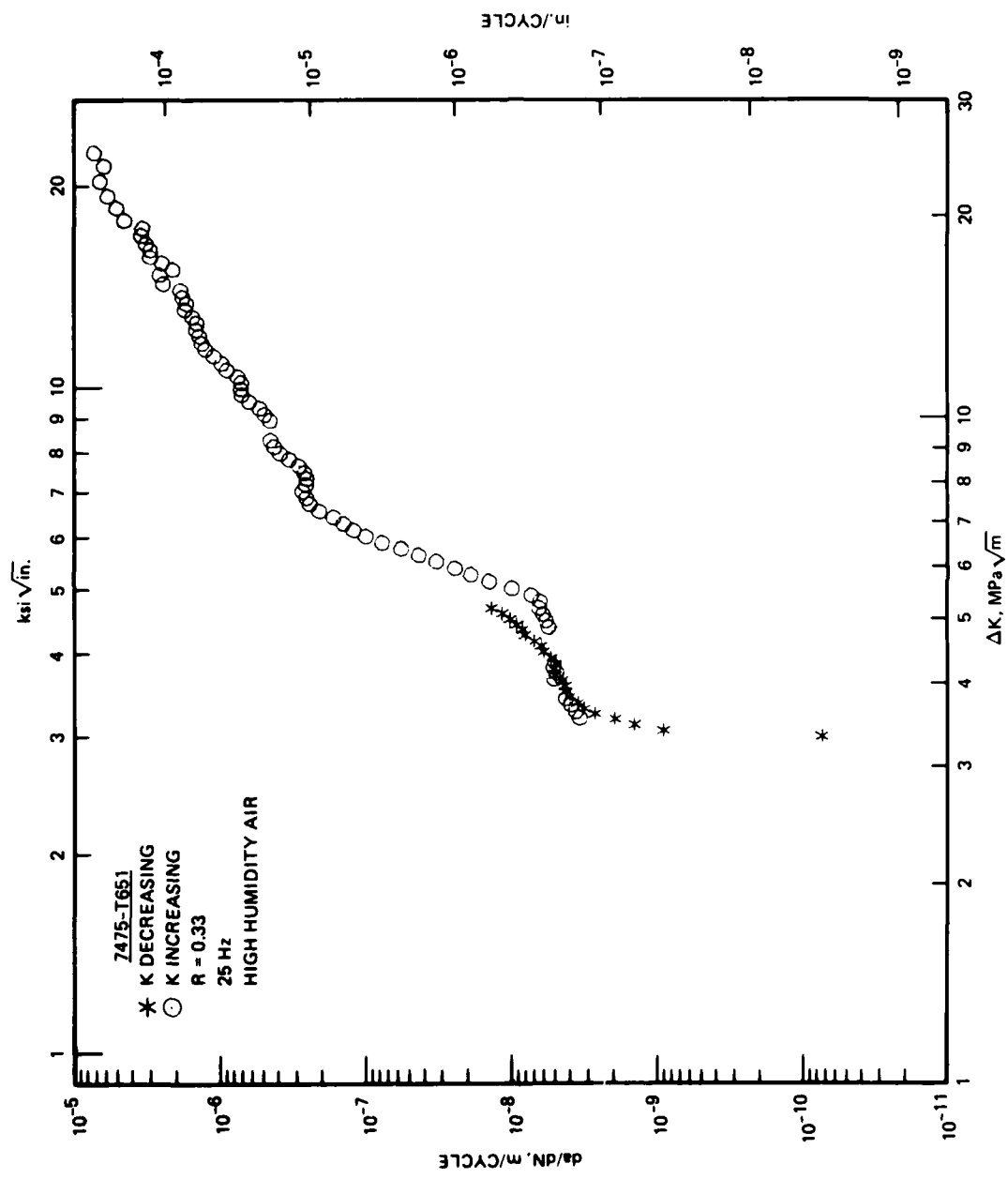
FIGURE A-7. CONSTANT LOAD AMPLITUDE FATIGUE CRACK GROWTH RATE DATA FOR 7475-T651
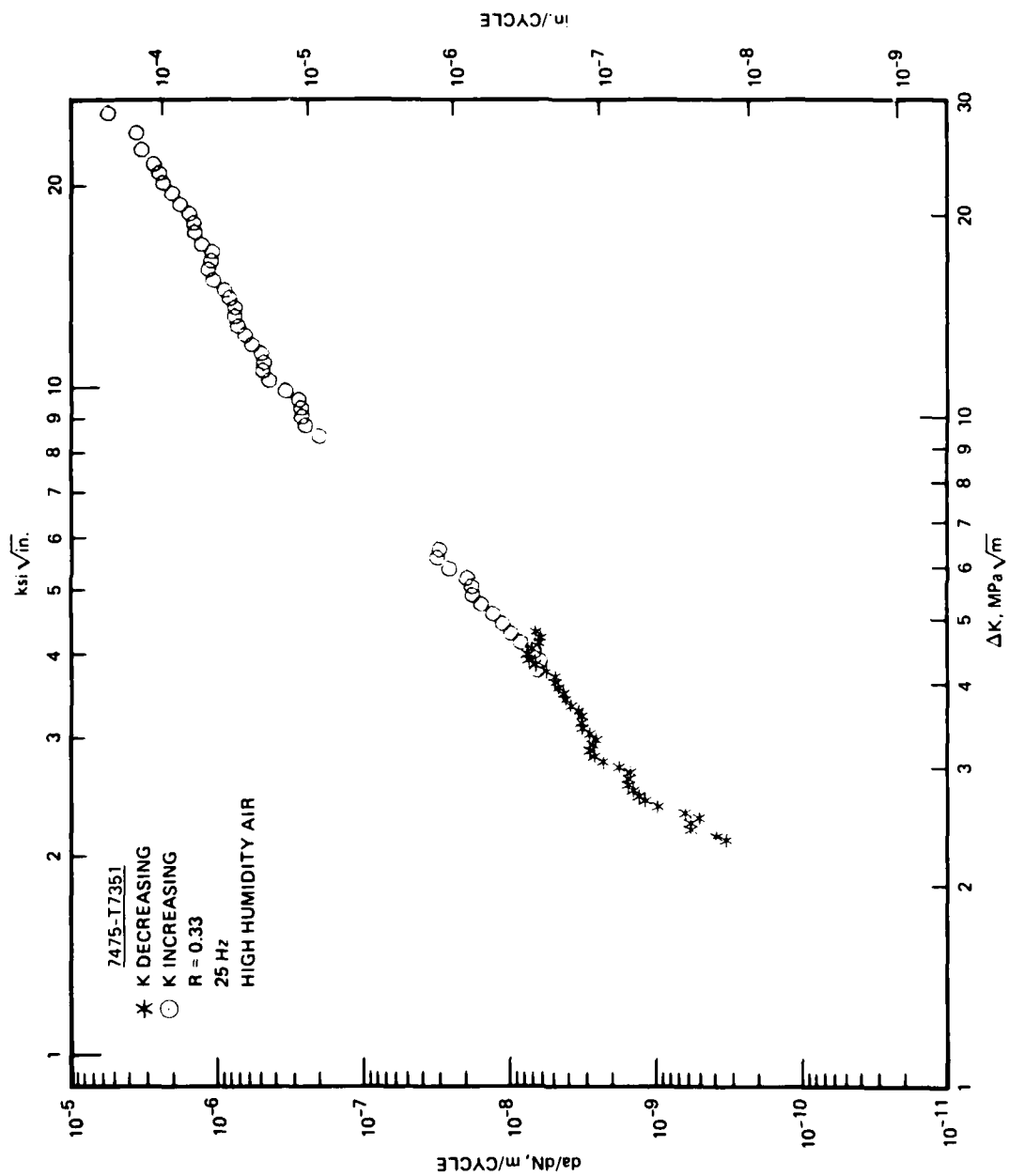
FIGURE A-8. CONSTANT LOAD AMPLITUDE FATIGUE CRACK GROWTH RATE DATA FOR 7475-T7351

APPENDIX B

CRACK LENGTH VERSUS SIMULATED FLIGHT HOURS, a VERSUS H

1. The scale for the ordinate (a) is the same for each graph; the scale for the abscissa (H) varies.

2. Two specimens each were tested at 145 MPa and 103/169 MPa.

3. Data are in numerical order by alloy designation with TD spectrum first, then TC spectrum.

4. The tension-dominated (TD) spectrum representing the lower wing root load history of the F-18 is coded C2 at Northrop and the tension-compression (TC) spectrum representing the horizontal hinge tail moment load history is coded E3.

5. All data are plotted in this appendix, although not all portions were used for analysis, see text – particularly Figure 8, and Appendix C notes.

6. Crack length was measured at the end of one or more passes (300 simulated flight hours per pass) of the spectrum, which at the beginning of the 103 and 145 MPa tests resulted in the crack growth increment being less than 0.25 mm which is required by ASTM E647. (Note that ASTM E647 method is a constant amplitude method for fatigue crack growth.) However, in calculating crack growth rates, the 0.25 mm increment requirement was observed. At the higher crack growth rates, the one per pass crack measurement resulted in larger crack growth increments than required by ASTM 647.

7. Graphs were plotted using a Northrop Support Services Laboratory computer program designated $SPECPT from data on files designated .DDN, created from crack length measurement versus pass raw data.
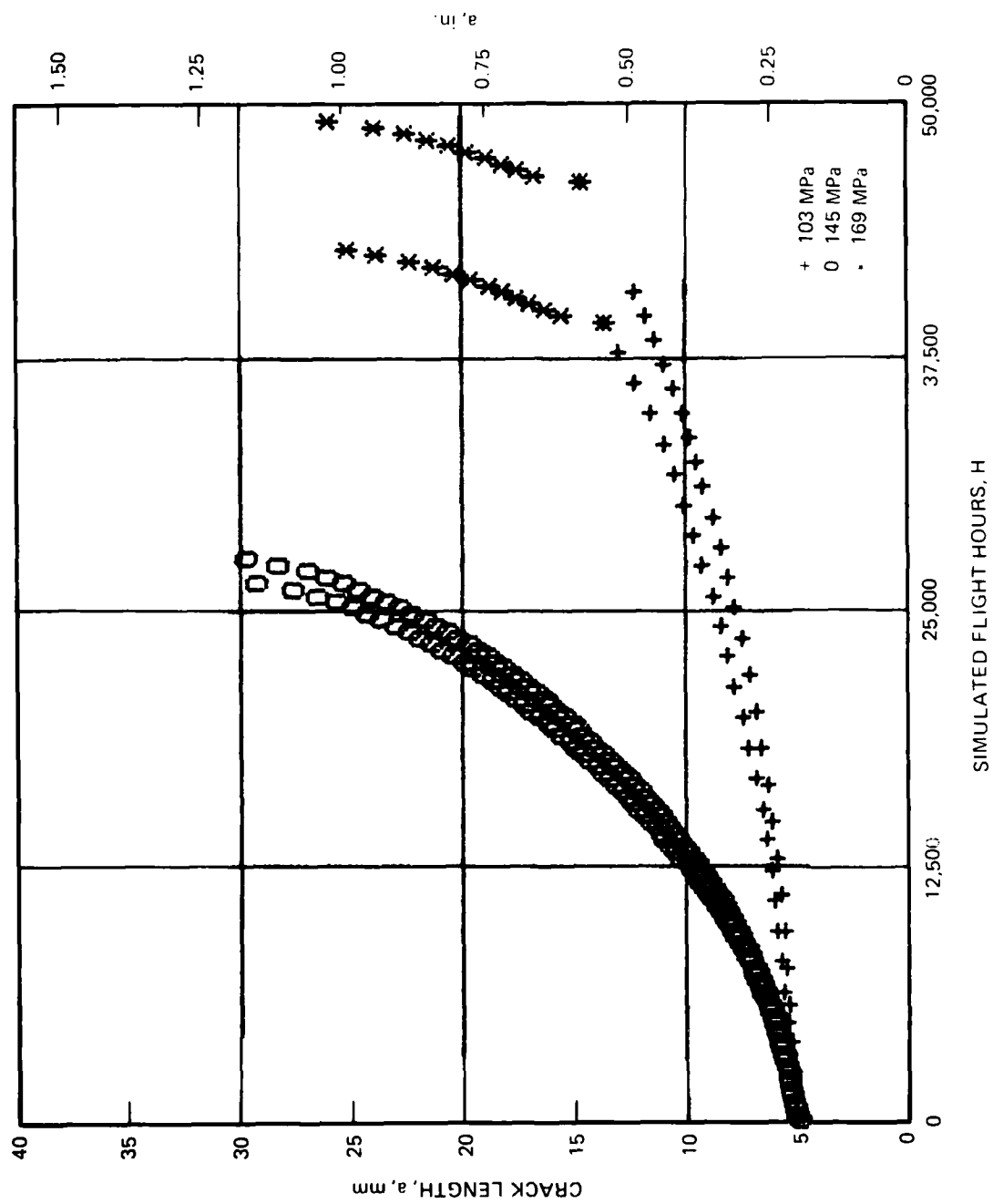
FIGURE B-1. 2024–T351, TD SPECTRUM
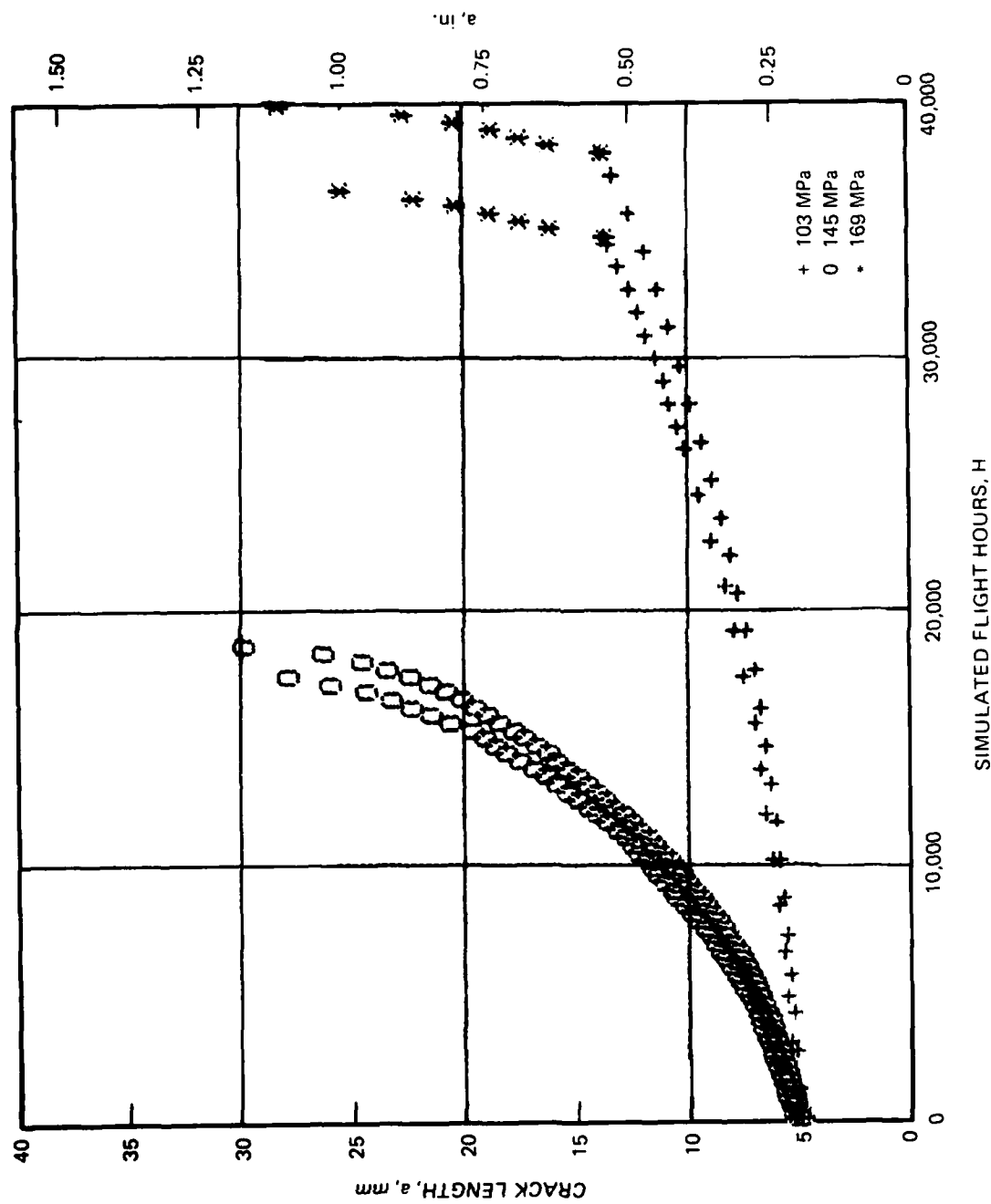
FIGURE B-2. 2024-T351, TC SPECTRUM
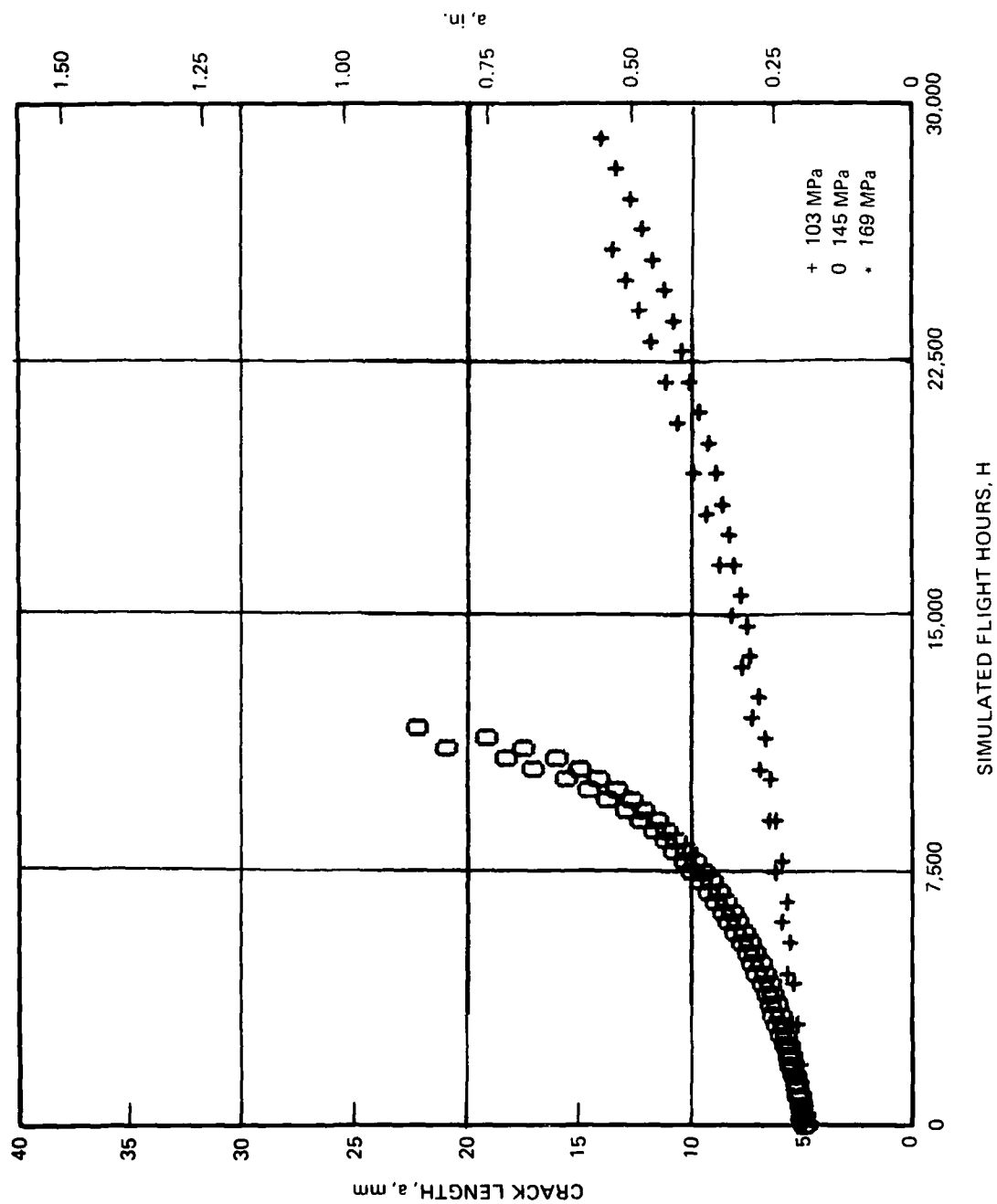
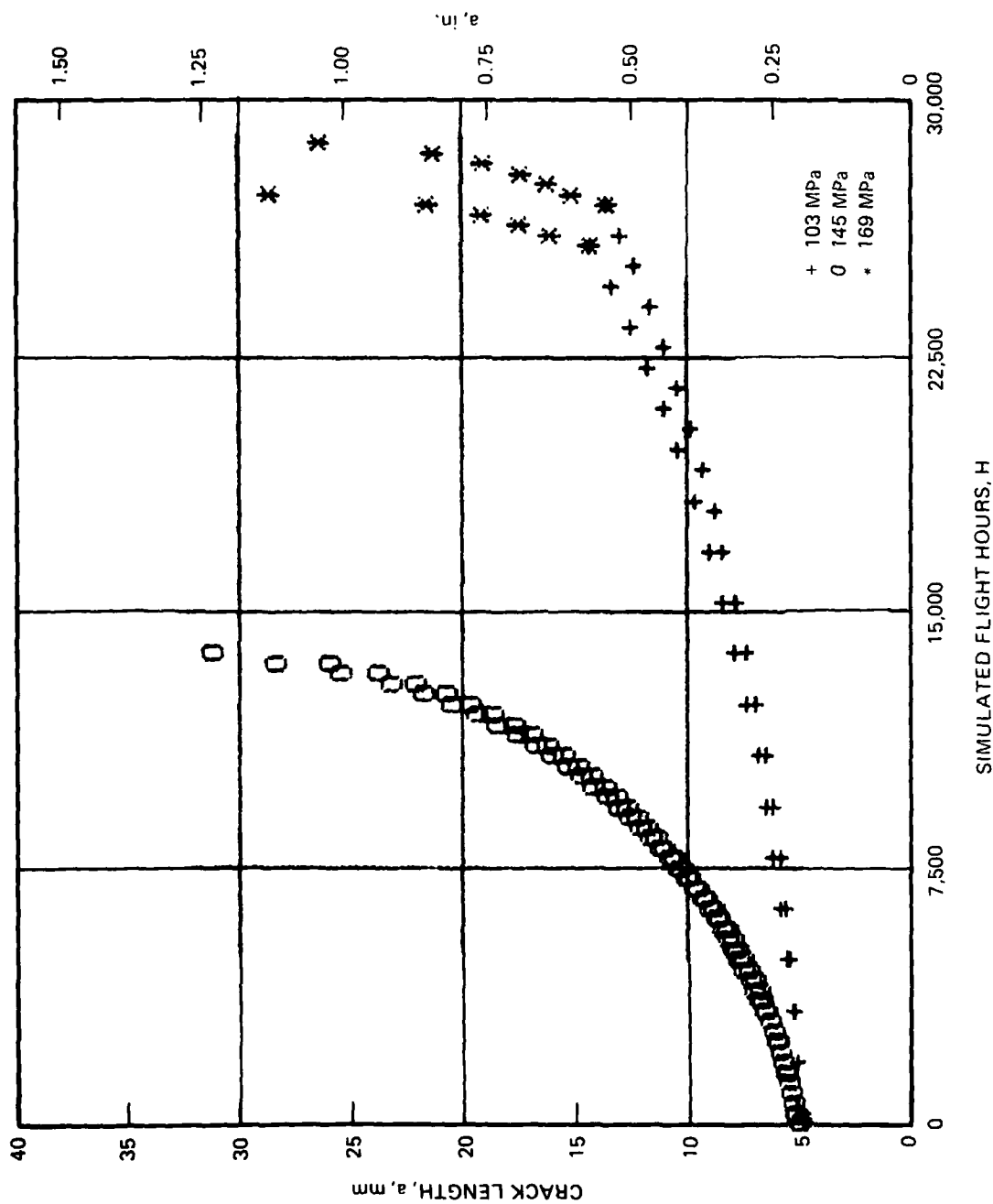FIGURE B-3. 2024-T851, TD SPECTRUM
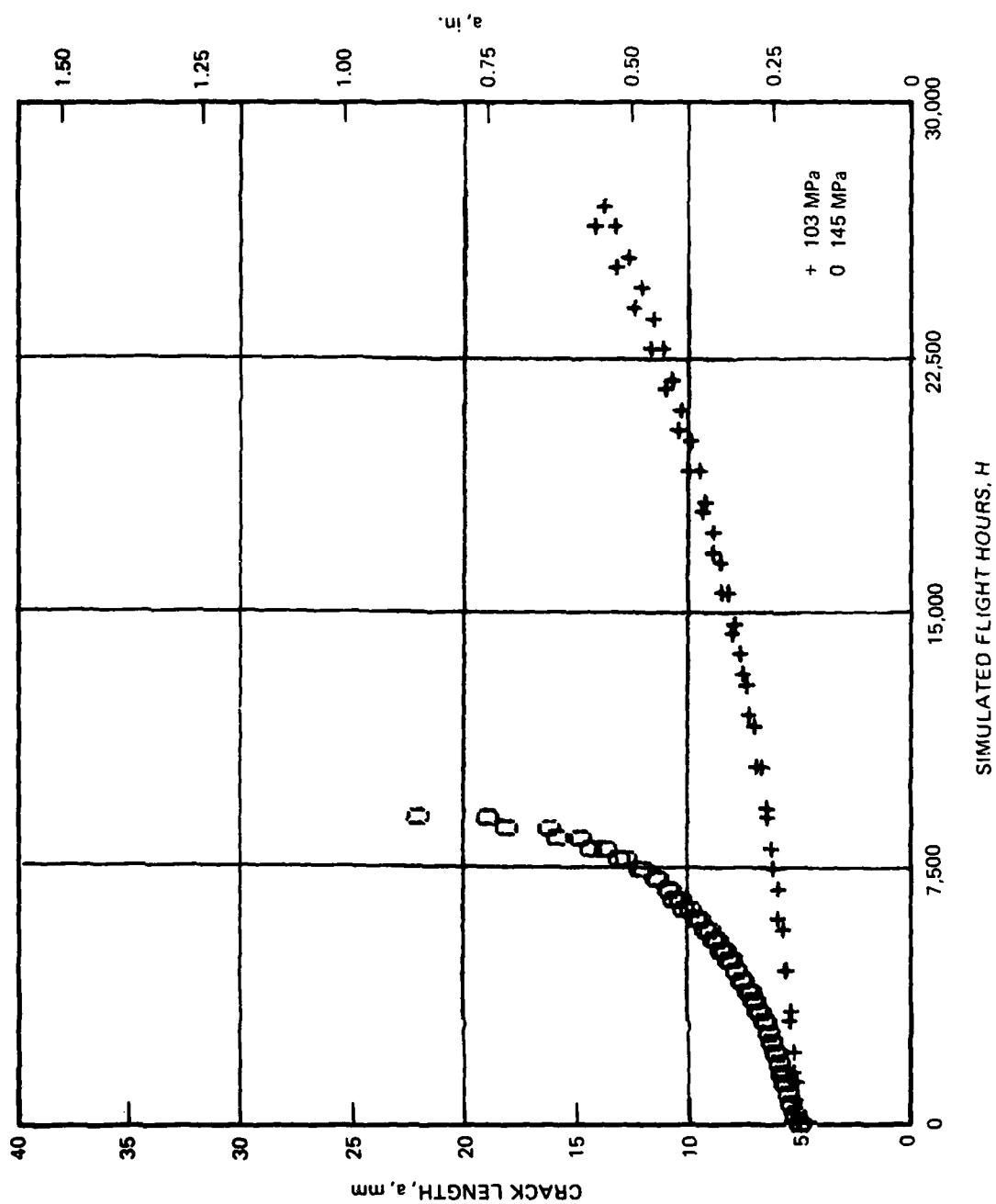
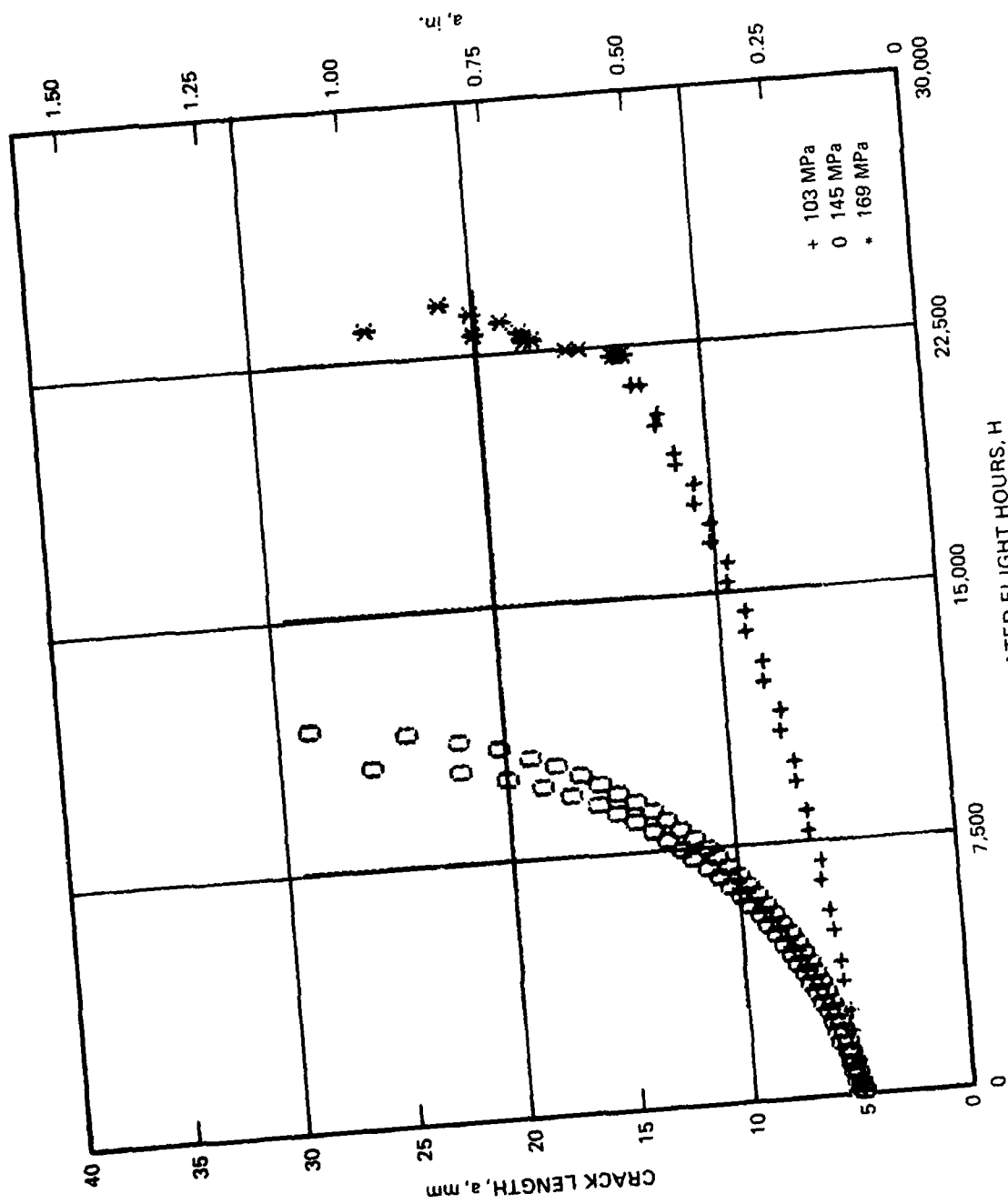FIGURE B-4. 2024-T851, TC SPECTRUM

FIGURE B-5. 2124-T851, TD SPECTRUM
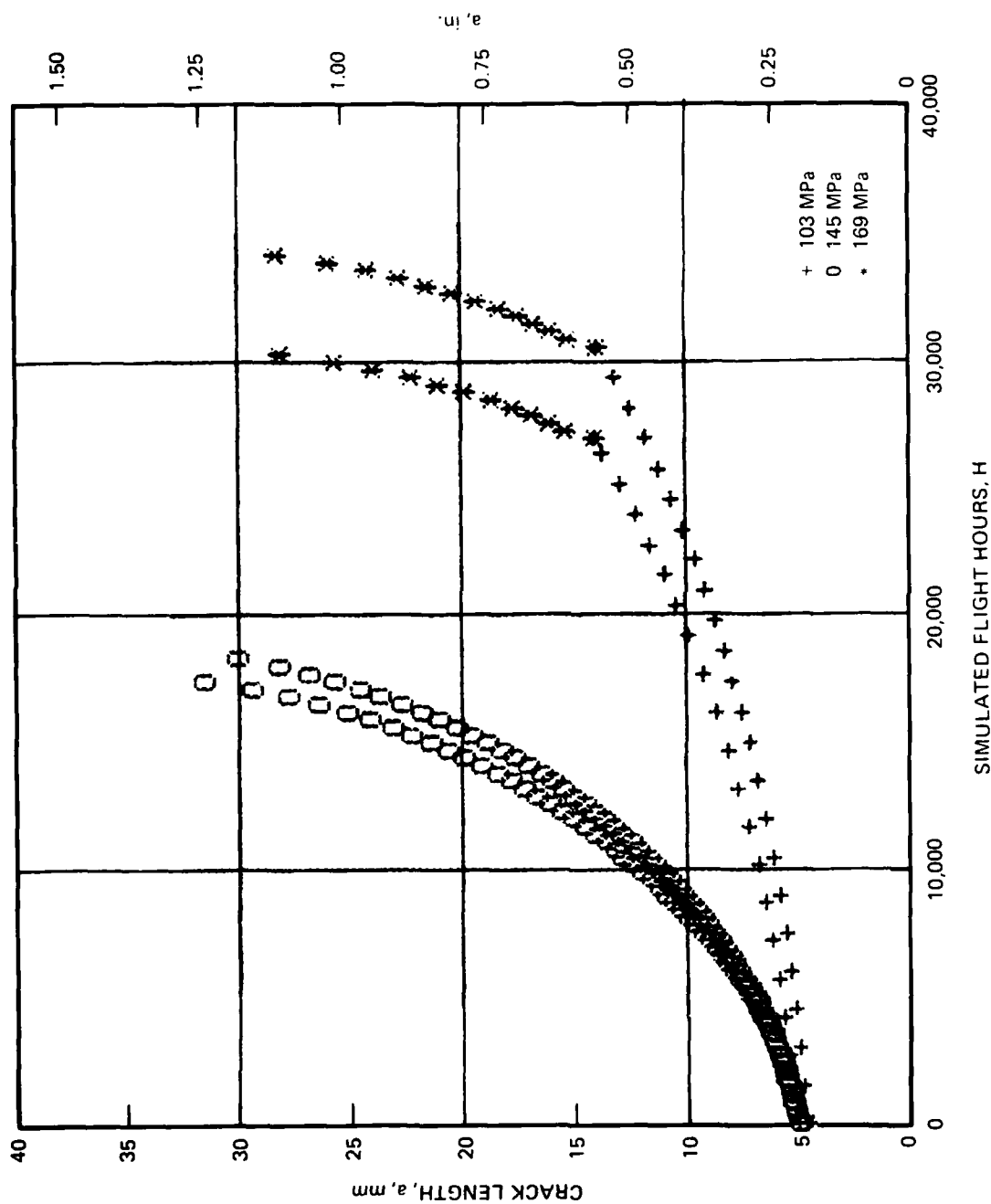
104

FIGURE B-6. 2124-T851, TC SPECTRUM
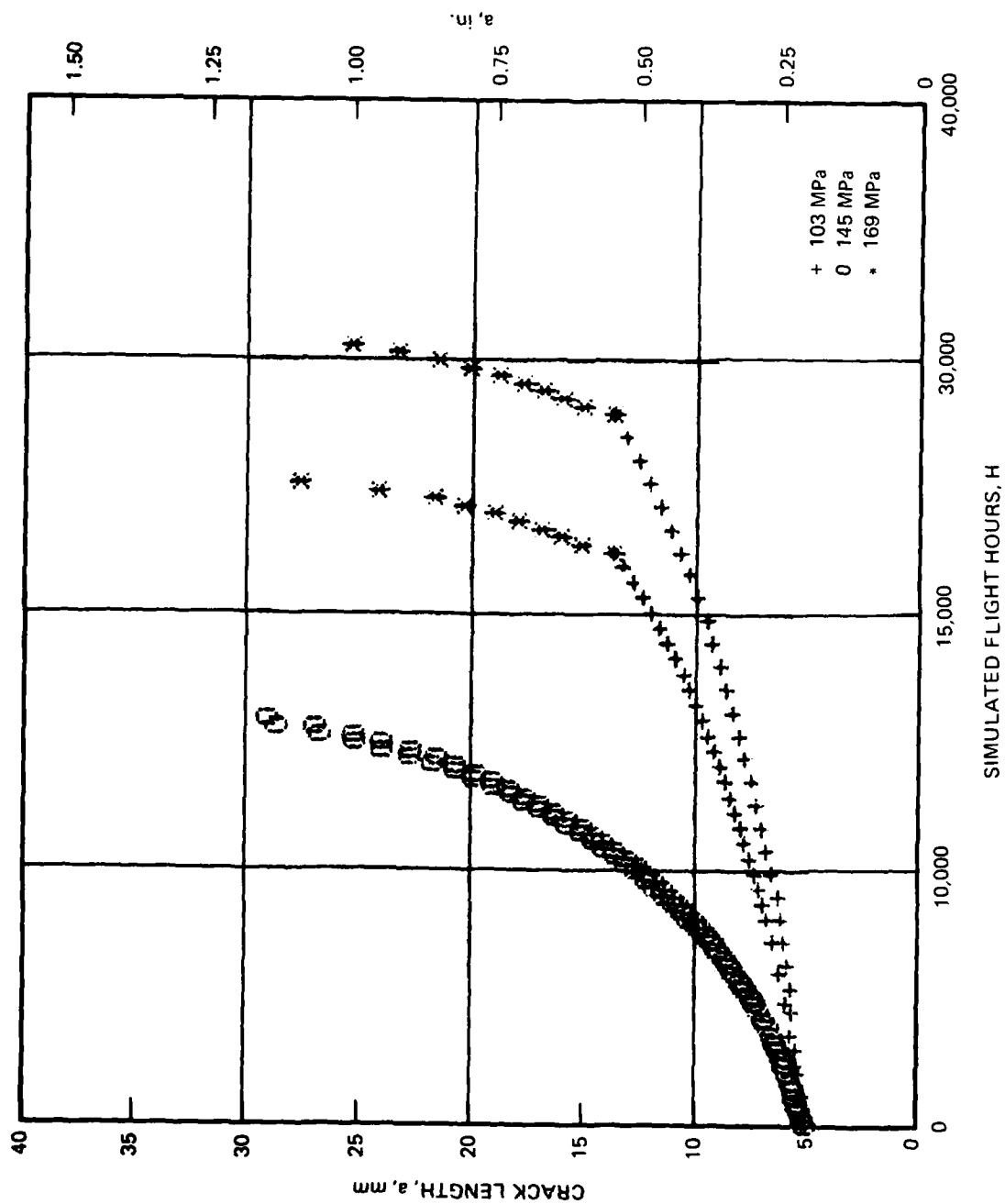
FIGURE B-7. 7050-T73651, TD SPECTRUM
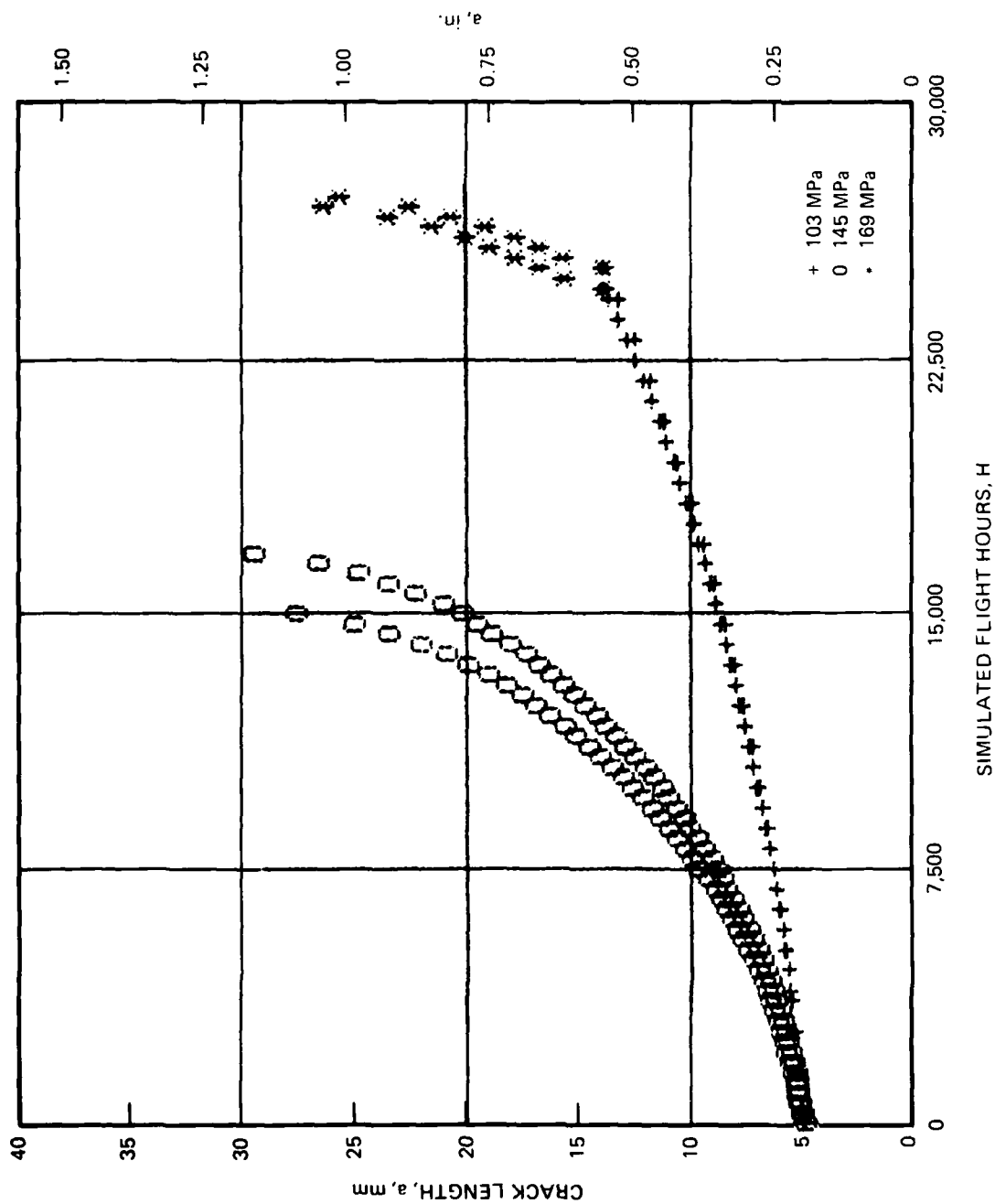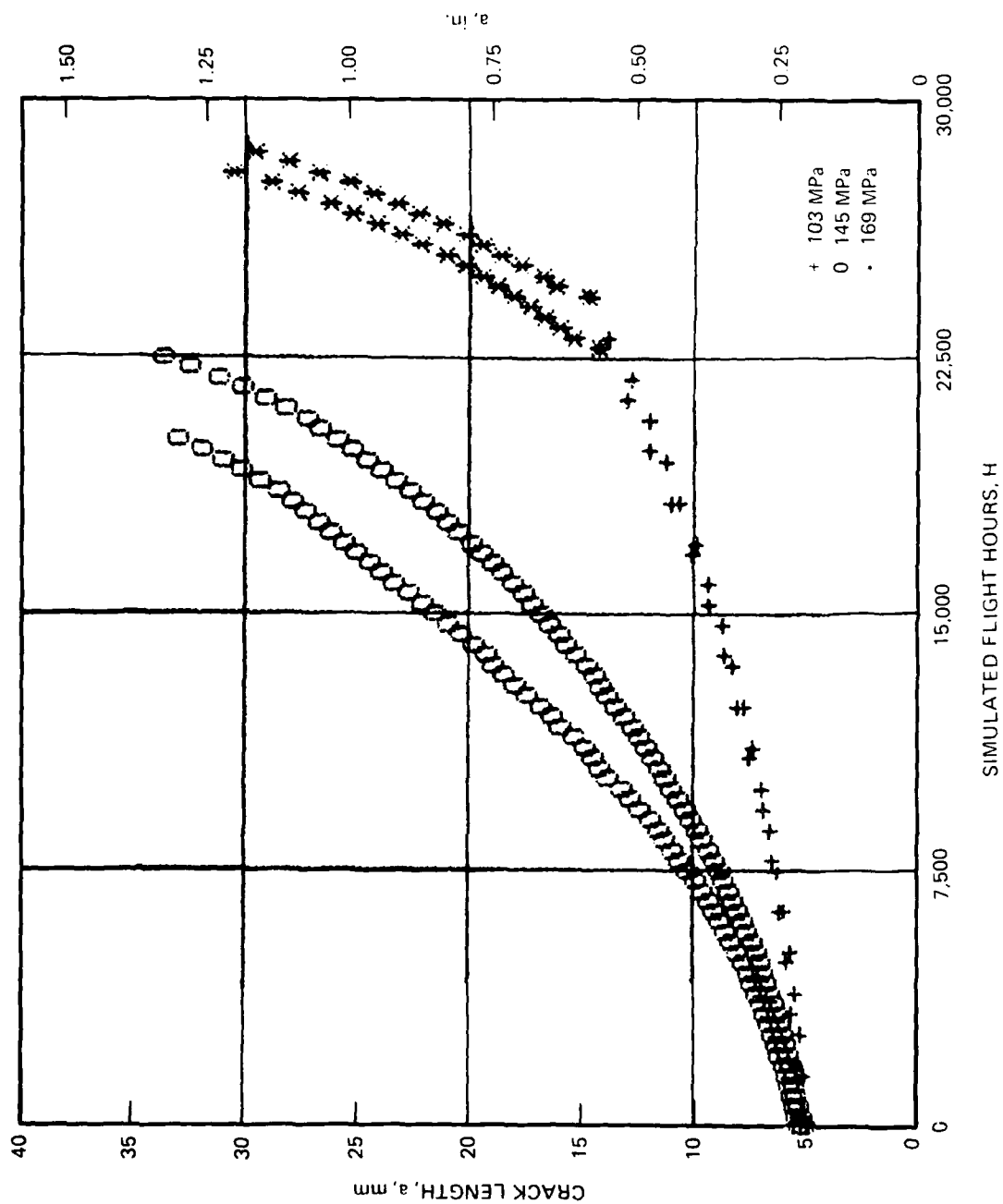
106

FIGURE B-8. 7050-T73651, TC SPECTRUM

FIGURE B-9. 7075-T7351, TD SPECTRUM

SIMULATED FLIGHT HOURS. H
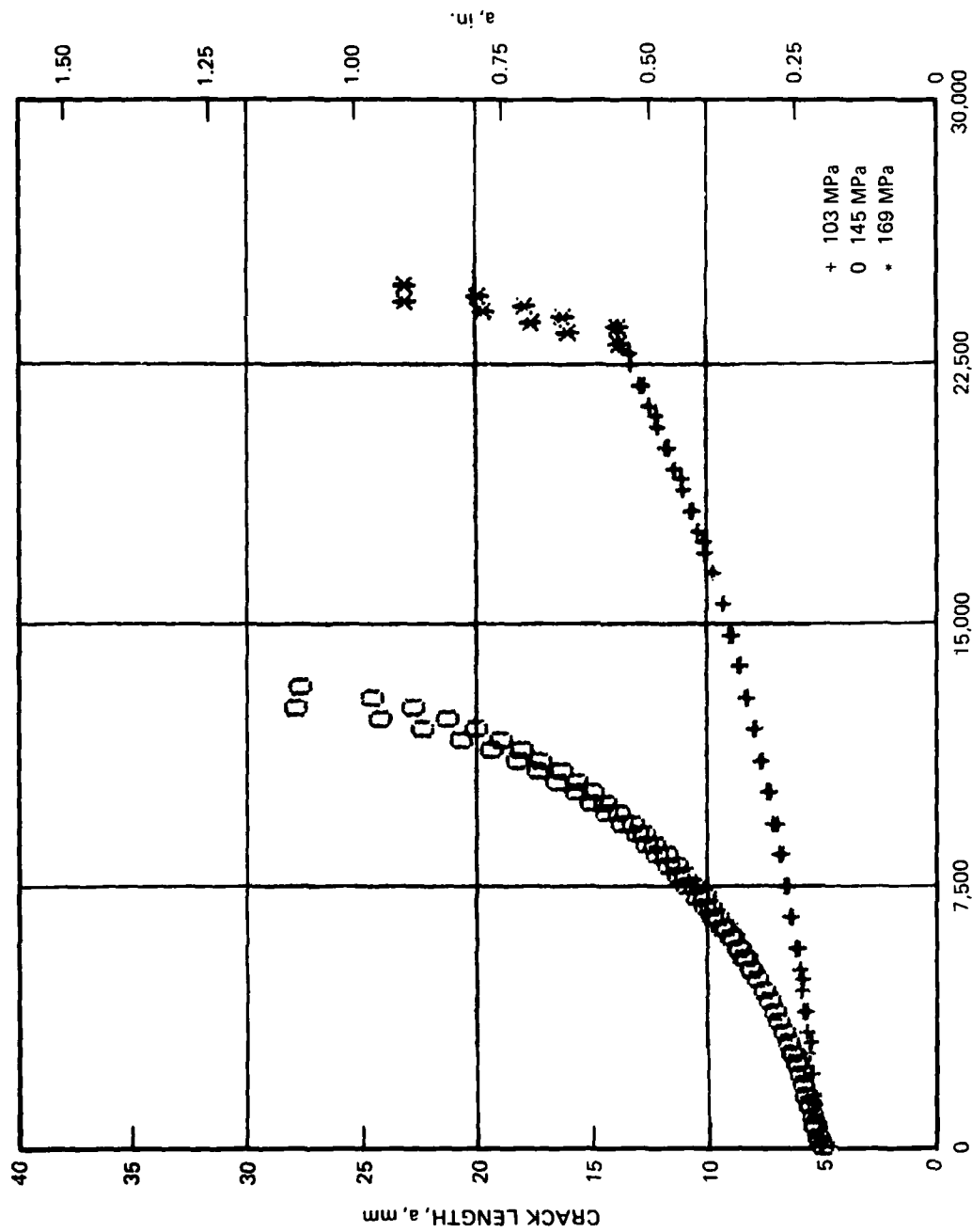
FIGURE B-10. 7075-T7351, TC SPECTRUM

109

FIGURE B-11. 7475-T651, TD SPECTRUM
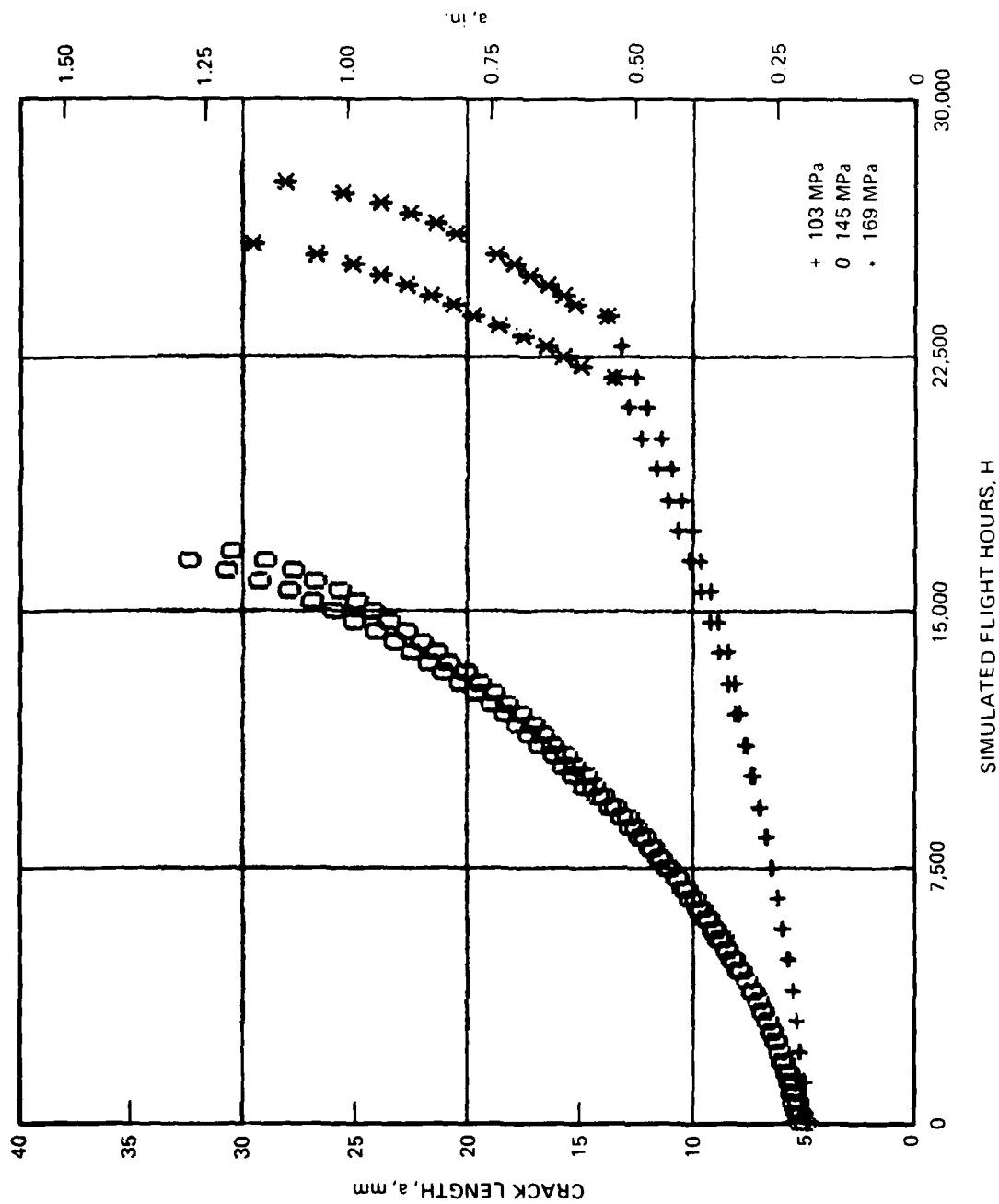
FIGURE B-12. 7475-T651, TC SPECTRUM
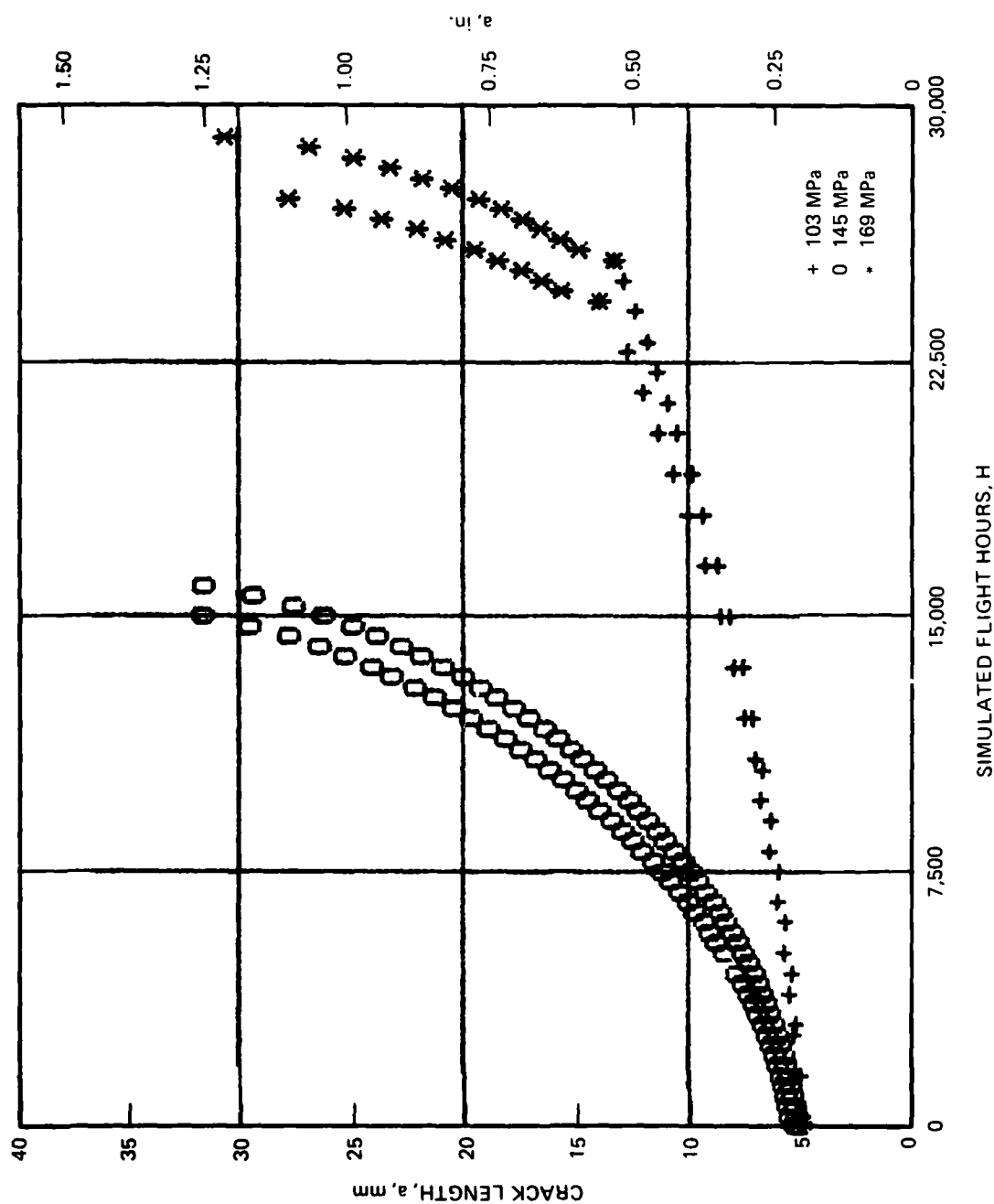
111
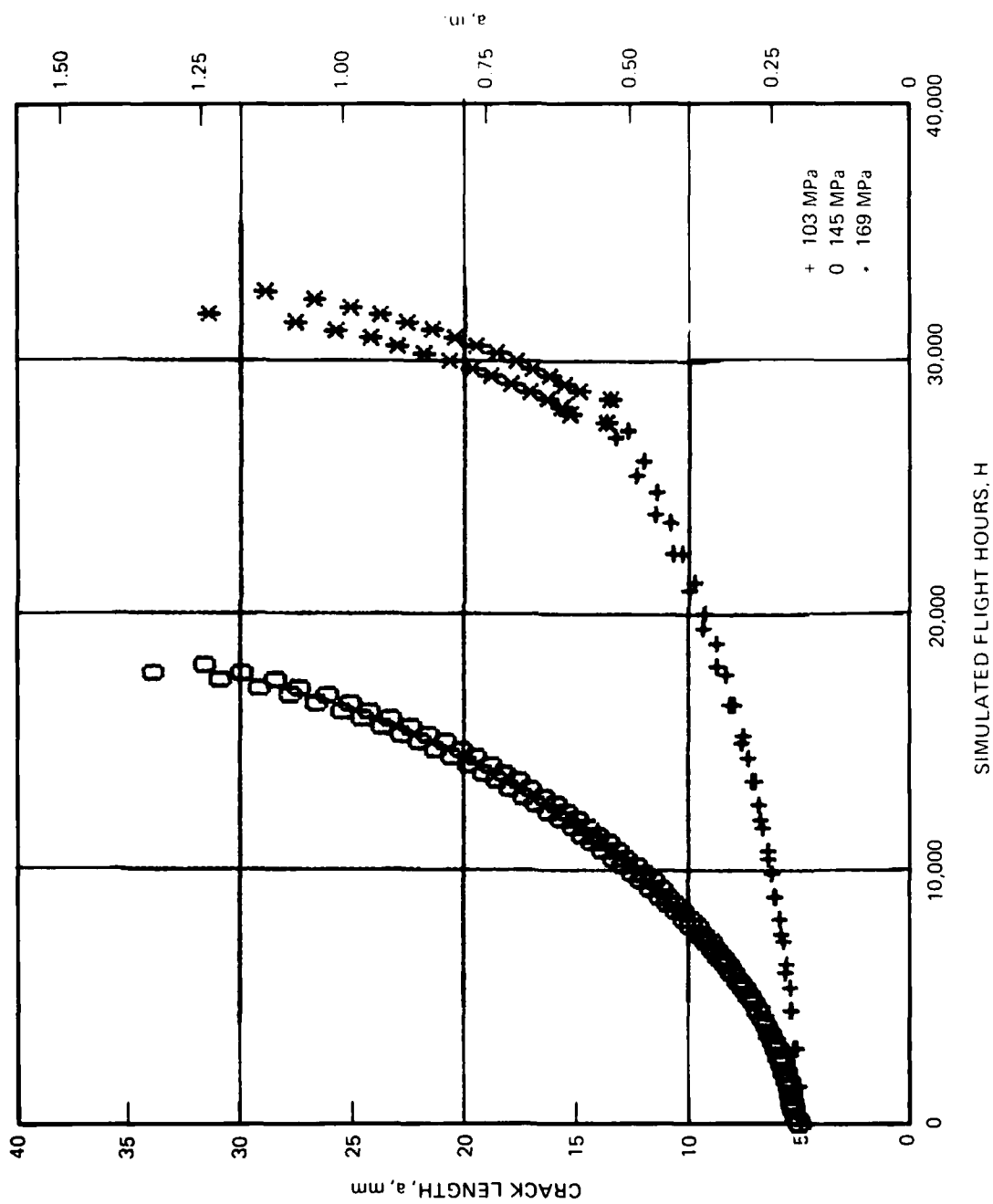
FIGURE B-13. 7475-T7351, TD SPECTRUM

112

FIGURE B-14. 7475-T7351, TC SPECTRUM

113

APPENDIX C

SPECTRUM CRACK GROWTH RATE VERSUS MAXIMUM PEAK STRESS INTENSITY, da/dH VERSUS K_{hmax}

1. The scales for both axes are identical on each graph.

2. There are two tests per maximum peak stress level and both are plotted with the same symbol.

3. Crack growth rates are calculated by two-point secant method per ASTM E647 based on the data in Appendix B, and applying the ASTM E647 requirement that the minimum crack growth interval, a, be greater than or equal to 0.25 mm. This is performed using Northrop Support Services Laboratory computer program designated $FITPLT from data on files designated .DDN, created from crack length measurement versus pass raw data.

4. Almost all tests had a crack growth rate which initially decreased for a few data points after precracking or in the transition from 103 to 169 MPa, therefore, all data up to the first local minimum crack growth rate were not plotted.

5. In some cases the first several data points for the 145 MPa testing the FCOR's were lower than for the 103 MPa testings. As discussed in Section 3.6, this was found to probably be related to the precracking procedure and, therefore, these first few data points were not considered in presenting data in the text.

6. One test at 169 MPa for 2124-T851, TC spectrum, Figure C-6 exhibited unusual behavior, which could be due to an overload during testing. This test was ignored in the presentation of crack growth rate data in the text.
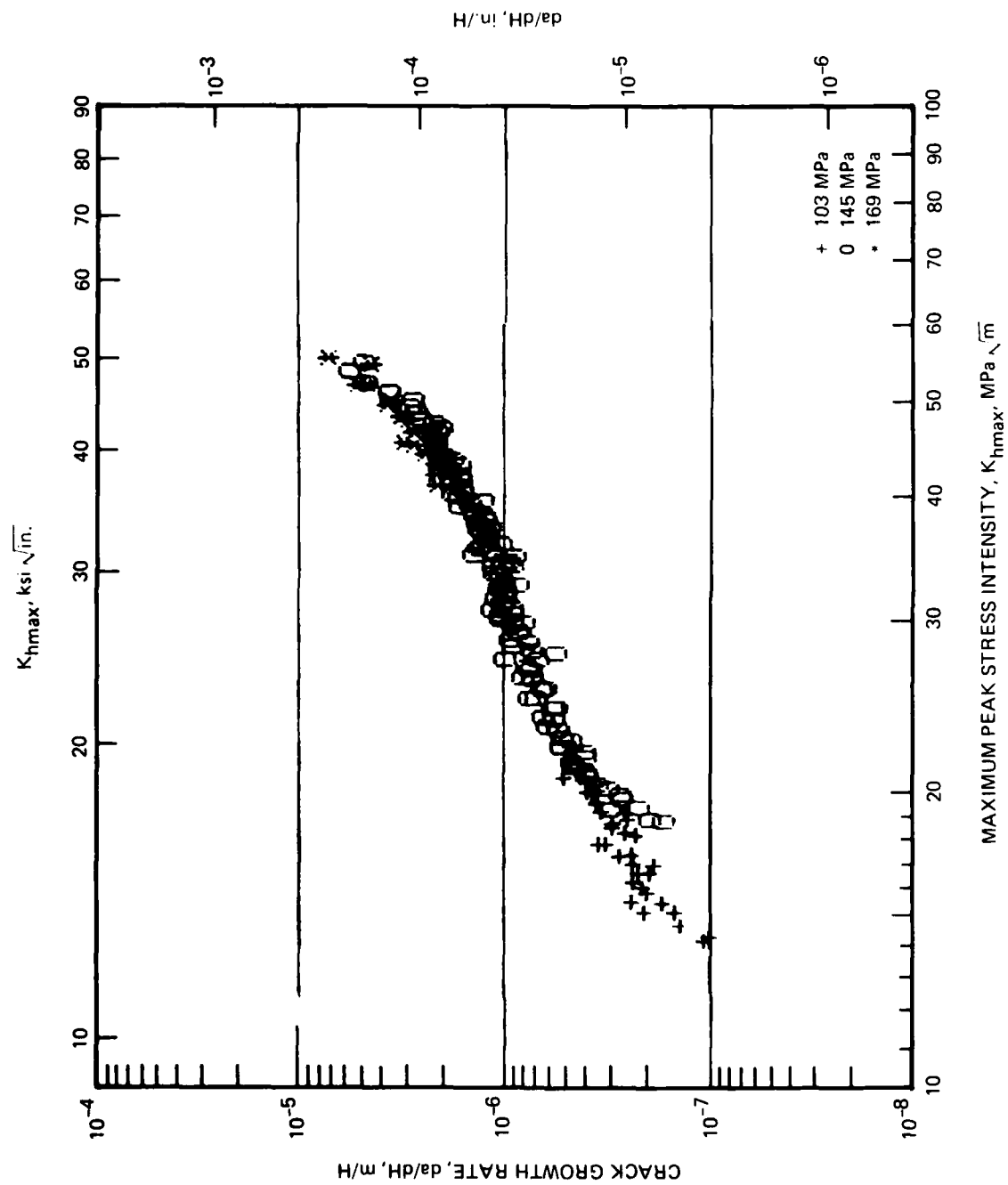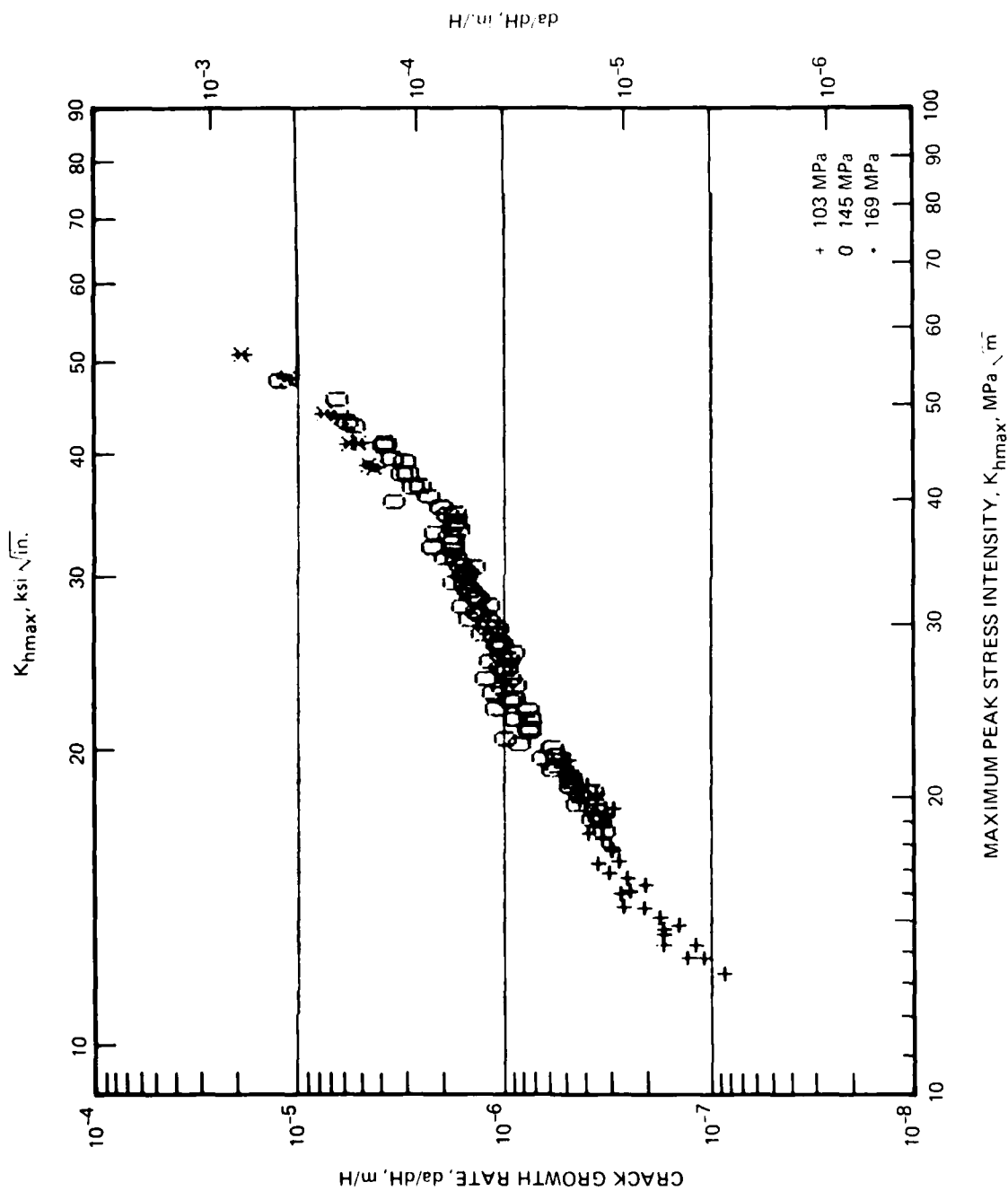
114

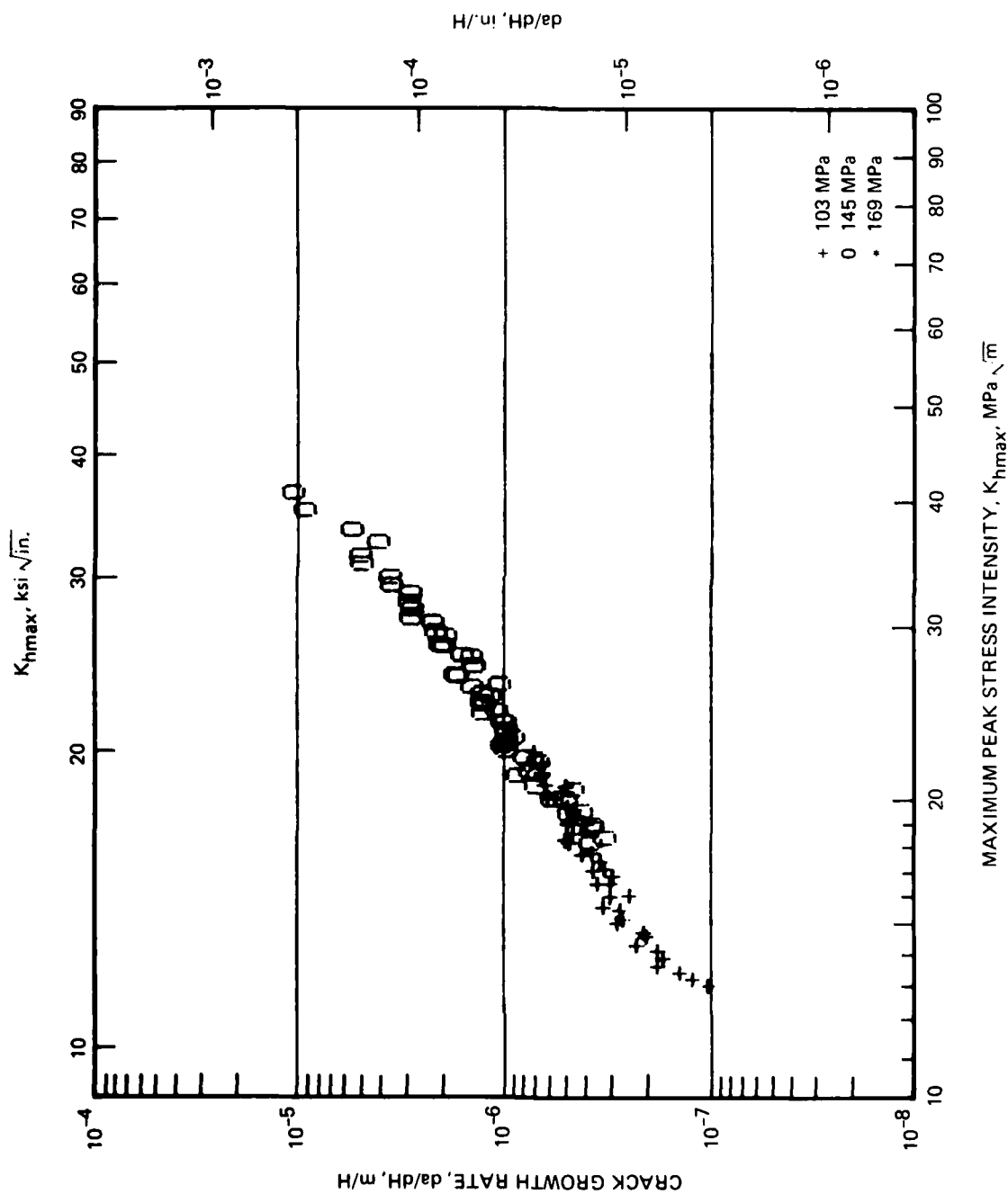FIGURE C-1. 2024-T351, TD SPECTRUM

FIGURE C-2. 2024-T351, TC SPECTRUM

116
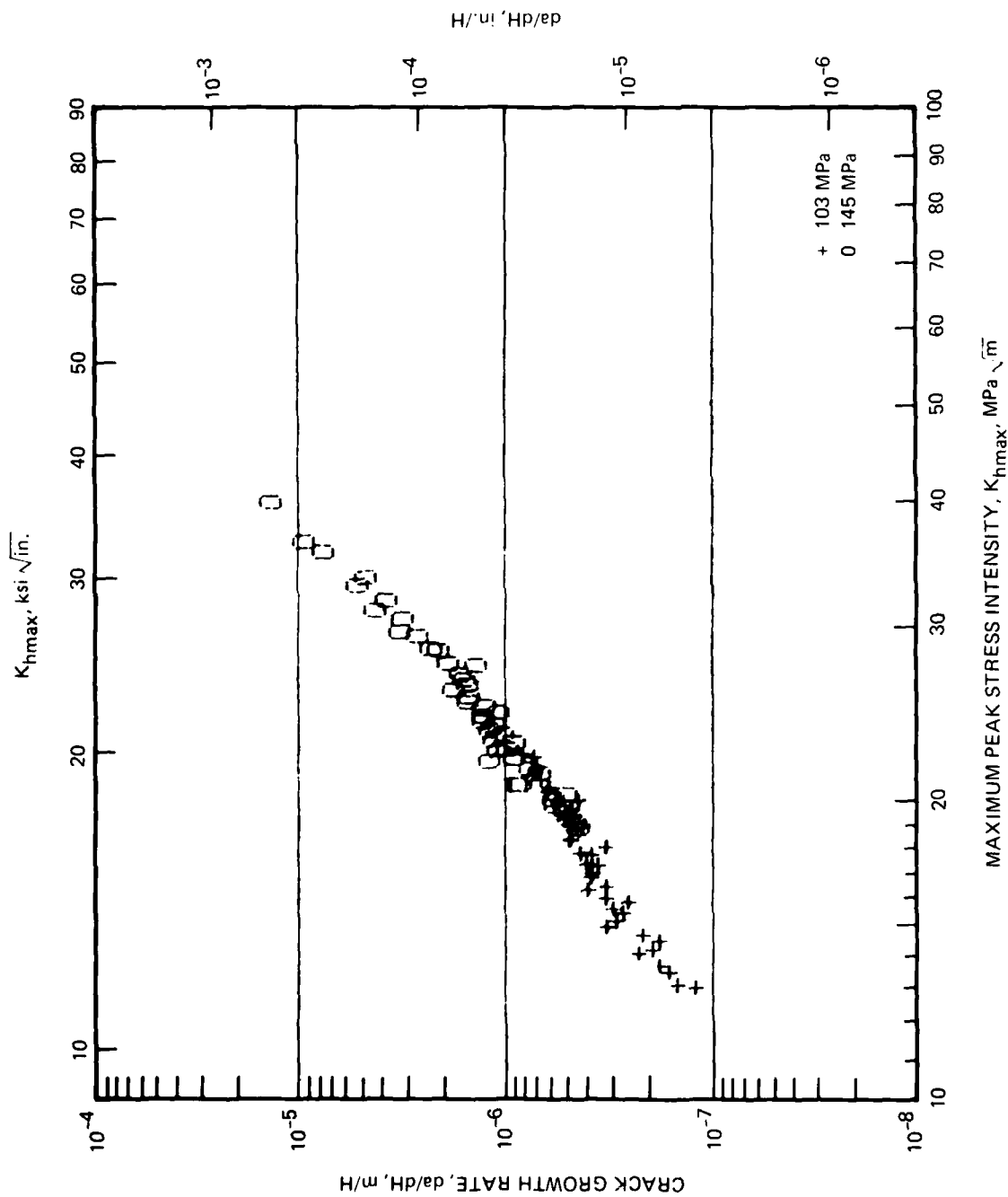
FIGURE C-3. 2024-T851, TD SPECTRUM

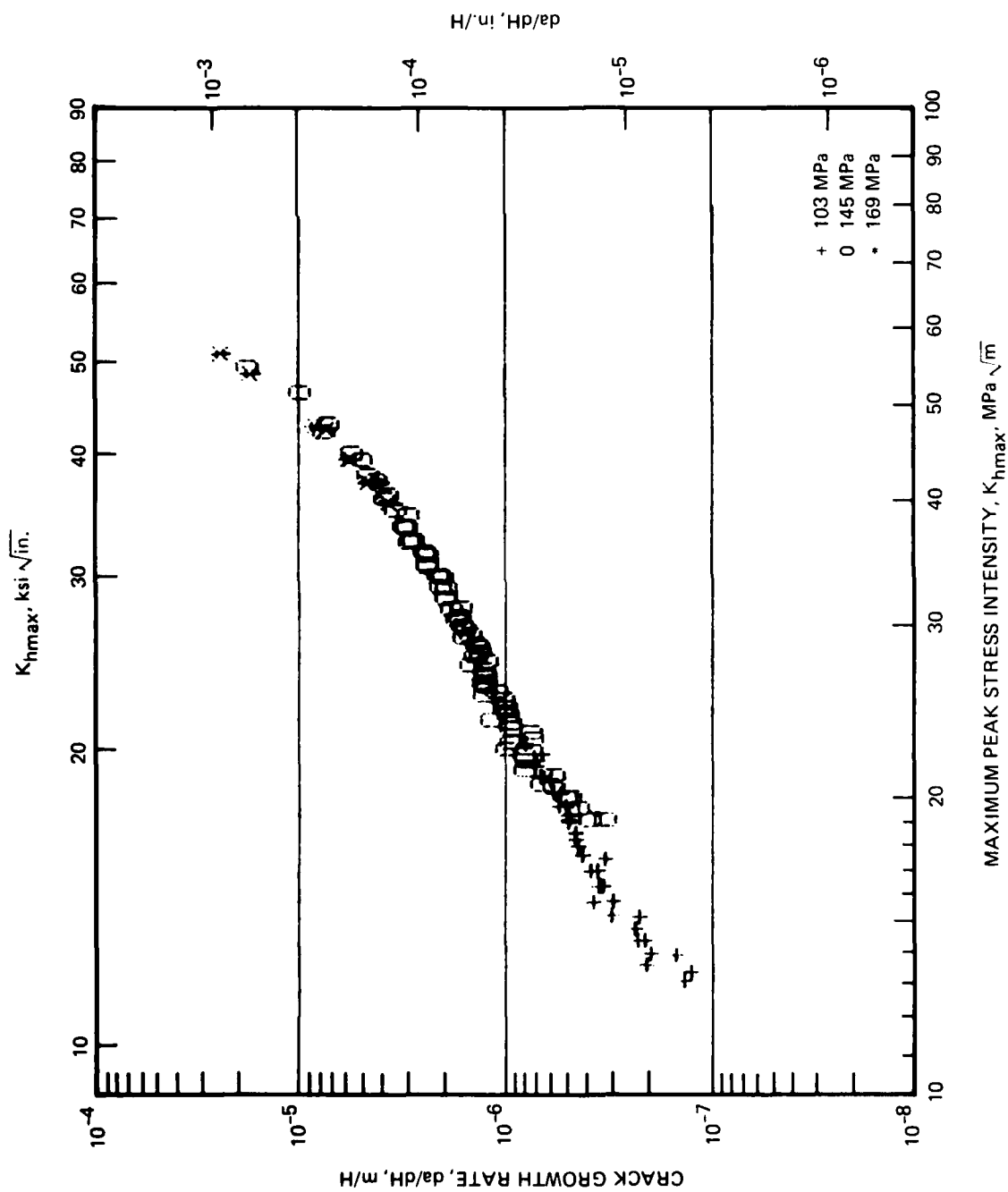FIGURE C-4. 2024-T851, TC SPECTRUM
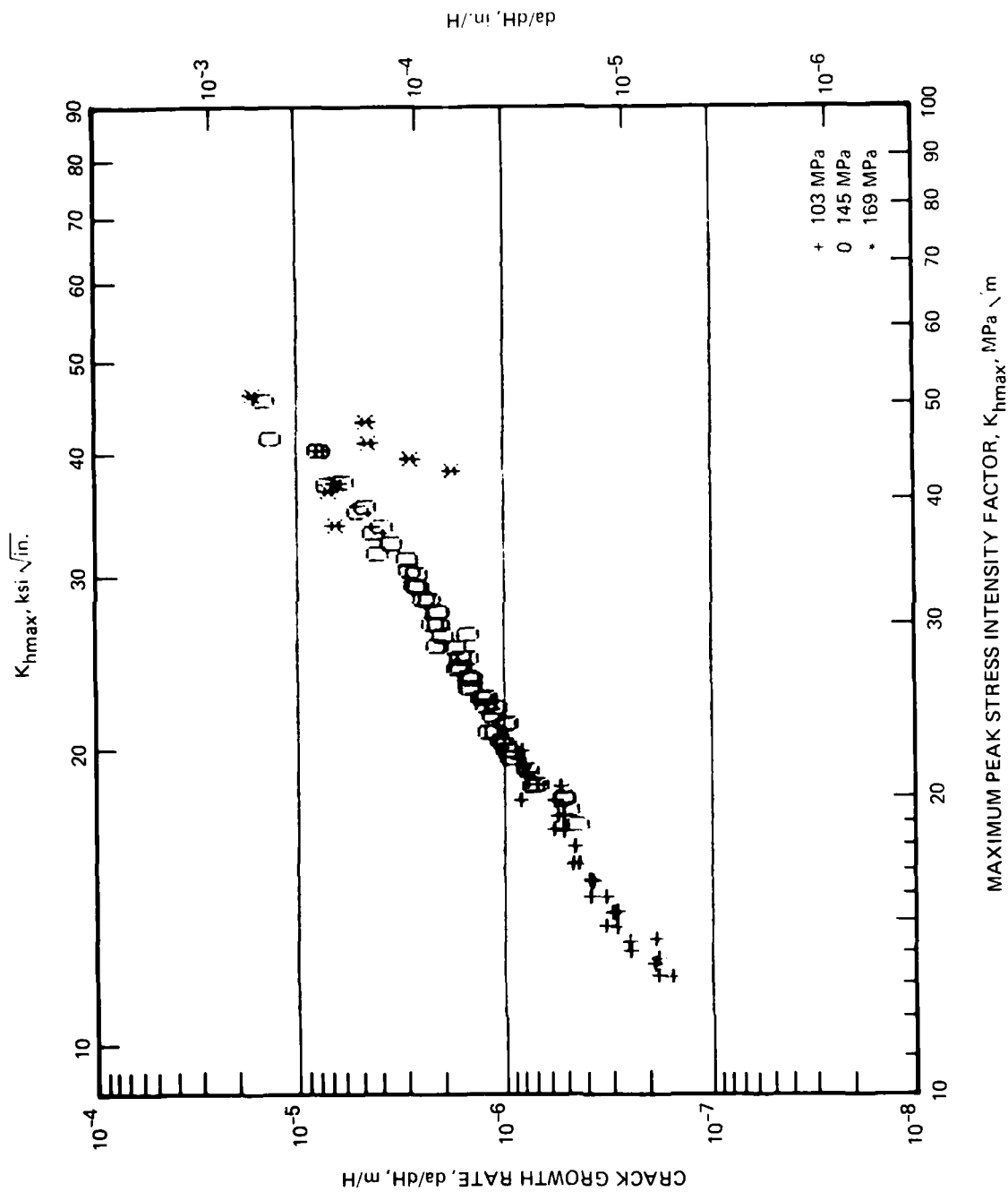
118

FIGURE C-5. 2124-T851, TD SPECTRUM
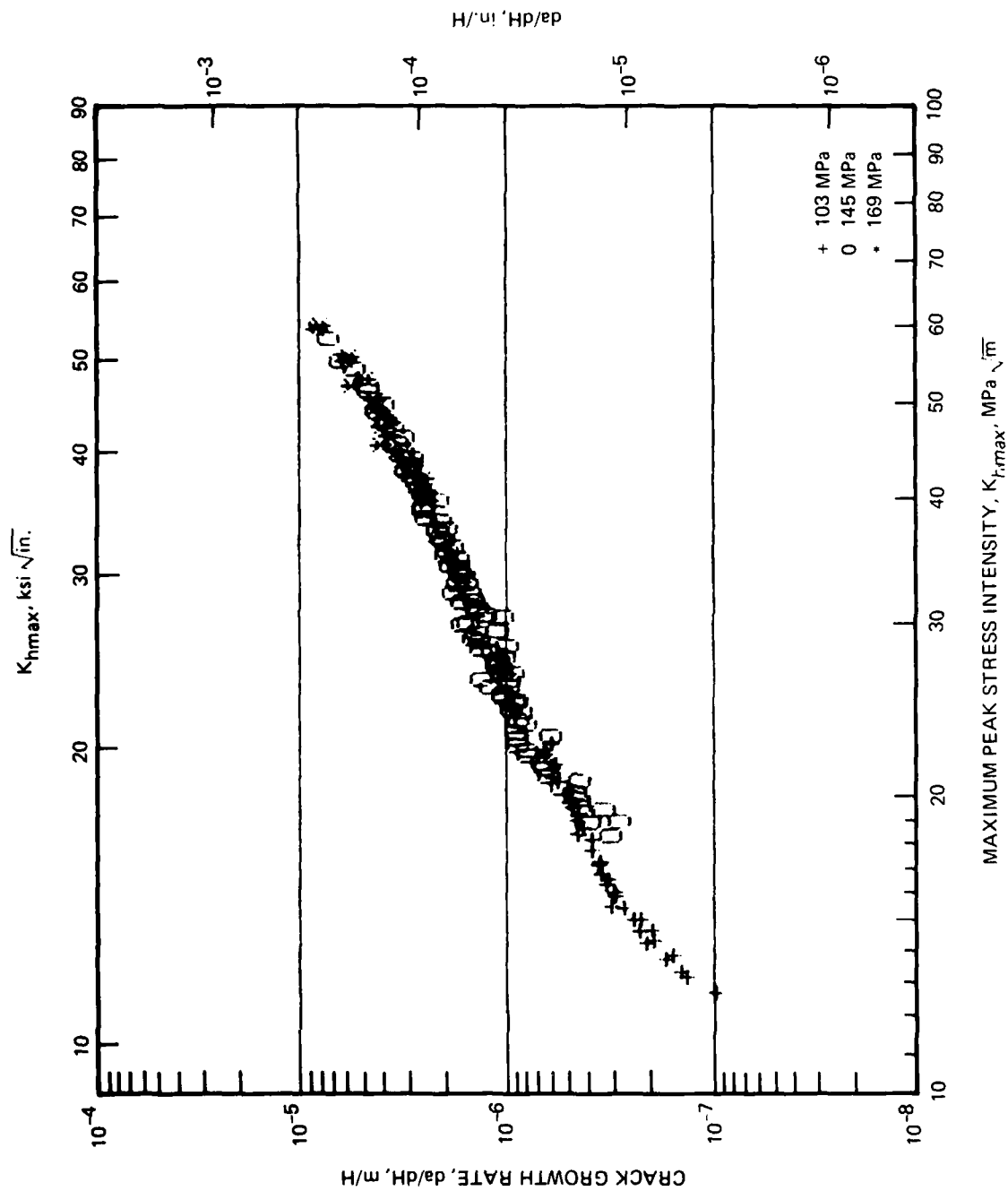
119

FIGURE C-6. 2124-T851, TC SPECTRUM
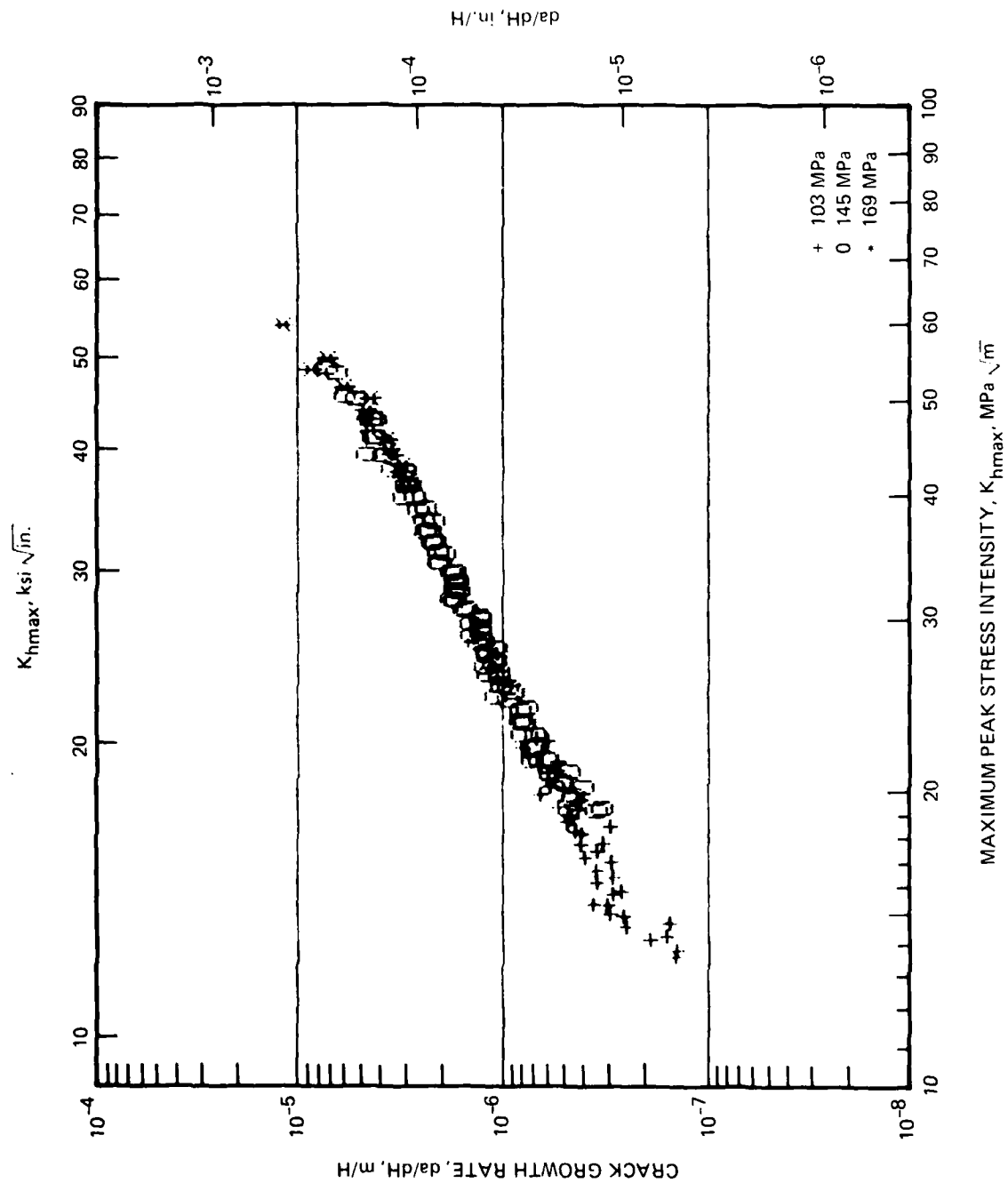
FIGURE C-7. 7050-T73651, TD SPECTRUM
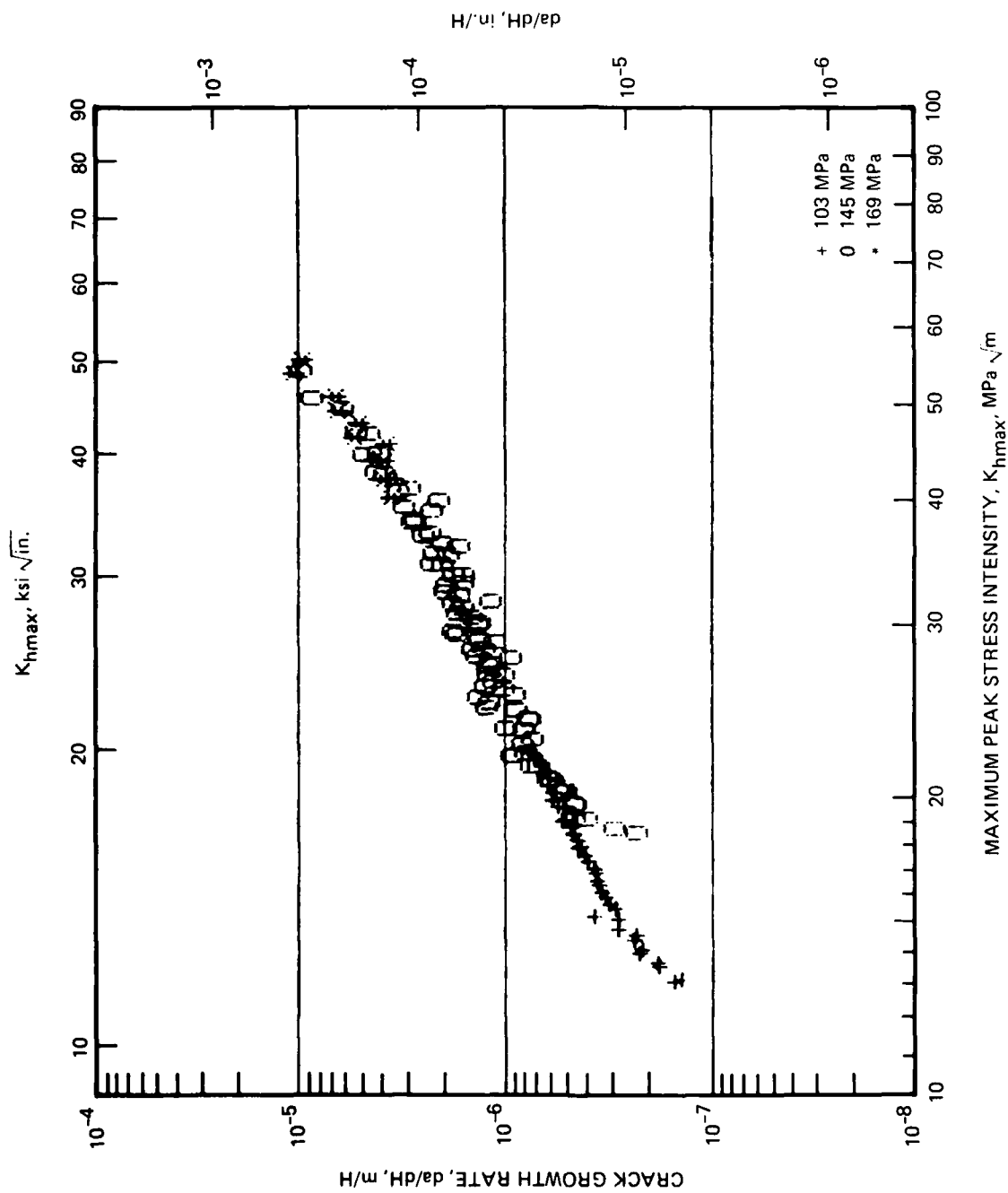
FIGURE C-8. 7050-T73651, TC SPECTRUM

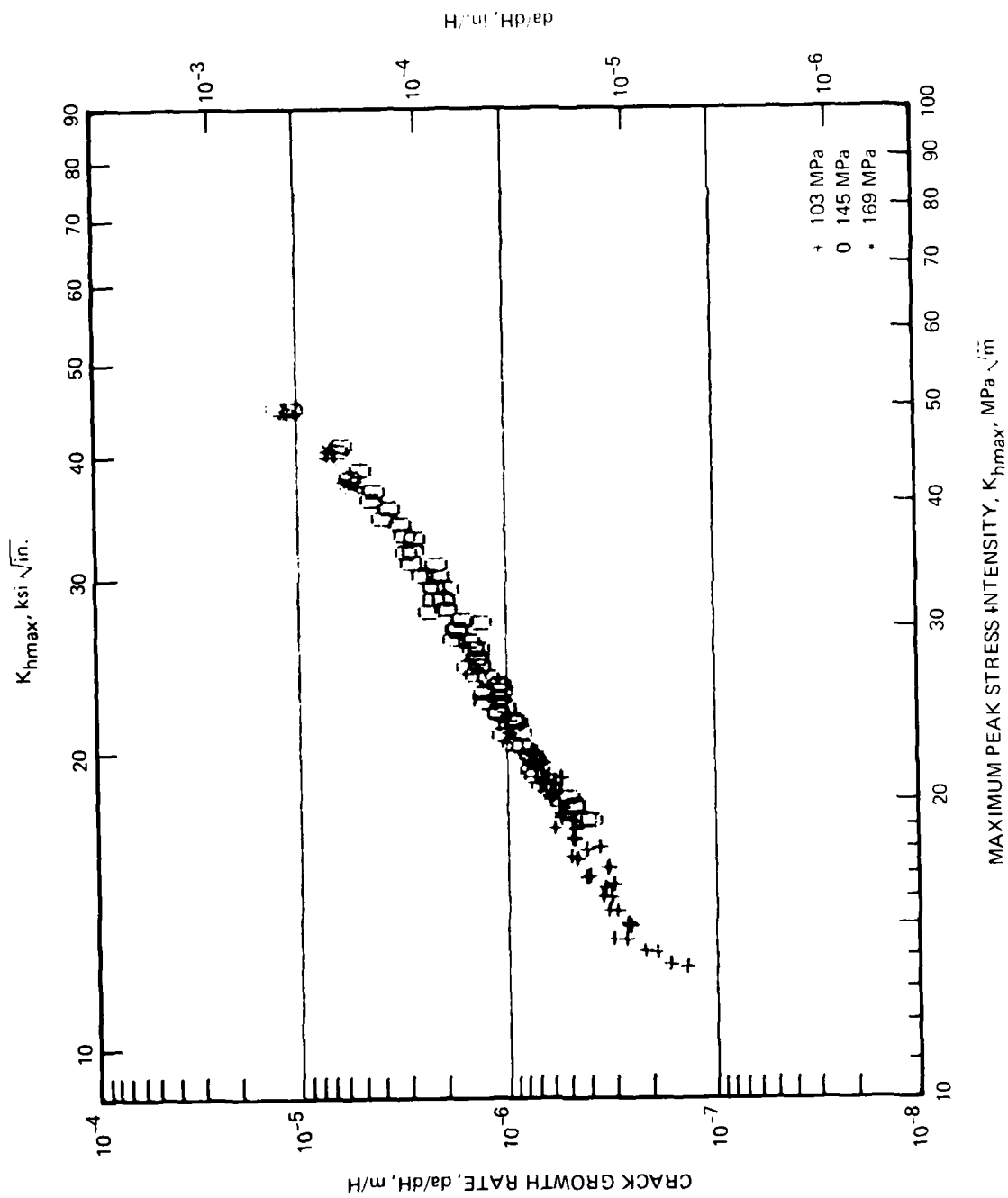FIGURE C-9. 7075-T7351, TD SPECTRUM
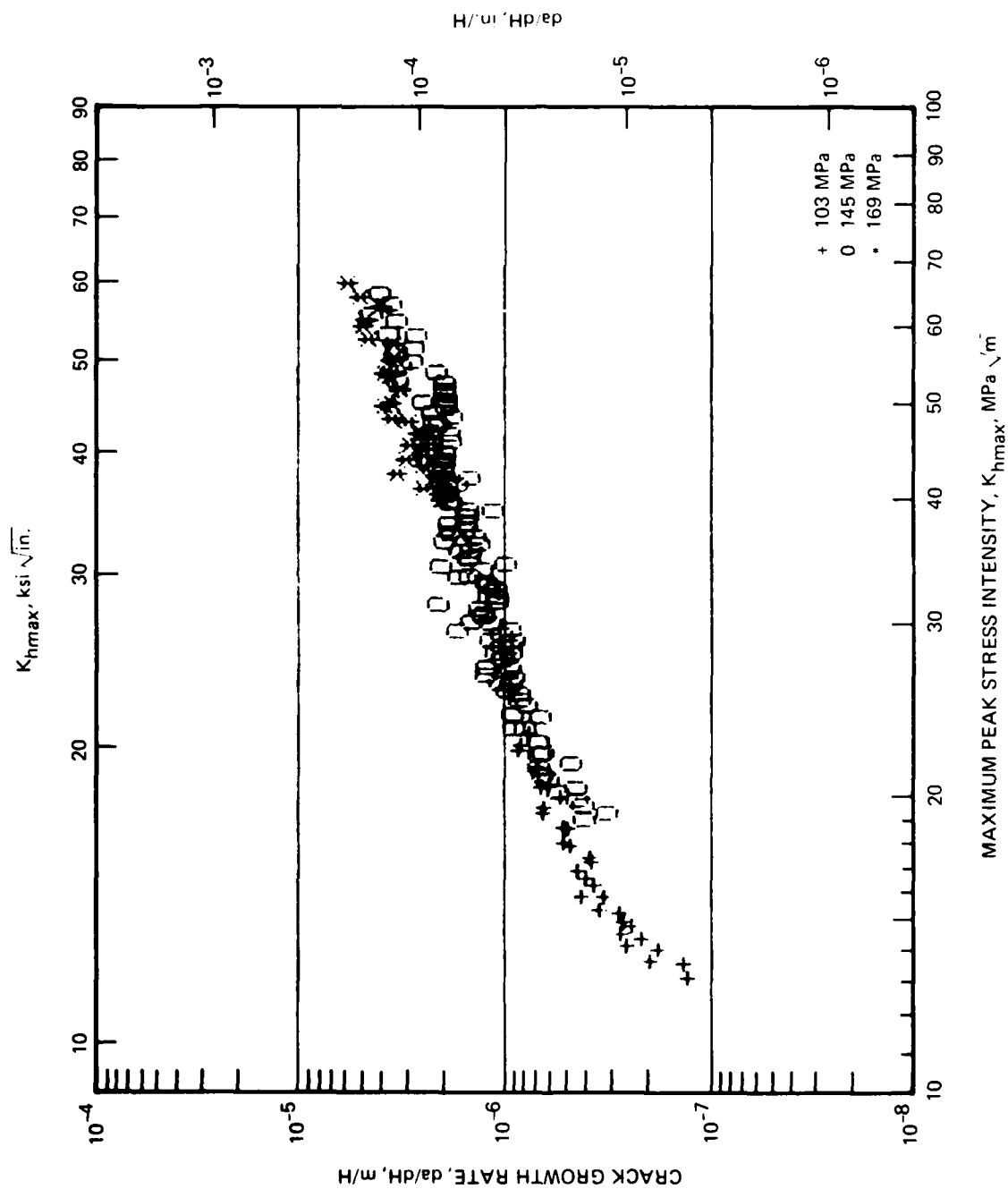
FIGURE C-10. 7075-T7351, TC SPECTRUM

124
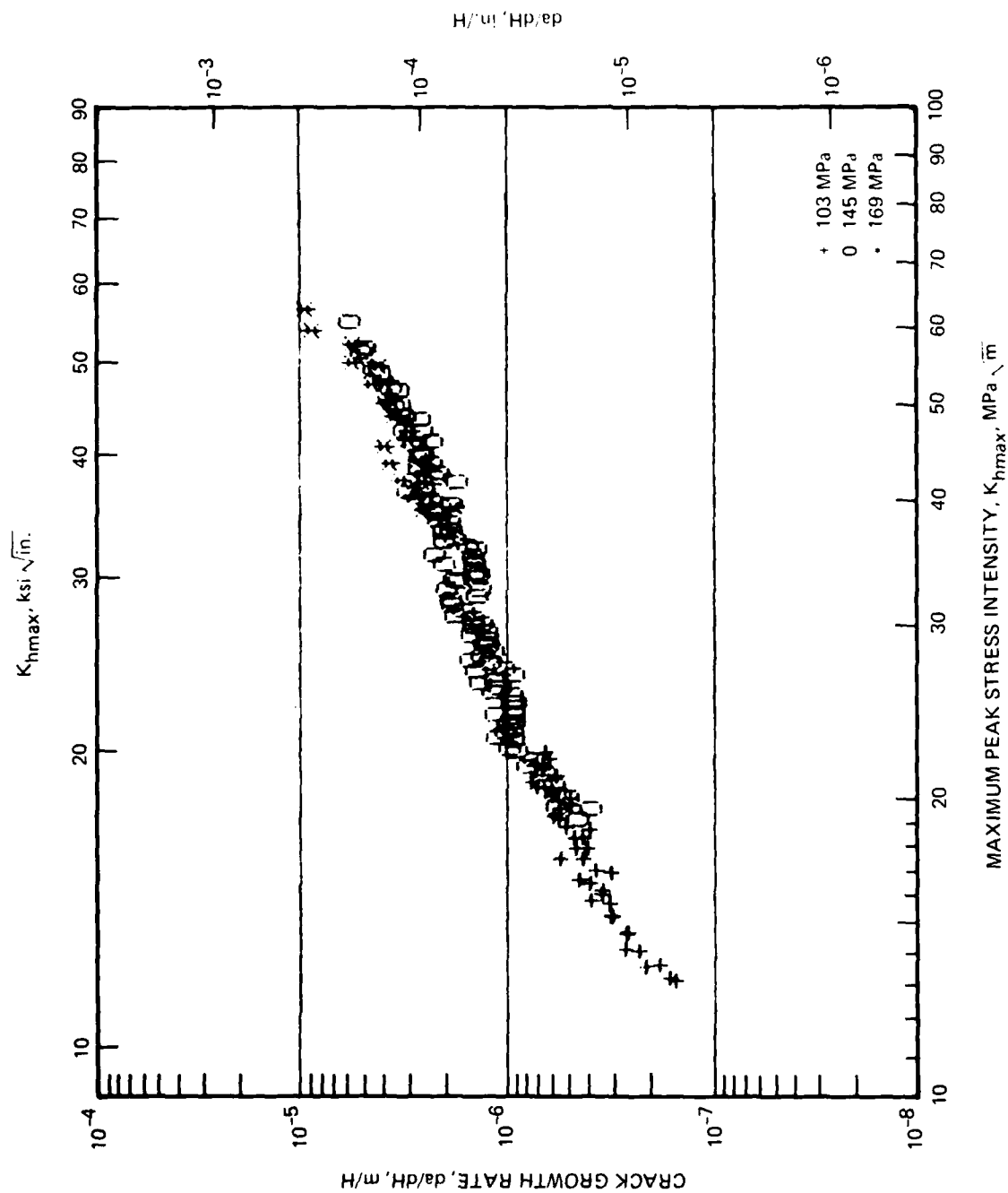
FIGURE C-11. 7475-T651, TD SPECTRUM
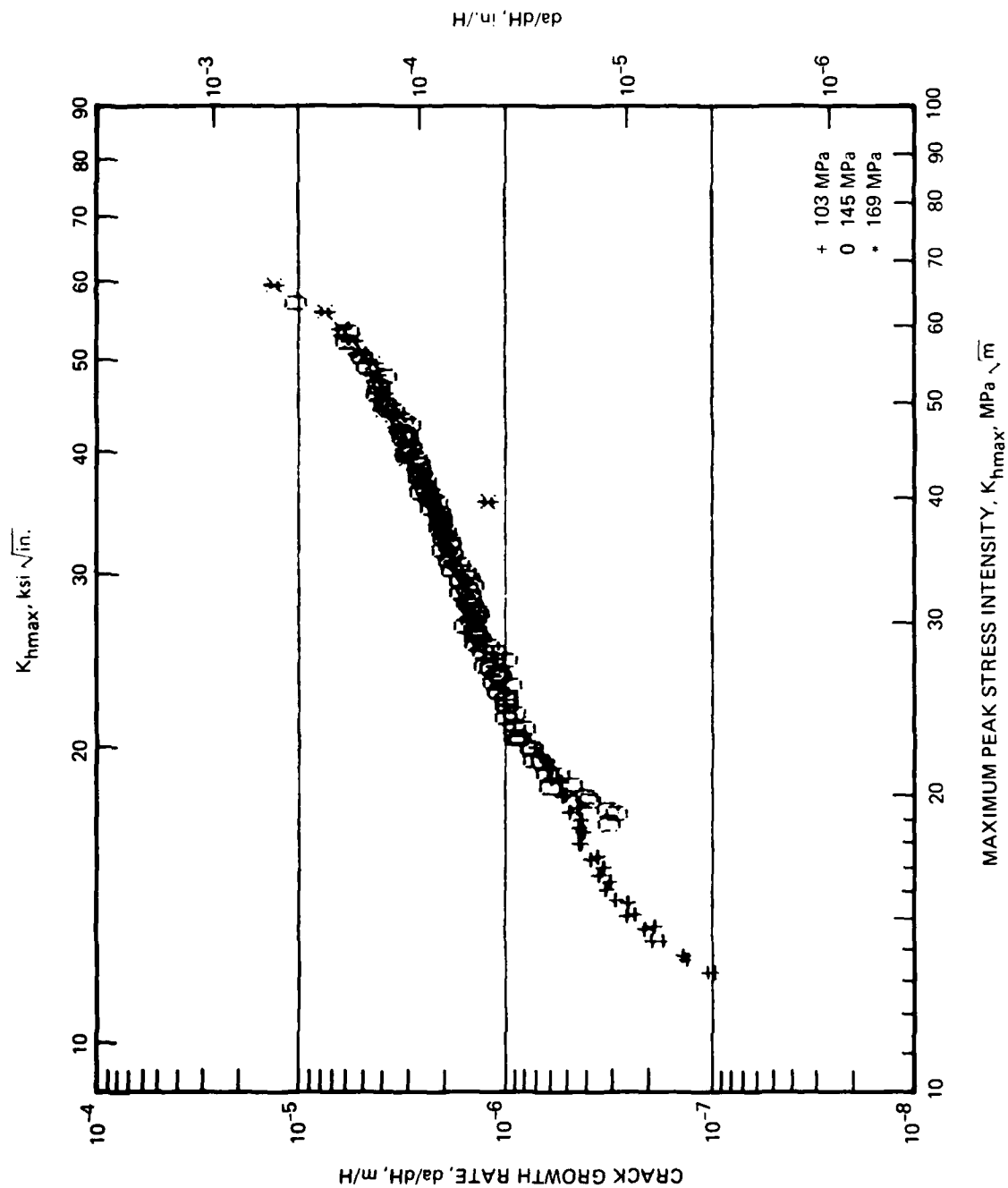
125

FIGURE C-12. 7475-T651, TC SPECTRUM
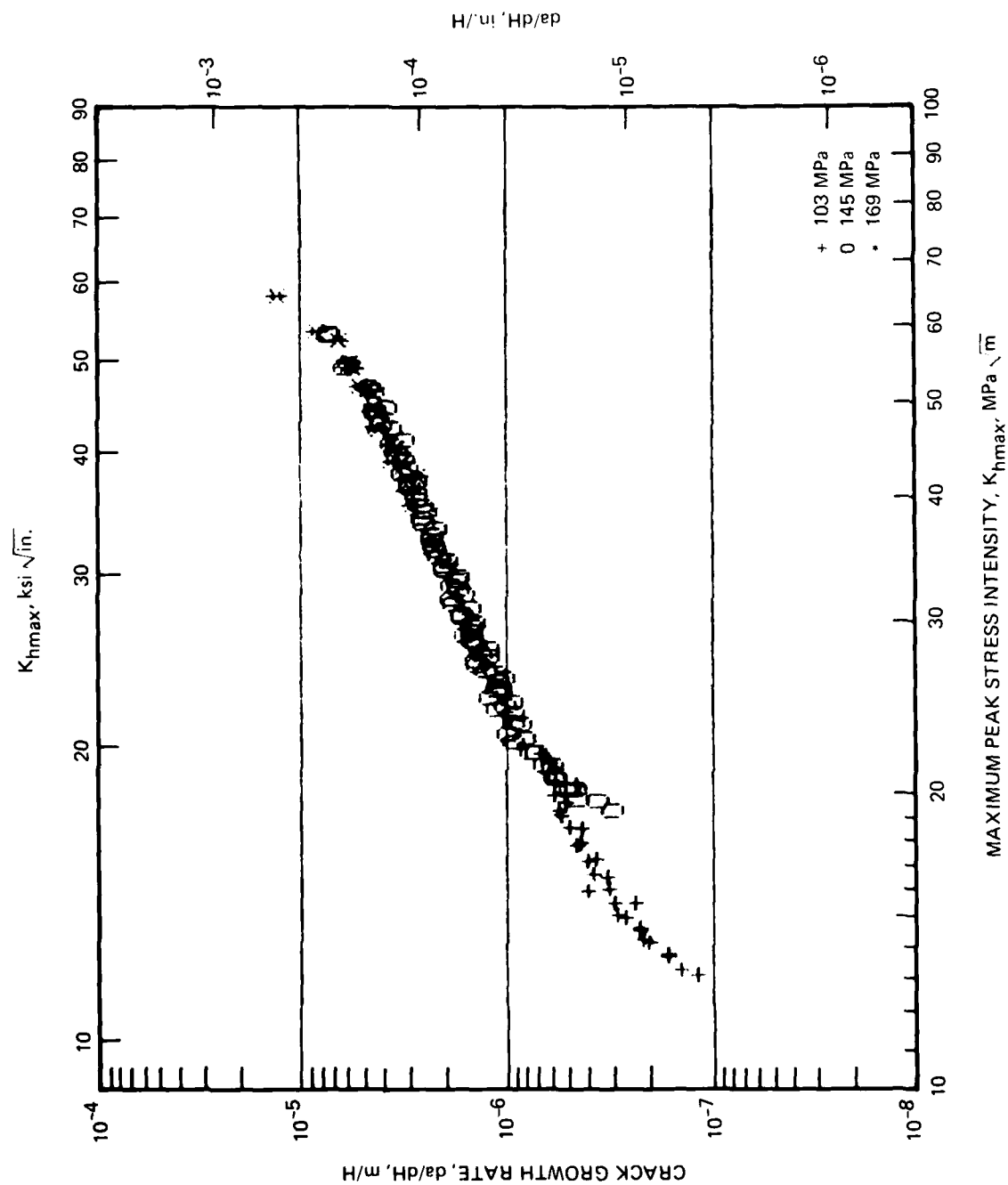
FIGURE C-13. 7475-T7351, TD SPECTRUM

127

FIGURE C-14. 7475-T7351, TC SPECTRUM

128

REFERENCES

1. G.R. Chanani, "Fundamental Investigation of Fatigue Crack Growth Retardation in Aluminum Alloys," AFML-TR-76-156, 1976.

2. T.H. Sanders, R.R. Sawtell, J.T. Staley, R.J. Bucci, A.B. Thakker, "The Effect of Microstructure on Fatigue Crack Growth of 7XXX Aluminum Alloys Under Constant Amplitude and Spectrum Loading," NADC Contract No. N00019-76-C-0482, 1978.

3. R.J. Bucci, A.B. Thakker, T.H. Sanders, R.R. Sawtell, J.T. Staley, "Ranking 7XXX Aluminum Alloy Fatigue Crack Growth Resistance Under Constant Amplitude and Spectrum Loading," ASTM STP 714, 1980.

4. R.J. Bucci, "Spectrum Loading — A Useful Tool to Screen Effects of Microstructure on Fatigue Crack Growth Resistance," ASTM STP 631, 1977.

5. O. Jonas and R.P. Wei, "An Exploratory Study of Delay in Fatigue-Crack Growth," Int. J. of Fracture Mechanics, Vol. 7, p. 116, 1971.

6. J. Schijve, "Effect of Load Sequences on Crack Propagation Under Random and Program Loading," Eng. Frac. Mech., Vol. 5, p. 269, 1973.

7. R.I. Stephens, D.K. Chen and B.W. Hom, "Fatigue Crack Growth With Negative Stress Ratio Following Single Overloads in 2024-T3 and 7075-T6 Aluminum Alloys," ASTM STP 595, 1976.

8. W.X. Alzos, A.C. Skat, Jr., and B.M. Hillberry, "Effect of Single Overload/Underload Cycles on Fatigue Crack Propagation," ASTM STP 595, 1976.

9. G.R. Chanani, "Effect of Thickness on Retardation Behavior of 7075 and 2024 Aluminum Alloys," ASTM STP 631, 1977.

10. G.R. Chanani, "Investigation of Effects of Saltwater on Retardation Behavior of Aluminum Alloys," ASTM STP 642, 1977.

11. J. Schive, "Observations on the Prediction of Fatigue Crack Growth Propagation Under Variable-Amplitude Loading," ASTM STP 595, 1976.

12. R.J.H. Wanhill, "Maneuver Spectrum Fatigue Crack Propagation in Aluminum Alloy Sheet Materials," NLR-TR-78091-U, May 1980.

13. H.D. Dill, C.R. Saff and J.M. Potter, "Effects of Fighter Attack Spectrum on Crack Growth," ASTM STP 714, 1980.

14. P.R. Abelkis, "Effect of Transport Aircraft Wing Loads Spectrum Variation on Crack Growth," ASTM STP 714, 1980.

15. J.T. Staley, "Microstructure and Toughness of High Strength Aluminum Alloys," ASTM STP 605, 1976.

16. W.G. Truckner, J.T. Staley, R.J. Bucci, and A.B. Thakker, "Effects of Microstructure on Fatigue Crack Growth of High Strength Aluminum Alloys," AFML-TR-76-169, 1976.

17. J.T. Staley, W.G. Truckner, R.J. Bucci, and A.B. Thakker, "Improving Fatigue Resistance of Aluminum Aircraft Alloys," Aluminum 11, 53, 1977.

18. T.H. Sanders, Jr., and J.T. Staley, "Review of Fatigue and Fracture Research on High-Strength Aluminum Alloys," Fatigue and Microstructure, Metals Park: American Society for Metals, 1979.

19. P.E. Bretz, A.K. Vasudevan, R.J. Bucci, and R.C. Malcolm, "Effect of Microstructure on 7XXX Aluminum Alloy Fatigue Crack Growth Behavior Down to Near-Threshold Rates, Final Report, Naval Air Systems Command, Contract N00019-79-C-0258, 1981.

20. J. Willenborg, R.M. Engle, and H.A. Wood, "A Crack Growth Retardation Model Using an Effective Stress Concept," TM-71-1-FBR, WPAFB, Ohio, 1971.

21. O.E. Wheeler, "Crack Growth Under Spectrum Leading," J. of Basic Eng. Trans. ASME, p. 181, March 1972.

22. W. Elber, "The Significance of Fatigue Crack Closure," ASTM STP 486, 1971.

23. H.D. Dill, C.R. Saff, "Effects of Fighter Attack Spectrum on Crack Growth," AFFDL-TR-76-112, March 1977.

24. G.R. Chanani and B.J. Mays, "Observation of Crack-Closure Behavior After Single Overload Cycles in 7075-T6 SEN Specimens," Eng. Fract. Mech., Vol. 9, p. 65, 1977.

25. G.R. Chanani, "Determination of Plastic-Zone Sites at Fatigue Cracks by Optical Interference Technique," Int. J. of Fracture, Vol. 13, p. 394, 1977.

26. R.L. Jones and T.E. Cagle, "The Mechanical Stress-Corrosion, Fracture Mechanics, and Fatigue Properties of 7050, 7475, and Ti-8 Mo-8V-2Fe-3Al Plate and Sheet Alloys," Report FGT-5791, General Dynamices, 1976.

27. A. Saxena, S.J. Hudak, Jr., J.K. Donald, D.W. Schmidt, "Computer Controlled K-Decreasing Test Technique for Low Rate Fatigue Crack Growth Testing," JETVA, Vol. 6, 1978.

28. R.J. Bucci, "Development of a Proposed Standard Practice for Near-Threshold Fatigue Crack Growth Rate Measurements," ASTM STP 738, 1981.

29. E.J. Coyne, Jr., and E.A. Starke, Jr., "The Effect of Microstructure on Fatigue Crack Growth Behavior of an Al-Zn-Mg-(Zr) Alloy," Int. J. of Fracture, Vol. 15, p. 405, 1979.

30. J.F. Knott and A.C. Pickard, "Effects of Overloads on Fatigue Crack Propagation: Aluminum Alloys," Metal Science, p. 399, 1979.

31. C.Y. Kung and M.E. Fine, "Fatigue Crack Initiation and Microcrack Growth in 2024-T4 and 2124-T4 Aluminum Alloys," Met. Trans. A, Vol. 10, p. 603, 1979.

DISTRIBUTION LIST

(One copy unless otherwise noted)

Mr. M. Valentine
AIR-5304B4
Naval Air Systems Command
Washington, DC 20361
(10 copies + balance after distribution)

Commander
Naval Air Development Center
(Code 302)
Warminster, PA 18974

Naval Sea Systems Command
(Code 03423)
Department of the Navy
Washington, DC 20360

Navy Ships Research &
Development Center
(Code 2812)
Annapolis, MD 21402

Commander Naval Surface/Weapons Center
(Metallurgy Division)
White Oak
Silver Spring, MD 20910

Director, Naval Research Laboratory
(Codes: 6380, 6490, 6601, 8430) - 1 each
Washington, DC 20390

Office of Naval Research
The Metallurgy Program, Code 471
Arlington, VA 22217

Dr. T.R. McNelley
Dept. of Mechanical Engineering
(Code 59)
Naval Postgraduate School
Monterey, CA 93940

14 copies (12 copies for DDC, 2 copies
for AIR-954)
Commander, Naval Air Systems Command
AIR-954
Washington, DC 20361

Wright-Patterson Air Force Base
Ohio 45433
Attn: W. Griffith, AFML/LLS

Wright-Patterson Air Force Base
Ohio 45433
Attn: C.L. Harmsworth, AFML/MXE

Army Materials & Mechanics
 Research Center
Watertown, MA 02172
Attn: Dr. A. Gorum

A.P. Divecha, R32
Naval Surface Weapons Center
White Oak, Laboratory
Silver Spring, Maryland 20910

Richard Schmidt, Code 320A
Naval Air Systems Command
Washington, D.C., 20361
(2 copies)

Naval Surface Weapons Center
Library - X211
White Oak, Silver Spring, MD
20910

Commanding Officer
Office of Ordnance Research
Box CM, Duke Station
Durham, North Carolina 27706

U.S. Army Armament R&D Command
(ARRADCOM)
Dover, NJ 07801
Attn: Dr. J. Waldman
        DRDAR-SCM-P, Bldg. 3409

National Aeronautics & Space
 Administration
(Code RWM)
600 Independence Ave., S.W.
Washington, D.C. 20546

National Aeronautics and Space
  Administration
Langley Research Center
Materials Division, Langley Station
Hampton, Virginia 23365
Attn: Mr. H.F. Hardrath
        Stop 188M

National Aeronautics & Space
  Administration
George C. Marshall Space Flight Center
Huntsville, Alabama 35812
Attn: Mr. J.G. Williamson
        S&E-ASTN-MMC

National Academy of Science
Materials Advisory Board
Washington, D.C. 20418
Attn: Dr. J. Lane

Director
National Bureau of Standards
Washington, D.C. 20234
Attn: Dr. E. Passaglia

Battelle Memorial Institute
505 King Avenue
Columbus, OH 43201
Attn: Mr. Stephan A. Rubin, Mgr.
        Information Operations

IIT Research Institute
Metals Research Department
10 West 35th Street
Chicago, Illinois 60616
Attn: Dr. N. Parikh

Aluminum Company of America
1200 Ring Bldg.
Washington, D.C. 20036
Attn: Mr. G.B. Barthold

Aluminum Company of America
Alcoa Center, PA 15069
Attn: Mr. Paul L. Mehr

General Dynamics Convair Div.
P.O. Box 80847
San Diego, CA 92138
Attn: Mr. Jack Christian, Code 643-10

Kaman Aerospace Corporation
Old Windsor Road
Bloomfield, Connecticut 06001
Attn: Mr. M.L. White

Rockwell International
Columbus Division
Columbus, OH 43216
Attn: Mr. P. Maynard, Dept. 75
        Group 521

Rockwell International
Rocketdyne Division
Canoga Park, CA 91305
Attn: Dr. Al Jacobs
            Group Scientist
            Materials Branch

Rockwell International
Los Angeles Division
International Airport
Los Angeles, CA 90009
Attn: Gary Keller
            Materials Applications

Lockheed Palo Alto Research
  Laboratories
Materials Science Laboratory
3251 Hanover Street
Palo Alto, CA 94303
Attn: Dr. Frank A. Crossley
        52-31/204

Lockheed California Company
P.O. Box 551
Burbank, CA 91503
Attn: Mr. J.M. VanOrden
        Dept. 74-71, Bldg. 221,
        Plt. 2

Lockheed-Georgia Company
Marietta, Georgia 30061
Attn: E. Bateh

Lockheed Missile & Space
  Corporation
Box 504
Sunnyvale, CA 94088
Attn: Mr. G.P. Pinkerton
        Bldg. 154, Dept. 8122
        Mr. C.D. McIntyre
        Bldg. 132, Dept. 84-13
        (1 each)

Douglas Aircraft Company
3855 Lakewood Blvd.
Long Beach, CA 90808
Attn: Mr. Fred Mehe, C1-250

Sikorsky Aircraft
Division of United Aircraft Corp.
Stratford, Connecticut 06497
Attn: Materials Dept.

Boeing-Vertol Company
Boeing Center
P.O. Box 16858
Philadelphia, PA 19142
Attn: Mr. J.M. Clark

The Boeing Company
Commerical Airplane
ORG. 6-8733, MS77-18
P.O. Box 3707
Seattle, Washington 98124
Attn: Cecil E. Parsons

Northrop Corporation
Aircraft Division
One Northrop Avenue
Hawthorne, CA 90250
Attn: Mr. Allan Freedman
      Dept. 3871/62

Vought Corp.
P.O. Box 5907
Dallas, Texas 75222
Attn: Mr. A. Hohman

McDonnell Aircraft Company
St. Louis, Missouri 63166
Attn: Mr. H.J. Siegel
      Materials & Processes Div.
      General Engineering Division

Lycoming Division
AVCO Corporation
550 S. Main Street
Stratford, Connecticut 06497
Attn: Mr. Barry Goldblatt

Detroit Diesel Allison Division
General Motors Corporation
Materials Laboratories
Indianapolis, Indiana 46206

AiResearch Manufacturing Co.
  of America
Sky Harbor Aircraft
402 S. 36th Street
Phoenix, Arizona 85034
Attn: Mr. Jack D. Tree,
      Dept. 93-35-5M

General Electric Company
Aircraft Engine Group
Materials & Processes Technology
  Laboratories
Evendale, OH 45315

Solar
2200 Pacific Highway
San Diego, CA 92112
Attn: Dr. A.G. Metcalfe

Teledyne CAE
1330 Laskey Road
Toledo, OH 43601

Dr. Charles Gilmore
Tompkins Hall
George Washington University
Washington, D.C. 20006

General Electric Company
Corporate Research & Development
P.O. Box 8
Schenectady, New York 12301
Attn: Dr. D. Wood

Westinghouse Electric Company
Materials & Processing Laboratories
Beulah Road
Pittsburgh, Pennyslvania 15235
Attn: Don E. Harrison

Dr. John D. Wood
Associate Professor
Lehigh University
Bethlehem, Pennyslvania 18015

General Dynamics Corp.
Convair Aerospace Division
Fort Worth Operation
P.O. Box 748
Fort Worth, Texas 76101
Attn: Tom Coyle
      E. Balmuth

Dr. A.I. Mlavsky
Senior Vice President for Technology
   and Director of Corporate Technology
   Center
Tyco Laboratories, Inc.
16 Hickory Drive
Waltham, Massachusetts 02145

Martin Marietta Aluminum
Attn: Mr. Paul E. Anderson
         (M/C 5401)
19200 South Western Avenue
Torrance, CA 90509

Dr. Howard Bomberger
Reactive Metals, Inc.
Niles, OH 44446

Mr. W. Spurr
The Boeing Company
12842 72nd Ave., N.E.
Kirkland, Washington 98033

Dr. John A. Schey
Department of Materials Engineering
University of Illinois at Chicago Circle
Box 4348
Chicago, Illinois 60680

Rockwell International
P.O. Box 1082
1027 Camino Dos Rios
Thousand Oaks, California 91320

Pratt & Whitney Aircraft
Division of United Technologies
Florida Research and Development Center
P.O. Box 2691
West Palm Beach, Florida 33402

P.R. Mallory & Company, Inc.
3029 East Washington Street
Indianapolis, Indiana 46206
Attn: Technical Librarian

Martin Marietta Corporation
P.O. Box 5837
Orlando, Florida 32805
Attn: Dr. Richard C. Hall
         Mail Point 275

Southwest Research Institute
8500 Culebra Road
P.O. Box 28510
San Antonio, Texas 78284
Attn: Dr. C. Gerald Gardner

Avco Space Systems Division
Lowell Industrial Park
Lowell, Massachusetts 01851

Brush Wellman, Inc.
17876 St. Clair Avenue
Cleveland, Ohio 44110
Attn: Mr. Bryce King

General Electric
Missile & Space Division
Materials Science Section
P.O. Box 8555
Philadelphia, Pennsylvania 91901
Attn: Technical Library

Kawecki Berylco Industries
P.O. Box 1462
Reading, Pennsylvania 19603

Linde Company
Division of Union Carbide
P.O. Box 44
Tonawanda, New York 14152

Midwest Research Institute
425 Volker Boulevard
Kansas City, Missouri 64110

University of California
Lawrence Radiation Laboratory
P.O. Box 808
Livermore, CA 94550
Attn: Mr. L.W. Roberts

ERDA Division of Reactor Development
   and Technology
Washington, D.A. 20545
Attn: Mr. J.M. Simmons, Chief
         Metallurgy Section

Dr. W.C. Setzer, Director
Metallurgy & Surface Technology
Consolidated Aluminum Corp.
P.O. Box 14448
St. Louis, MO 63178

Kaiser Aluminum & Chemical Corp.
Aluminum Division Research Center
  for Technology
P.O. Box 870
Attn: T.R. Prichett
Pleasanton, CA 94566

Reynolds Metals Company
Metallurgical Research Division
4th & Canal Streets
Richmond, VA 23219
Attn: Dr. Grant Spangler

The Dow Metal Products Company
Hopkins Building
Midland, Michigan 48640

Dr. F.N. Mandigo
Olin Metals Research Laboratories
91 Shelton Ave.
New Haven, CT 06515

General Electric Co.
Corporate Research & Development
Bldg. 36-441
Schenectady, NY 12345
Attn: Dr. J.H. Westbrook, Manager
        Materials Information Services

Dr. E.A. Starke, Jr.
School of Chemical Engineering and
  Metallurgy
Georgia Institute of Technology
Atlanta, GA 30332

Dr. R. Balluffi, Chairman
Dept. of Materials Science & Engineering
Bard Hall
Cornell University
Ithaca, NY 14853

Dr. D.J. Duquette
Materials Engineering Dept.
RPI
Troy, NY 12181

United Technologies Research
  Laboratories
East Hartford, CT 06108
Attn: Mr. Roy Fanti

Autonetics Division of Rockwell
  International
P.O. Box 4173
Anaheim, CA 92803
Attn: Mr. A.G. Gross, Jr.
        Dept. 522-92

DATE
FILMED

7-8